Downloaded from orbit.dtu.dk on: Aug 08, 2016

Technical University of Denmark

Structural Optimization of non-Newtonian Microfluidics

Jensen, Kristian Ejlebjærg; Okkels, Fridolin; Szabo, Peter

Publication date:
2013

Document Version
Publisher's PDF, also known as Version of record

Link to publication

Citation (APA):
Jensen, K. E., Okkels, F., & Szabo, P. (2013). Structural Optimization of non-Newtonian Microfluidics.

General rights
Copyright and moral rights for the publications made accessible in the public portal are retained by the authors and/or other copyright owners and it is a condition of accessing publications that users recognise and abide by the legal requirements associated with these rights.

- Users may download and print one copy of any publication from the public portal for the purpose of private study or research.
- You may not further distribute the material or use it for any profit-making activity or commercial gain
- You may freely distribute the URL identifying the publication in the public portal ?

If you believe that this document breaches copyright please contact us providing details, and we will remove access to the work immediately and investigate your claim.

Ph.D. Thesis

Structural Optimization of non-Newtonian Microfluidics

Kristian Ejlebjerg Jensen

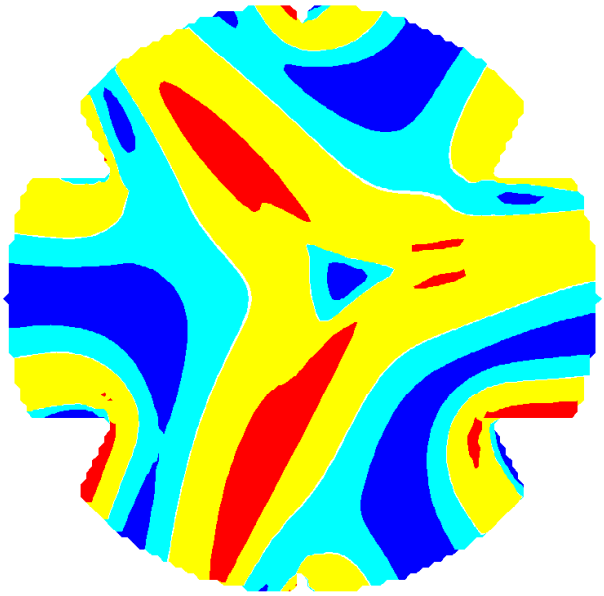

Supervisors: Associate Professor Fridolin Okkels
Associate Professor Peter Szabo

Department of Micro- and Nanotechnology
Technical University of Denmark

August 16, 2013

DTU Nanotech
Department of Micro- and Nanotechnology

Technical University of Denmark

Preface

This thesis is submitted in partial fullfillment of the requirements for obtaining the Ph.D. degree. The project was carried out over 3 years starting the 1st of August 2010 at the Department of Micro- and Nanotechnology, Technical University of Denmark. Supervisors on the project were Associate Professor Fridolin Okkels and Associate Professor Peter Szabo from Nanotech and the Department of Chemical and Biochemical Engineering, respectively.

I am grateful to Peter for introducing me to the world of non-Newtonian fluids and to Fridolin for his guidance on topology optimization. They both took their time to answer all of my questions to the best of their abilities. The Theoretical Microsystems Optimization group has provided a cosy working environment. I have shared an office with Andrea Cavalli throughout the project, and I have enjoyed his Italian perspective on Denmark as well as his input on science and life in general. I thank Assistant Professor Manuel Alves for hosting my external stay during 6 months in his group at the Department of Chemical Engineering, FEUP, University of Porto. The postdocs Francisco J. Galindo Rosales and Laura Campo Deaño helped with many of the practicalities, and as such they were crucial for this experimental Portuguese investigation.

The project was financed by DTU Nanotech, but travel expenses related to conferences and the external stay were supported by the Otto Mønsted foundation, Fabrikant P.A. Fisker Foundation and Reinholdt W. Jorck and Wife's foundation.

Kgs. Lyngby, August 16, 2013.

Kristian Ejlebjærg Jensen

Resumé (in Danish)

Strukturel Optimering af ikke-Newtonske væsker i Mikrofluide Systemer

Mange biologiske væsker kan analyseres i mikrofluide laboratorier, og disse væsker kan have en elastisk mikrostruktur, der giver væskerne elastiske egenskaber. Sådanne væsker kaldes ikke-Newtonske eller, mere præcist, viskoelastiske. De kan give anledning til eksotiske fænomer på makroskala, som aldrig ses for væsker bestående af små molekuler, såsom vand. Betydningen af disse viskoelastiske egenskaber i forhold til inerti øges, når systemet skaleres ned. Derfor bliver der forsket i at erstatte inertielle effekter med ikke-Newtonske egenskaber i mikrofluide laboratorier, men designprocessen for systemer med ikke-Newtonske væsker kompliceres af, at det er vanskeligt at anvende intuition.

Denne afhandlingen kombinerer topologioptimeringsmetoden med differential konstitutive ligninger til beskrivelse af viskoelastiske væsker. Optimeringsmetoden kan forbedre et design iterativt baseret på en matematisk analyse, og denne teknik kan derfor bruges til at identificere et fremragende design uden brug af intuition. Vi har anvendt kombinationen til at optimere en ventil uden bevægelige dele og fundet et nyt design [P2]. Vi har karakteriseret dette design eksperimentelt og sammenlignet resultaterne med det etablerede hyperbolske design. Vi fandt bedre virkningsgrad i optimeringsregimet for det nye design og sammenlignelig optimal virkningsgrad [P3].

En geometri med et kryds er kendt for at give anledning til bistabile strømningsmønstre for viskoelastiske væsker. Vi har studeret denne geometri, og vi har anvendt optimeringen på ideer relateret til bistabiliteten ved brug af en heuristisk metode. Det er en succes for de simple ideer, men den mest udfordrende ide virker til at kræve en mere stringent metodik.

Endelig indeholder afhandlingen numeriske kode, som er specifik til COMSOL Multiphysics, et kommercielt simuleringsprogram. Koden kan beregne den viskoelastiske strømning i en standardiseret geometri, og vi håber den kan hjælpe nybegyndere såvel som erfarne forskere i feltet af differential konstitutive ligninger.

Abstract

Structural Optimization of non-Newtonian Microfluidics

Many of the biological fluids analyzed in Lab-on-a-Chip systems contain elastic components, which gives the fluids elastic character. Such fluids are said to be non-Newtonian or, more precisely, viscoelastic. They can give rise to exotic effects on the macroscale, which are never seen for fluids consisting of small molecules, such as water. These viscoelastic effects become increasingly important as devices are scaled down, in particular relative to inertial effects. Experimental researchers have thus investigated the possibility of replacing Lab-on-a-Chip components relying on inertial effects with components relying on viscoelastic effects, but the non-intuitive nature of these fluids complicates the design process.

This thesis combines the method of topology optimization with differential constitutive equations, which govern the flow of viscoelastic fluids. The optimization method iteratively improves a material layout based on a mathematical analysis, and this technique therefore has the potential to identify excellent designs without user intervention. We have applied the combination to the problem of a valve without moving parts, and found a novel design [P2]. We characterized this design experimentally, and compared the results with the established hyperbolic designs. We found superior performance in the parameter regime of the optimization as well as similar optimal performance [P3].

The cross-slot geometry is known to exhibit bistability for viscoelastic fluids. We studied this geometry, and applied the optimization to ideas related to the bistability using a heuristic approach [P4]. This is successful for the most simple ideas, but the most advanced idea seems to call for a stricter methodology.

Finally the thesis contains numerical code specific to COMSOL Multiphysics [P1], a commercial finite element package. The code is capable of calculating the viscoelastic flow in a benchmark geometry, and we hope that it will help newcomers as well as experienced researchers in the field of differential constitutive equations.

Publications

The following publications are part of the thesis

P1 K.E. Jensen, P. Szabo and F. Okkels, Implementation of the Log-Conformation Formulation for Two-Dimensional Viscoelastic Flow, *submitted to International Journal for Numerical Methods in Fluids*, starting on page 19.

P2 K.E. Jensen, P. Szabo and F. Okkels, Topology optimization of viscoelastic rectifiers, *Applied Physics Letters* **100**, 243102 (2012), starting on page 39.

P3 K.E. Jensen ,P. Szabo, F. Okkels and M.A. Alves, Experimental characterisation of a novel viscoelastic rectifier design, *Biomicrofluidics* **6**, 044112 (2012), starting on page 47.

P4 K.E. Jensen, P. Szabo and F. Okkels, Optimization of Bistable Viscoelastic Systems, *submitted to Structural and Multidisciplinary Optimization*, starting on page 56.

The project also involved oral contributions to three international conferences (WCSMO9, IWNMNNF17, WCSMO10) as well as three smaller national meetings (Krogerup 2011, DANSIS 2012 and NRC2013).

Contents

List of Symbols

Symbol [unit]	Description	Definition
E, ν [Pa]	Young's modulus and Poisson ratio	
ρ	Density	
$\underline{\underline{\mathbf{I}}}$	Identity matrix	
ϵ	Small numerical parameter	
$\mathbf{v}$ [m/s], t [s]	Velocity and time	
$\dot{V}$ [m^3/s]	Flow rate	
$\underline{\underline{\mathbf{G}}}$	Continuous velocity gradient	chapter 2
$\underline{\underline{\mathbf{s}}}$	Logarithm of conformation tensor	chapter 2
$\underline{\underline{\boldsymbol{\tau}}}$, $\underline{\underline{\boldsymbol{\tau}}}_e$, $\underline{\underline{\boldsymbol{\tau}}}_s$ [Pa]	Stress, elastic stress and solvent stress tensor	sec. 1.2.5
p [Pa]	Pressure	sec. 1.2.2
η, η_s, [Pa s]	Viscosity, solvent viscosity	sec. 1.2.2 and 1.2.5
η_p [Pa s]	Polymer viscosity	page 7
λ [s]	Relaxation time	page 7
We	Weissenberg number	page 10
β	Solvent to total viscosity ratio	page 10
θ	Design variable	sec. 3.1
$\tilde{\theta}$, $\bar{\theta}$	Filtered and projected design variable	sec. 3.1.1 and page 42
ϕ	Objective function	sec. 3.1
$L_{\min}$ [m]	Filter length	sec. 3.1.1
ξ	Projection parameter	page 42
q	Interpolation convexity	page 42
α [Pa s/m^2]	Brinkman damping term a	sec. 1.2.2
$\alpha_{\max}$ [Pa s/m^2]	maximum damping for optimization.	page 42
$\underline{\underline{\mathbf{A}}}$	Conformation tensor	page 8
$\mathbf{a}$, a_{eq}, [m]	End-to-End vector and equilibrium length	page 7
$\mathrm{a}_{\max}$	Maximum dumbbell extension in units of a_{eq}	
Re	Reynolds number	page 10
We	Weissenberg number	page 10
Da	Darcy number	page 10
El	Elasticity number	page 11
P	SIMP penalization exponent	page 36
k	Spring constant modification	page 8
$\dot{\boldsymbol{\gamma}}$ [s^{-1}]	Rate of deformation tensor	page 3
$\boldsymbol{\gamma}$	Deformation tensor	page 36

Chapter 1

Background

1.1 Introduction

1.1.1 Motivation

The Lab-on-a-Chip research field concerns the down-scaling of laboratories to micro fluidic chips. This has the potential to reduce cost, analysis time and sample volume. Some of the applied techniques exploit the non-linear nature of inertial effects, but the effect of inertia is negligible on small scales. There is thus a need for an alternative source of non-linearity. Non-Newtonian effects have been proposed as a substitute, since they do not vanish at the micro scale, and experimental researchers have not only demonstrated the superiority of Non-Newtonian over inertial effects for valves without moving parts, but also showed that entirely new devices, such as the bistable cross-slot, can be realized.

Non-Newtonian fluids appear abundantly in industry in the form of coating application and plastic processing as well as in the form of biological fluids in food and human bodies. The elastic micro-structure of these fluids can give rise to exotic flow phenomena on the macro scale. Many engineers have been able to adopt an intuitive understanding of inertial effects in fluids, but the same kind of understanding is more elusive in the context of non-Newtonian effects. In fact, non-Newtonian fluids often tend to be counter-intuitive, in the sense that they give a response opposite of inertial fluids, which complicates the process for designing devices relying on non-Newtonian effects.

1.1.2 Thesis Structure

This thesis presents an approach to the design process in terms of a break away from relying on intuition. Instead, differential constitutive equations describing the viscoelastic fluid flow are combined with the method of topology optimization, which has previously been used for reducing the use of intuition in many other areas of engineering. The thesis starts out with an introduction to Non-Newtonian fluids and Rheology. Then the numerical modeling with the finite element method is discussed followed by a paper [P1], which serves as an introduction to all the tricks related to numerical solution of differential constitutive equations. The paper includes results in a novel geometry, but its primary purpose is to ease entry in the field for new researchers by means of an attached high-level implementation, that produces results for a popular benchmark problem. This is followed by a section on the method of topology optimization, and a paper [P2] on the optimization of passive valves relying on anisotropic flow resistance. The optimization results in novel design, which is verified experimentally in paper [P3]. Finally, the thesis concludes with a paper [P4] on optimization of the bistable flow in the cross-slot geometry.

1.2 Modeling of non-Newtonian Fluids

This section deals with a subgroup of Non-Newtonian fluids called viscoelastic fluids, which are the focus of this thesis. These fluids have properties resembling those of Newtonian fluids as well as elastic solids, due to the fact that they contain elastic components, i.e. polymers or biological molecules. Before going into a detailed derivation related to this subject, we will visit the topics of continuum modeling and Newtonian fluids.

1.2.1 Continuum Modeling

Continuum models are entirely macroscopic in nature, and they are the basis of this thesis. The alternative is micro-macro methods such as Brownian configuration fields [1], or fully atomistic methods such as Monte Carlo or non-equilibrium molecular dynamics (NEMD) simulations [2].

Continuum models assume that the characteristic length in the geometry of interest is much smaller than any discrete components in the fluid, i.e. the bond in a water molecule and the backbone in a polymer are much shorter than the channel width. In example, it is not possible to model the flow of red blood cells in a channel, if the dimensions of the channel are comparable to the size of the cells.

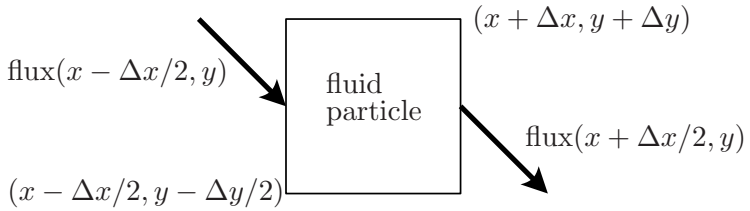

Figure 1.1: A flux flows through a fluid particle of size $(\Delta x, \Delta y)$ centered at (x, y).

It is in this context, that the concept of *fluid particles* arises. These are small volumes in which conservation laws can be considered, such that scaling to the infinitesimal size allows for derivation of the governing partial differential equation. As an example, the flux through such a particle is illustrated in figure 1.1 for the two-dimensional case. If one takes the flux to be the flow of mass $\rho\mathbf{v}$ one arrives at the continuity equation

$$
\begin{aligned}
\left.\frac{\partial \rho}{\partial t}\right|_{(x,y)} \Delta x \Delta y &= \overbrace{\rho(x - \Delta x/2, y)\mathbf{v}(x - \Delta x/2, y)\Delta y}^{\text{left}} - \overbrace{\rho(x + \Delta x/2, y)\mathbf{v}(x + \Delta/2x, y)\Delta x}^{\text{right}} \\
&+ \overbrace{\rho(x, y - \Delta y/2)\mathbf{v}(x, y - \Delta y/2)\Delta x}^{\text{lower}} - \overbrace{\rho(x, y + \Delta y/2)\mathbf{v}(x, y + \Delta y/2)\Delta x}^{\text{upper}} \\
\Leftrightarrow \left.\frac{\partial \rho}{\partial t}\right|_{(x,y)} &= \frac{\rho(x - \Delta x/2, y)\mathbf{v}(x - \Delta x/2, y) - \rho(x + \Delta x/2, y)\mathbf{v}(x + \Delta x/2, y)}{\Delta x} \\
&+ \frac{\rho(x, y - \Delta y/2)\mathbf{v}(x, y - \Delta y/2) - \rho(x, y + \Delta y/2)\mathbf{v}(x, y + \Delta y/2)}{\Delta y} \\
\Delta x, \Delta y \overset{\Rightarrow}{\to} 0 \; \frac{\partial \rho}{\partial t} &= \partial_x \left(\rho\mathbf{v} \cdot \hat{\mathbf{x}}\right) + \partial_y \left(\rho\mathbf{v} \cdot \hat{\mathbf{y}}\right) = \boldsymbol{\nabla} \cdot (\rho\mathbf{v}),
\end{aligned}
$$

where ∂_x and ∂_y denote differentiation with respect to the spatial coordinates x and y. It is straight forward to extend the technique to three dimensions, and it can be used to derive many partial differential equations, but since the expressions can become quite lengthy, we will not repeat this exercise for the following partial differential equations.

1.2.2 Newtonian Fluids

Consider a fluid with a velocity field $\mathbf{v}$, which depends on the position $\mathbf{x}$. The symmetrized derivative of the velocity field with respect to position, $\dot{\underline{\underline{\gamma}}} = \boldsymbol{\nabla}\mathbf{v} + (\boldsymbol{\nabla}\mathbf{v})^T$ is called the rate of strain tensor, and it quantifies the internal deformation of the fluid.

Stress, $\underline{\underline{\boldsymbol{\tau}}}$ is used to describe the forces between fluid particles relative to the surfaces of these particles. One can argue that the total torque on the particle should be equal to zero, and this leads to the conclusion that the stress tensor has to be symmetric. In this case the force on a particle is equal to

$$\mathbf{F}_{\text{particle}} = \int_{\partial\Omega} \underline{\underline{\boldsymbol{\tau}}} \cdot \hat{\mathbf{n}} dA,$$

where $\hat{\mathbf{n}}$ is the outward pointing normal vector on the surface of the particle. This convention defines tension to be positive and compression to be negative. The picture of a fluid particle can also be used to derive that the force per volume is equal to $\boldsymbol{\nabla} \cdot \underline{\underline{\boldsymbol{\tau}}}$.

A proportional relation between strain and viscous stress is what defines a Newtonian fluid with the viscosity, η, equal to the constant of proportionality,

$$\underline{\underline{\boldsymbol{\tau}}}_\eta = \eta \dot{\underline{\underline{\gamma}}} = \eta \left[\boldsymbol{\nabla}\mathbf{v} + (\boldsymbol{\nabla}\mathbf{v})^T \right].$$

Here we have neglected the term due to compression, as we will consider incompressible fluids. This means that requiring conservation of mass leads to the continuity equation,

$$0 \quad = \quad \boldsymbol{\nabla} \cdot \mathbf{v}. \tag{1.1}$$

If inertia is neglected, acceleration of fluid particles vanishes, such that the forces due to viscosity and pressure, $-\boldsymbol{\nabla} p$, have to balance in what is called Stokes flow,

$$\mathbf{0} \quad = \quad \boldsymbol{\nabla} \cdot \underline{\underline{\boldsymbol{\tau}}} = \boldsymbol{\nabla} \cdot \left(-\underline{\underline{\mathbf{I}}} p + \eta \left[\boldsymbol{\nabla}\mathbf{v} + (\boldsymbol{\nabla}\mathbf{v})^T \right] \right),$$

where the total fluid stress, $\underline{\underline{\boldsymbol{\tau}}}$ has been introduced. This brings the number of equations in agreement with the number of variables (p, $\mathbf{v}$).

The equation for Stokes flow (1.2) can be supplemented with other forces on its right-hand side. Examples include the effect of inertia and damping due to permeable materials given by

$$\mathbf{F}_{\text{inertia}} = -\rho \left[(\mathbf{v} \cdot \boldsymbol{\nabla})\mathbf{v} - \partial_t \mathbf{v} \right] \quad \text{and} \quad \mathbf{F}_{\text{permeable}} = -\alpha \mathbf{v},$$

where α is the inverse permeability and ∂_t denotes differentiation with respect to time. Considering an incompressible fluid with inertia thus leads to the Navier-Stokes equation,

$$\mathbf{0} = -\boldsymbol{\nabla} p + \eta \nabla^2 \mathbf{v} - \rho \frac{D\mathbf{v}}{Dt} \tag{1.2a}$$

$$0 = \boldsymbol{\nabla} \cdot \mathbf{v}, \tag{1.2b}$$

where the time convected derivative, $D = (\mathbf{v} \cdot \boldsymbol{\nabla}) + \partial_t$ has been introduced and

$$\boldsymbol{\nabla} \cdot (\boldsymbol{\nabla}\mathbf{v})^T \quad = \quad 0 \tag{1.3}$$

has been used to cancel out the out transposed velocity gradient. This latter operation is only valid for incompressible fluids with constant density, where the continuity equation reduces to a requirement of a divergence free velocity field, $\boldsymbol{\nabla} \cdot \mathbf{v} = 0$. One can use this to derive equation (1.3).

Historically, a lot of work has been devoted towards solving the Navier-Stokes equation in the absence of the viscous term, the Euler equation. This is despite the fact that the viscosity always matters on some length scale, however small it might be. This meant that experimental and theoretical researchers became divided with "experiments that could not be calculated and equations that could not be measured". It was the theoretical results that were flawed in the sense that an accurate description of viscosity was lacking. Part of the problem might have been, that a close collaboration between experimental and theoretical researches was required, since it is not possible to rigorously derive the viscous term without assumptions.

The Navier-Stokes equation is similar to the convection-diffusion equation, which governs the diluted concentration, c, of some species

$$0 = \frac{Dc}{dt} - D\nabla^2 c - R, \tag{1.4}$$

where R is a reaction rate and D is the diffusion coefficient. Equations (1.2) and (1.4) are identical for $c = \mathbf{v}$, $D = \eta/\rho$ and $R = -\boldsymbol{\nabla} p$. The important thing to note is that there is a term with a Laplacian in both equations, and that the magnitude of this term relative to the other two terms depends on the material parameters. In general one says that differential equations where the Laplacian dominates are *elliptic*, and in the following we will use the Finite Element Method to solve such equations, since it is well suited for such problems. We will, however, also use it on problems which are not elliptic by adding a small amount of artificial elliptic character to the equation called *streamline diffusion*, see section 1.4.1. It is fair to say, that excellent numerical methods exists for problems with no convection and convection only, since it is a matter of Eulerian versus Lagrangian descriptions. However, the difficult (and most interesting) problems are often of weak elliptic character. Boundary layers in inertial flows, is an example of small length scales in the solution variables for a problem with weak elliptic character, and an intelligent choice of degrees of freedom is imperative for numerical solution of such problems. At least this is true before the transition to small time scales – whether due to inertial or viscoelastic effects. For inertial fluids this transition is governed by the *Reynolds number*, Re, which appears in dimensional analysis of the Navier-Stokes equation, see section 1.2.6.

1.2.3 An Example: Flow Between Infinite Parallel Plates

An illustrative solution of the Navier-Stokes equation is related to the pressure driven flow between two parallel plates, which are infinite in the z direction and situated at $y = 0$ and $y = H$, as illustrated in figure 1.2. We assume that the plates extend a distance L in the x direction, and that there is a pressure going from Δp at $x = 0$ to 0 at $x = L$.

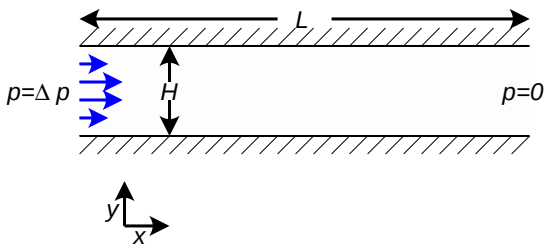

Figure 1.2: The geometry of flow between infinite parallel plates is illustrated with dimensions and coordinates.

The symmetry of the problem causes the velocity field to take the form $\mathbf{v} = v_x(y)\hat{\mathbf{x}}$, such that the inertial term drops out. The equation thus reduces to a differential equation in y, and

it is easy to see that the solution becomes

$$\mathbf{v} = \frac{\Delta p H^2}{2L\eta}(y/H)\left[1-(y/H)\right]\hat{\mathbf{x}}. \tag{1.5}$$

It is straightforward to calculate the flow rate

$$\dot{V} = \int_0^H \mathbf{v}dy = \Delta p \overbrace{\frac{H^3}{12L\eta}}^{R_{\text{hyd}}}.$$

One can choose to multiply with the width in the z direction to get the correct unit, but the important point is the strong scaling with the smaller dimension H. That is the resistance is dominated by the smaller transverse direction. Furthermore the flow rate is proportional to the driving pressure just as the current is proportional to the potential over an electrical resistor, and therefore the constant of proportionality is referred to as the hydraulic resistance. This exercise can be performed for the flow through a pipe with an arbitrary cross section, and it is thus possible to calculate the hydraulic resistance of any pipe.

The fact that connecting pipes is equivalent to connecting resistors has led to the concept of equivalent circuit theory, where numerical as well as analytical tools used in electrical engineering are applied to calculate flow rates and pressure drops without considering velocity and pressure distributions [3].

1.2.4 Generalized Newtonian Fluids

The flow properties of an incompressible Newtonian fluid can be characterized solely in terms of the density and viscosity. The viscosity can be determined by measuring the shear stress due to an imposed shear flow as illustrated in figure 1.3(a), and in the case of a non-Newtonian fluid the measured viscosity will often depend on the imposed shear rate. Therefore a lot of models with shear dependent viscosity exists, also called generalized Newtonian models. These models are excellent for describing the flow of non-Newtonian fluids in shear dominated flows such as pipes [see figure 1.3(b)], but they do not take the fluid's memory of past deformations into account. This means that they do not give rise to large normal stresses, which are necessary to describe most viscoelastic phenomena. Normal stresses can be defined and measured in shear as well as shear-free flows, but it is not strictly relevant to our thesis, and therefore we will refer the reader to [4] for a detailed description of such experiments.

Generalized Newtonian models are often characterized by the dependence of the shear-stress on the shear-rate, as shown in figure 1.4 with shear thickening fluids characterized by viscosities increasing with the shear rate and opposite for shear thinning fluids. Yield stress fluids are special in the sense that they feature a minimum shear stress, which is a desired property for creams, gels and pastes.

In this project we study anisotropic flow resistance and bistability, and due to fact that the memory of the fluid plays a crucial role for the phenomena, we use (differential) constitutive equations rather than generalized Newtonian models.

1.2.5 Differential Constitutive Equations

This section is dedicated to models for the flow of dilute viscoelastic fluids, that is fluids in which the elastic components do not directly interact. We focus on the differential formulation of these equations, as this is well suited for solving flow problems with in- and outlets in an Eulerian description, but integral versions of such equations also exist. These are well suited for a Lagrangian description and transient problems with free interfaces.

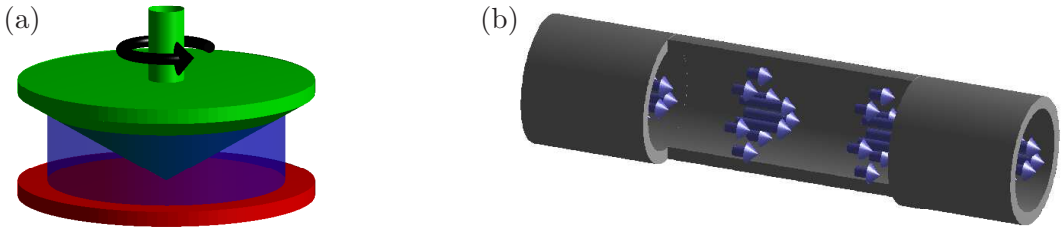

Figure 1.3: One can impose a shear flow and measure the resulting shear stress (torque) in a cone and plate rheometer (a). The result is useful for predicting the flow in a pipe of invariant cross section (b). Note that pipe flow gives rise to a velocity field, which only has a component along the flow direction, and this component only depends on the transverse coordinates. By symmetry the diagonal component of the rate of deformation tensor thus drops out, but the remaining off-diagonal component varies from zero at the center to its maximum value at the wall. In other words a range of shear rates are involved and therefore the flow is said to be non-ideal. This is opposed to the cone and plate rheometer, which uses very blunt cone angles to produce ideal flows (constant shear rate).

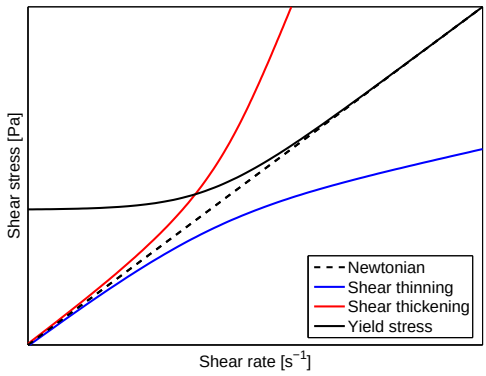

Figure 1.4: The dependence of shear stress on shear rate is illustrate for a Newtonian, a shear thinning, a shear thickening and a yield stress fluid.

Differential constitutive equations have shown excellent quantitative as well as qualitative agreement with experiments [5, 6, 7], although the prediction of pressure drop in abrupt contraction flows remains an issue as described in section 1.4.2.

The first step for formulation of any of these models is to split the total stress, $\underline{\underline{\boldsymbol{\tau}}}$, into a contribution from the solvent, $\underline{\underline{\boldsymbol{\tau}}}_s$, and one due to the elasticity, $\underline{\underline{\boldsymbol{\tau}}}_e$.

$$\underline{\underline{\boldsymbol{\tau}}} = \overbrace{-\underline{\underline{\mathbf{I}}}p + \eta_s \underline{\underline{\dot{\gamma}}}}^{\underline{\underline{\boldsymbol{\tau}}}_s} + \underline{\underline{\boldsymbol{\tau}}}_e \tag{1.6}$$

The splitting of stress is common within modelling of viscoelastic fluids, and this work uses the convention in equation (1.6), where the signs of $\underline{\underline{\boldsymbol{\tau}}}_e$ and p are opposite, but the opposite sign convention can also be used. The solvent contribution is Newtonian, and the following subsection is devoted to deriving closed form partial differential equations for the elastic stress. Note that it is not possible to derive these equations without assumptions, and that the success of these models thus relies on agreement with experiments.

Maxwell, Oldroyd-B, FENE-P and FENE-CR Models

The first attempt at a differential constitutive model for a viscoelastic fluid is due to Maxwell. He combined the properties of a Newtonian fluid with those of elastic solids in a simple way.

The shearing of a Newtonian fluid with the shear rate $\dot{\gamma}$ will give rise to a constant stress $\eta\dot{\gamma}$, while the shearing of solid will give rise to a stress growing proportionally with time, $-G\int_0^t \dot{\gamma}dt$ (for small deformations, where G is the elastic modulus). The Maxwell model thus states that the viscoelastic stress should be

$$\tau_e + \overbrace{\frac{\eta}{G}}^{\lambda}\frac{\partial \tau_e}{\partial t} = \eta\dot{\gamma}$$

For steady state motion the equation gives rise to constant stress (like a Newtonian fluid), but for a sudden stress displacement the time derivative will dominate and we get the description of an elastic material. When the shearing stops, the stress decays exponentially with a characteristic time, λ, *the relaxation time of the fluid*.

It is tempting to generalize the Maxwell model to arbitrary deformations by taking its tensor equivalent, but this turns out to be inconsistent with respect to rotation of the coordination system. The solution is to adopt a special time derivative denoted by a raised capital delta, the upper convected derivative.

$$\underline{\underline{\boldsymbol{\tau}}}_e + \lambda\overbrace{\frac{D\underline{\underline{\boldsymbol{\tau}}}_e}{Dt} - \lambda\left[\underline{\underline{\boldsymbol{\tau}}}_e\cdot(\boldsymbol{\nabla}\,\mathbf{v}) + (\boldsymbol{\nabla}\,\mathbf{v})^T\cdot\underline{\underline{\boldsymbol{\tau}}}_e\right]}^{\overset{\triangle}{\underline{\underline{\boldsymbol{\tau}}}}_e} = \eta_p\dot{\underline{\underline{\boldsymbol{\gamma}}}} \tag{1.7}$$

When excluding a solvent contribution ($\eta_s = 0$), we get the Upper Convected Maxwell Model (UCM), while we get the Oldroyd-B model otherwise. When writing out the individual components, it is important to treat $\boldsymbol{\nabla}\,\mathbf{v}$ as a 2nd rank tensor with the same components of the velocity vector in each column, i.e. $\underline{\underline{\boldsymbol{\tau}}}\cdot(\boldsymbol{\nabla}\,\mathbf{v}) + (\boldsymbol{\nabla}\,\mathbf{v})^T\cdot\underline{\underline{\boldsymbol{\tau}}} = \tau_{ij}\partial_j v_k + \partial j v_i\tau_{jk}$.

James Gardner Oldroyd gave name to the Oldroyd-A and Oldroyd-B models. He solved the problem of invariance with respect to rotation of the coordinate system by inventing the upper and lower convected derivatives. The Oldroyd-A model is based on the latter, and it is largely unused today, because agreement with experiment tends to be superior for the Oldroyd-B model. In contrast to the generalized Newtonian models, both the Oldroyd-B and UCM model have a constant shear viscosity and give rise to large normal stresses.

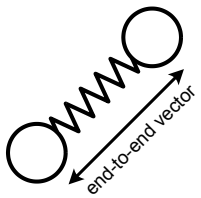

Figure 1.5: Two point masses connected with a spring, also called a dumbbell, can be used to describe orientation and elongation of the elastic particles in a viscoelastic fluid.

This derivation of the Maxwell and Oldroyd-B models takes a phenomenological approach with the upper convected derivative introduced as a fix, but it is also possible to start by considering the micro-structure of a viscoelastic fluid and arrive at the same result. The idea is that two point masses connected with a spring can describe the elastic components in what is called a *dumbbell model*, see figure 1.5. The conformation tensor is the statistical average

$\langle \cdots \rangle$, of the dyadic product between the end-to-end vector $\mathbf{a}$ and itself normalized with the equilibrium extension, a_{eq},

$$\underline{\underline{\mathbf{A}}} = \left\langle \frac{\mathbf{a} \otimes \mathbf{a}}{a_{eq}^2} \right\rangle. \tag{1.8}$$

This approach is however not free of assumptions either, since one has to introduce the upper convected derivative by assuming a result called the Giesekus relation. Some models are substantially easier to write and understand, when expressed in terms of the conformation tensor, in particular the FENE-P model discussed in the following. Another point is that it makes the model compatible with the log-conformation formulation discussed in the implementation paper [P1]. Finally, the derivation of the constitutive equations from this starting point relates the relaxation time and polymer viscosity to properties of the micro-structure

$$\lambda = \frac{\zeta}{4H} \qquad \text{and} \qquad \eta_p = \frac{n k_B T \zeta}{4H},$$

where ζ is a friction coefficient between the fluid and the dumbbells, H is the spring constant, n is the dumbbell concentration, T is the temperature and k_B is the Boltzmann constant.

Assuming a Hookean spring force for the dumbbell it is possible to show, the Oldroyd-B model can be written as

$$\begin{aligned} \frac{\partial \underline{\underline{\mathbf{A}}}}{\partial t} &= \overbrace{-\frac{1}{\lambda}\left(\underline{\underline{\mathbf{A}}} - \underline{\underline{\mathbf{I}}}\right)}^{\text{relaxation}} - \overbrace{(\mathbf{v}\cdot\boldsymbol{\nabla})\,\underline{\underline{\mathbf{A}}}}^{\text{convection}} + \overbrace{\left[\underline{\underline{\mathbf{A}}}\cdot(\boldsymbol{\nabla}\,\mathbf{v}) + (\boldsymbol{\nabla}\,\mathbf{v})^T \cdot \underline{\underline{\mathbf{A}}}\right]}^{\text{stretching/orientation}} \\ \underline{\underline{\boldsymbol{\tau}}}_e &= \frac{\eta_p}{\lambda}\left(\underline{\underline{\mathbf{A}}} - \underline{\underline{\mathbf{I}}}\right) \end{aligned} \tag{1.9}$$

The Hookean spring force of the Oldroyd-B and UCM models can give rise to exponential growth in time for the conformation tensor in the case of an extensional flow. This is unphysical, because the ratio of extension to equilibrium length quickly exceeds that of the elastic micro component. This behavior can also prevent convergence of numerical algorithms in free stagnations, which appear in geometries such as the cross-slot described in chapter 2. The remedy is to introduce a varying spring constant, such that the relaxation term balances the stretching term, when the dumbbells become very extended

$$\frac{\partial \underline{\underline{\mathbf{A}}}}{\partial t} = -\frac{1}{\lambda}\left(k(\underline{\underline{\mathbf{A}}})\underline{\underline{\mathbf{A}}} - \underline{\underline{\mathbf{I}}}\right) - (\mathbf{v}\cdot\boldsymbol{\nabla})\,\underline{\underline{\mathbf{A}}} + \left[\underline{\underline{\mathbf{A}}}\cdot(\boldsymbol{\nabla}\,\mathbf{v}) + (\boldsymbol{\nabla}\,\mathbf{v})^T \cdot \underline{\underline{\mathbf{A}}}\right] \tag{1.10a}$$

$$\underline{\underline{\boldsymbol{\tau}}}_e = \frac{\eta_p}{\lambda}\left(k(\underline{\underline{\mathbf{A}}})\underline{\underline{\mathbf{A}}} - \underline{\underline{\mathbf{I}}}\right) \tag{1.10b}$$

$$k(\underline{\underline{\mathbf{A}}}) = \frac{1}{1 - \mathrm{Trace}(\underline{\underline{\mathbf{A}}})/a_{max}^2} \tag{1.10c}$$

where $k(\underline{\underline{\mathbf{A}}})$ is a non-linear modification of the spring constant that causes the spring force to diverge, when the dumbbell extension approaches a_{max} times the equilibrium length. The model is called the Finite Extensible model, FENE-P [8]. Note that the Oldroyd-B model is recovered in the limit of $a_{max} \to \infty$. The model gives rise to shear thinning with a power law slope of 2/3 at high shear rates, but dilute polymer solutions usually have a near constant shear viscosity to allow separation of elastic from viscous effects. The FENE-CR model [9] addresses this as it keeps the spring constant of the FENE-P model (1.10c), but takes it outside parentheses in the

expressions for the elastic stress (1.10b) and relaxation term in the evolution equation (1.10a),

$$\frac{\partial \underline{\underline{\mathbf{A}}}}{\partial t} = -\frac{k(\underline{\underline{\mathbf{A}}})}{\lambda}\left(\underline{\underline{\mathbf{A}}} - \underline{\underline{\mathbf{I}}}\right) - (\mathbf{v}\cdot\boldsymbol{\nabla})\,\underline{\underline{\mathbf{A}}} + \left[\underline{\underline{\mathbf{A}}}\cdot(\boldsymbol{\nabla}\,\mathbf{v}) + (\boldsymbol{\nabla}\,\mathbf{v})^T\cdot\underline{\underline{\mathbf{A}}}\right] \tag{1.11a}$$

$$\underline{\underline{\boldsymbol{\tau}}}_e = \frac{\eta_p}{\lambda}k(\underline{\underline{\mathbf{A}}})\left(\underline{\underline{\mathbf{A}}} - \underline{\underline{\mathbf{I}}}\right) \tag{1.11b}$$

$$k(\underline{\underline{\mathbf{A}}}) = \frac{1}{1 - \mathrm{Trace}(\underline{\underline{\mathbf{A}}})/\mathrm{a}^2_{\max}}. \tag{1.11c}$$

Alternatively one can see the FENE-CR model as the Oldroyd-B model with a relaxation time equal to $\lambda[1 - \mathrm{Trace}(\underline{\underline{\mathbf{A}}})/L^2]$. That is, the relaxation time decreases as the maximum extension is approached. The model gives rise to a constant shear viscosity, while preserving the upper bound on the conformation tensor, and it is the primary model used throughout all articles. Besides the FENE-P and FENE-CR models there is a simplified version of the FENE-CR model (FENE-MCR), which is well suited for a stress-formulation (where the conformation tensor is not a variable, see [10]).

Boundary Conditions

Boundary conditions can be separated in the categories of Dirichlet and Neumann. Dirichlet boundary conditions are used to

- impose the noslip boundary condition ($\mathbf{v} = \mathbf{0}$) on walls.
- fix the inlet velocity for problems with a fixed flow rate.
- fix the in- and outlet pressure for pressure driven problems.
- impose zero normal flow through symmetry lines ($\mathbf{v}\cdot\hat{\mathbf{n}} = 0$).
- set a certain value for the conformation tensor on inlets.

With regards to the last point, we have found that taking the conformation tensor equal to the identity matrix at inlets gives rise to the most robust formulation – although not the most accurate.

In the context of viscoelastic flow, the Neumann boundary condition is encountered for pressure driven calculations. These require that the stress is specified on the in- and outlets, and the details of this is described in section 1.4.1.

1.2.6 Dimensionless Form

The point of writing an equation in dimensionless form is to reduce the number of relevant free parameters to a minimum by introducing dimensionless variables (denoted with tilde)

$$\mathbf{x} = L_{\mathrm{char}}\tilde{\mathbf{x}}, \quad \mathbf{v} = v_{\mathrm{char}}\tilde{\mathbf{v}}, \quad t = \frac{L_{\mathrm{char}}}{v_{\mathrm{char}}}\tilde{t}, \quad p = \frac{v_{\mathrm{char}}\eta}{L_{\mathrm{char}}}\tilde{p}, \quad \text{and} \quad \alpha = \alpha_{\mathrm{char}}\tilde{\alpha},$$

where L_{char}, v_{char} and α_{char} denotes characteristic length scale, velocity and damping respectively. They relate the dimension full form of space, time, velocity, pressure and inverse permeability to their dimensionless equivalents.

The Navier-Stokes Equations (1.2) can thus be written as

$$\mathbf{0} = \tilde{\boldsymbol{\nabla}} \cdot \left(-\underline{\underline{\mathbf{I}}}\tilde{p} + \left[\tilde{\boldsymbol{\nabla}}\tilde{\mathbf{v}} + \left(\tilde{\boldsymbol{\nabla}}\tilde{\mathbf{v}} \right)^T \right] \right) - \overbrace{\frac{\rho v_{\text{char}} L_{\text{char}}}{\eta}}^{\text{Re}} \frac{D\tilde{\mathbf{v}}}{D\tilde{t}} - \overbrace{\frac{\alpha_{\text{char}} L_{\text{char}}^2}{\eta}}^{\text{Da}^{-1}} \tilde{\alpha}\tilde{\mathbf{v}} \tag{1.12a}$$

$$0 = \tilde{\boldsymbol{\nabla}} \cdot \tilde{\mathbf{v}}, \tag{1.12b}$$

where the Reynolds, Re, and Darcy, Da, number have been identified. The regime of high inertia (relative to viscous effects) is characterized by Reynolds numbers much larger than unity, while small Darcy numbers correspond to strong damping. Note that the Reynolds number is usually expressed in terms of a characteristic velocity, such that the characteristic pressure becomes defined in terms of the characteristic velocity,

$$p_{\text{char}} = \eta \frac{v_{\text{char}}}{L_{\text{char}}},$$

but one might as well do it the way around. It is in fact necessary for pressure driven calculation, since one has no reference velocity at the inlet for such a flow. One can then compute the Reynolds number expressed from a characteristic velocity as a post processing step – in the case where this is required for comparison with other works.

The FENE-CR Model can be written in dimensionless form by introducing a dimensionless elastic stress,

$$\underline{\underline{\boldsymbol{\tau}}}_e = (\eta_s + \eta_p) \frac{v_{\text{char}}}{L_{\text{char}}} \tilde{\underline{\underline{\boldsymbol{\tau}}}}_e,$$

such that the governing equation (1.11) becomes

$$\overbrace{\frac{\lambda v_{\text{char}}}{L_{\text{char}}}}^{\text{We}} \overset{\Delta}{\underline{\underline{\mathbf{A}}}} = -k(\underline{\underline{\mathbf{A}}}) \left(\underline{\underline{\mathbf{A}}} - \underline{\underline{\mathbf{I}}} \right) \tag{1.13a}$$

$$\tilde{\underline{\underline{\boldsymbol{\tau}}}}_e = \overbrace{\frac{\eta_p L_{\text{char}}}{v_{\text{char}}(\eta_s + \eta_p)\lambda}}^{(1-\beta)/\text{We}} k(\underline{\underline{\mathbf{A}}}) \left(\underline{\underline{\mathbf{A}}} - \underline{\underline{\mathbf{I}}} \right) \tag{1.13b}$$

$$k(\underline{\underline{\mathbf{A}}}) = \frac{1}{1 + \text{Trace}(\underline{\underline{\mathbf{A}}})/L^2} \tag{1.13c}$$

, where the Weissenberg number, We, and solvent to total viscosity ratio, β, have been identified. Note that the dimensionless form corresponds to the substitutions $\text{We} \to \lambda$, $\beta \to \eta_s$ and $1-\beta \to \eta_p$. The governing equation of a Newtonian fluid is recovered in the limit of β going to unity or We going to zero, while the extensibility parameter, a_{max}, going to infinity gives the Oldroyd-B model. Large Weissenberg numbers, small viscosity ratios and high extensibility parameters thus characterize flows with a strong viscoelastic character. This regime actually has similarities with that of high Reynolds number flows, in the sense that small length and time scales appear. The similarities, however, tend to have an anti-symmetric nature, in the sense that viscoelastic fluids tend to behave opposite of inertial fluids, in example

- The Weissenberg effect is the tendency for a viscoelastic fluid to climb a rotating stirring rod. An inertial flow would cause a depression in the liquid-gas interface due to the centrifugal force. One can understand the effect as tension of polymers (or whatever the elastic component is) around the rod, similar to the rotation of a fork in a bowl of spaghetti.

- Downstream recirculation in contraction flows are easy to understand for inertial fluids, but it is also well known that upstream recirculation form for viscoelastic flows as described in section 1.4.2.
- The flow at high Reynolds number in a pipe will give rise to instabilities that increase the hydraulic resistance and make the velocity profile more blunt. Similar instabilities can occur for viscoelastic fluids, but the viscoelastic forces are opposite the centrifugal ones, i.e. the destabilizing mechanism is opposite. It is therefore possible to delay the onset of inertial instabilities (and thus decrease the hydraulic resistance) by adding a viscoelastic component [11].

The anti-symmetry is only a philosophical observation, which has its limits. Viscoelastic fluids can, for instance, give rise to bistable properties as described in chapter 5, and there exists no inertial analog for this. The relative magnitude of elastic to inertial effects can be quantified using the elasticity number,

$$\mathrm{El} = \frac{\mathrm{We}}{\mathrm{Re}} = \frac{\lambda\eta}{\rho L_{\mathrm{char}}^2}, \tag{1.14}$$

which is independent of the characteristic velocity, and scales with the square of the characteristic length scale. It is this scaling that motivates the combination of viscoelastic fluids with microfluidics. In particular the examples where a desired non-linearity can be produced with both inertial and viscoelastic effects, as the latter will tend to be much stronger at the micro scale.

1.3 Rheology

Rheology is the study of flowing matter, in particular its response to various kinds of deformations, often quantified in terms of the rate of deformation tensor $\underline{\underline{\dot{\gamma}}} = \boldsymbol{\nabla}\mathbf{v} + (\boldsymbol{\nabla}\mathbf{v})^T$ and stress tensor $\underline{\underline{\tau}}$. The choice of deformation to study is highly dependent on the application, but this often points in the direction of one of three idealized flow deformations (see figure 1.6):

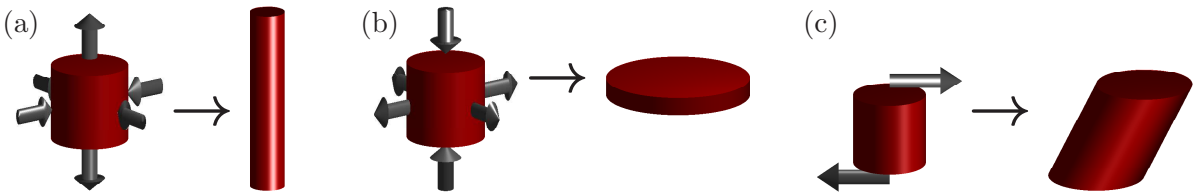

Figure 1.6: The case of uniaxial (a), bi-axial (b) and shear deformation (c) are illustrated by means of a cylinder.

Shear flow is similar to shearing a deck of cards. It is characterized by a rate of deformation tensor without diagonal components. It is typical of pipe flow and easy to realize in a cone and plate rheometer, see figure 1.3.

Uniaxial extension occurs when a fluid is deformed towards the shape of a line. Fiber spinning and extrusion are examples of flows with a high degree of uniaxial extension. It is difficult to realize an ideal uniaxial extension in experiments, because a constant extension rate involves exponential growth in time. The capillary break up extensional rheometer (see figure

1.7) has, however, gained popularity as an apparatus for determining the relaxation time using uniaxial extension.

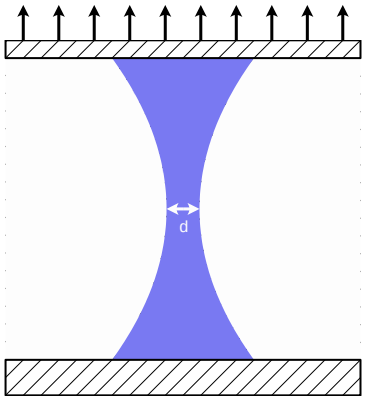

Figure 1.7: A capillary breakup extensional rheometer (CABeR) consists of two plates with a sample between them. The top plate is moved a fixed distance upwards swiftly, such that the fluid is stretched into a thin filament. An optical technique is then used to detect how surface tension causes the filament to decrease its diameter, d, as this will usually decrease exponentially in time with a half-time proportional to the relaxation time.

Bi-axial extension is the time reversed version of uniaxial extension. It occurs whenever a fluid is deformed towards the shape of a plane. Applications include all kinds of blow molding, i.e. for producing containers.

Shear flow is special in the sense, as it is characterized by separation distances growing linearly in time, while the other two "shear free flows" give rise to exponential separation in time. One can thus run out of lab space rather quickly, when trying to realize an ideal extensional flow.

The advantage of idealized flows is that the constitutive equations can be solved analytically, which makes comparison with theory much easier. However, many practical applications, such as injection molding, contains a high degree of extensional- as well as shear deformation, and it is this kind of "complex geometries" which call for numerical techniques.

1.4 Numerical Techniques

Besides the third paper [P3] the thesis relies entirely on the solution of differential constitutive equations using numerical methods, in particular the commercial high level finite element package COMSOL Multiphysics [12].

1.4.1 The Finite Element Method

A partial differential equation can be solved using the finite element method by introducing an approximate solution,

$$f(\mathbf{x}) \quad = \quad \sum_{i}^{N} c_i f_i(\mathbf{x}), \tag{1.15}$$

where c_i are coefficients to be determined and f_i are basis functions. The point is to arrive at a sparse linear equation system $\underline{\underline{\mathbf{A}}}\mathbf{c} = \mathbf{b}$, where $\underline{\underline{\mathbf{A}}}$ is a sparse matrix and $\mathbf{c}$ contains the coefficients

c_i. As an example we consider a Poisson equation in a one dimensional domain Ω with Dirichlet boundary conditions,

$$\frac{\partial^2 f}{\partial x^2} + 3(6x-4) \quad = \quad 0, \quad f(d\Omega) = 0 \quad \text{and} \quad x \in \Omega. \tag{1.16}$$

To solve this problem we introduce a *finite element mesh* consisting of nodes and elements as illustrated in figure 1.8a and 1.8b for 1D and 2D, respectively.

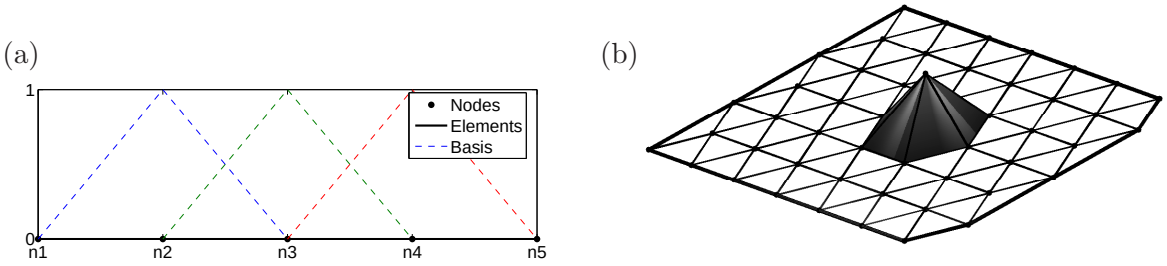

Figure 1.8: A finite element mesh consists of elements and nodes. In one dimension (a) the elements are line segments, while they are triangles in two dimensions (b) and tetrahedrons in three dimensions (It is possible to have many other types of elements, but these are the most simple). Linear basis functions are shown for the one and two dimensional case to illustrate the concept of local support, i.e. they are only non-zero in the elements containing the node at which they equal unity.

Equation (1.16) is *the strong form* of the equation, but to use the finite element method, one has to convert it to *weak form*. In order to do so one multiplies equation (1.16) with a *test function*, $\hat{f}$ and integrate over the domain,

$$0 \quad = \quad \int_\Omega \left(\frac{\partial^2 f}{\partial x^2} + 3(6x-4) \right) \hat{f} d\Omega. \tag{1.17}$$

If the test function belongs to the same function space as f, a solution to the weak form exists. A solution to the strong form (1.16) will be a solution to the weak form (1.17), but in general not the other way around.

The weak form (1.17) is closely related to the Galerkin method, which consists of using the approximation (1.15) for f. Considering a set of test functions $\hat{f}_j$, we thus get a set of weak problems,

$$\begin{aligned} 0 \quad &= \quad \int_\Omega \sum_i \left(c_i \frac{\partial^2 f_i}{\partial x^2} + 3(6x-4) \right) \hat{f}_j d\Omega \\ &= \quad \sum_i \int_\Omega \left(\hat{f}_j 3(6x-4) - c_i \frac{\partial f_i}{\partial x} \frac{\partial \hat{f}_j}{\partial x} \right) d\Omega + \sum_i \left[c_i \frac{\partial f_i}{\partial x} \hat{f}_j \right]_{x_{\text{left}}}^{x_{\text{right}}} \\ &= \quad \sum_i \int_\Omega \hat{f}_j 3(6x-4) d\Omega + \sum_i c_i \left[\frac{\partial f_i}{\partial x} \hat{f}_j \right]_{x_{\text{left}}}^{x_{\text{right}}} - \sum_i c_i \int_\Omega \frac{\partial f_i}{\partial x} \frac{\partial \hat{f}_j}{\partial x} d\Omega \end{aligned} \tag{1.18}$$

The reformulation using partial integration allows for use of basis functions consisting of nothing but first order polynomials. The test functions are taken to be zero on the domain boundaries in case of Dirichlet boundary conditions such that the square parentheses vanishes. Alternatively this parentheses can be used to impose Neumann boundary conditions. The test functions are normally taken to be the same as the basis functions, $f_i = \hat{f}_j$. Section 2.1.5 describes the details of converting the Oldroyd-B model to weak form.

The coefficients c_i are the only unknowns in equation (1.18) and by evaluating the integrals for each i and j a set of linear algebraic equations arises. The related matrix is sparse due to the local support of the basis functions, i.e. for linear basis functions integrals where $|i-j| \geq 2$ vanishes.

We discretize this example problem on the interval $x \in [0\,1]$ using five elements and arrive at the solution shown in figure 1.9. Note that the agreement at nodes is not guaranteed, since the Galerkin method enforces orthogonality of the residual with respect to the test functions in the individual elements.

This illustrates the method for linear problems, but it can be extended to non-linear problems by solving the linearized equation system and using the new solution to define the next point of linearization in a scheme similar to the Newton method.

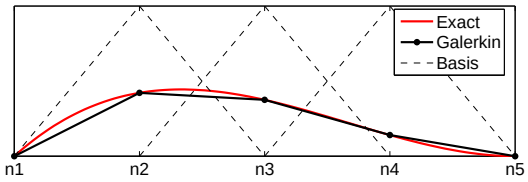

Figure 1.9: The exact and analytical solution to problem (1.16) on a finite element mesh with five elements.

A convergence test involves observing the solution as numerical parameters are varied. When working with numerical methods, one should always perform such a test, as it will reveal the extent to which the solution can be trusted. In example one might vary the number of elements and thus the number of degrees of freedom (DOF), while computing the integral of u (or some other quantity of particular interest) as shown in figure 1.10(a). One can check the variation from mesh to mesh to get a feeling for the accuracy with which the integral has been determined. In this case we have the analytical solution, and this means that we are able to compute the integrated two norm error as well as the maximum error as illustrated in figure 1.10(b). The term *polynomial accuracy* refers to the fact that the lines are straight in a log-log plot, while *order of accuracy* refers to the slope of the curves. Note that the maximum errors converges slower than the integrated two norm error, and it is typical to observe this kind of difference between *global* and *local error estimates*. It is possible to increase the slope and thus the order of accuracy of the scheme by increasing the polynomial degree of the basis functions. Varying the size of elements (h) as well as the polynomial degree (p) is called hp-FEM, while the limit of a single element with very high polynomial degree is called a spectral method. On one hand spectral methods give rise to superior accuracy for the same number of degrees of freedom, but on the other hand they are less stable and the discretized problem becomes less sparse, which result in much higher cost for determining the solution.

It is well known that geometric singularities such as sharp corners can give rise to infinite stresses, even for a Newtonian fluid, and that the Oldroyd-B and Upper Convected Maxwell models give rise to unbounded extension in free stagnation points. Such point singularities will prevent convergence in a local sense, but global convergence can still be obtained if the singularity is integrable as it is the case for the cross-slot geometry [13].

Time Dependent Problems

Transient problems can be solved with the the finite element method by treating time as yet a spatial parameter, but this is normally prohibitive in terms of computational cost (memory)

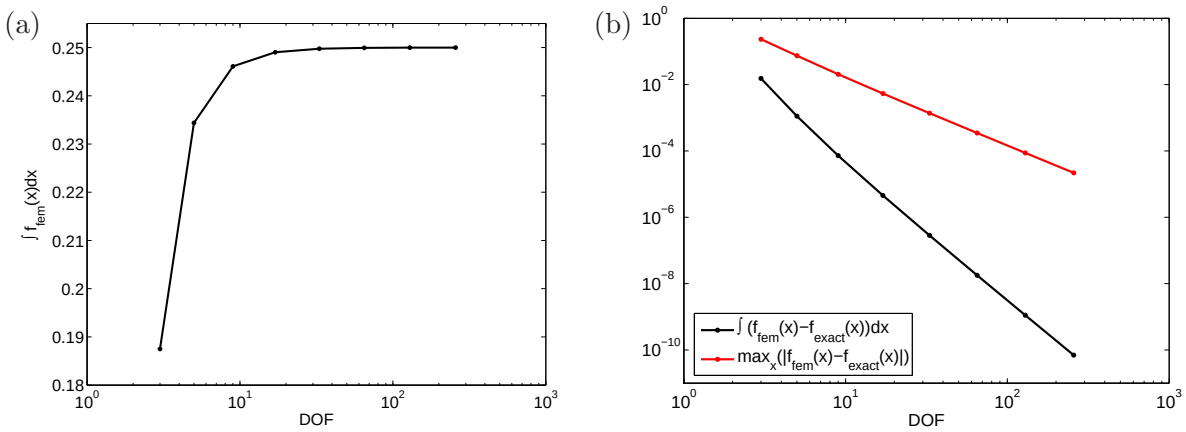

Figure 1.10: The integral of the numerical solution to the to problem (1.16) is plotted for different finite element meshes (a). The solution clearly converges, and the same can be said about the two norm and maximum error (b). The curves in (b) have slopes of -2 and close to -4.

and therefore one resorts to letting the coefficients in equation (1.15) vary with time,

$$f(\mathbf{x},t) \quad = \quad \sum_i^N c_i(t) f_i(\mathbf{x}). \tag{1.19}$$

Inserting the expression (1.19) in the governing equation and using the Galerkin method often results in an explicit expression for the time derivative of the coefficients, $\dot{c}$ in terms of the coefficients on the right-hand side.

$$\dot{\mathbf{c}} = \underline{\underline{\mathbf{A}}}\mathbf{c} - \mathbf{b} \tag{1.20}$$

This is specific to a linear system, i.e. we exploit that expressions such as the squared time derivative does not appear in the governing equation. The point is that there exists a function, which relate the coefficients to their time derivatives. Such ordinary differential equations can be solved using explicit and implicit methods. For explicit methods one calculates the coefficients at $t = \Delta t$ from the initial coefficients and their time derivatives at $t = 0$, where Δt is called the time step. The *Euler method* gives this as

$$\frac{\mathbf{c}_{n+1} - \mathbf{c}_n}{\Delta t} = \underline{\underline{\mathbf{A}}}\mathbf{c}_n - \mathbf{b} \Leftrightarrow \mathbf{c}_{n+1} = \Delta t \left(\underline{\underline{\mathbf{A}}}\mathbf{c}_n - \mathbf{b}\right) + \mathbf{c}_n$$

The Euler method is a very simple method, but it only has first order accuracy and therefore it gives a bad compromise between accuracy and computational cost. Higher order versions are however used extensively due to the low cost of evaluating the explicit expression for $\mathbf{c}_{n+1}$.

The *implicit* or *backward Euler method* differs in the sense that the time derivative is evaluated at $t = \Delta t$,

$$\frac{\mathbf{c}_{n+1} - \mathbf{c}_n}{\Delta t} = \underline{\underline{\mathbf{A}}}\mathbf{c}_{n+1} - \mathbf{b} \Leftrightarrow \mathbf{c}_{n+1} = \Delta t \left(\underline{\underline{\mathbf{A}}}\mathbf{c}_{n+1} - \mathbf{b}\right) + \mathbf{c}_n,$$

which gives rise to an implicit expression for $\mathbf{c}_{n+1}$. This makes computation more expensive, but implicit methods are preferred for many problems due to their robustness. The backward Euler method is a 1st order method, as it takes a single past solution into account, but it is possible to construct higher order variants that incorporate several past solutions. This work relies on the time dependent solver of COMSOL, which uses an implicit method with adaptive order and step size. The solver thus had the option of using higher order methods, but in practice it tends to favor 1st order, so one can say that this thesis mainly relies on the backward Euler method.

Stabilization

The finite element method is excellent at solving problems with a *strong elliptic* character such as the one in equation (1.16), that is partial differential equations where a term with second order derivatives dominates. On the other hand a pure convective problem such as

$$\mathbf{v} \cdot \boldsymbol{\nabla} c = 0 \quad \text{where} \quad \mathbf{v} \quad \text{is given}$$

are said to have *hyperbolic* character, and these cannot be solved without adding some artificial elliptic character. This is normally implemented such that convergence towards the solution to the the pure hyperbolic problem is achieved by scaling the artificial term with the mesh size. For convective problems Streamline Upwind Petrov-Galerkin (SUPG) diffusion is a popular stabilization technique which only adds diffusion along the streamlines. This gives rise to good convergence properties when compared with crosswind diffusion techniques. The most simple way to implement SUPG stabilization is to replace the test function c_{test} with $c_{\text{test}} + (h_{\text{mesh}}/v_{\text{char}})\mathbf{v} \cdot \boldsymbol{\nabla} c_{\text{test}}$ in the Galerkin weak formulation, where h_{mesh} and v_{char} are a characteristic element size and velocity, respectively. We choose to only let the h_{mesh} vary spatially, while v_{char} is taken as the average (or half for extra stability) inlet velocity.

We choose to use 1^{st} order elements for pressure and second order for velocity when discretizing the Stokes equation. Due to its popularity this element has many names: "mixed element", P_2P_1 or "Taylor Hood" to name a few. The element gives rise to a stable discretization at the cost of 2^{nd} order velocities. It is possible to use stabilization techniques that allow for 1^{st} order velocities, but we have chosen not to, because this complicates the implementation with more numerical parameters. Another reason is the fact that the solution to developed 2D channel flow is a 2^{nd} order polynomial for velocity and a 1st order for pressure, so one can in practice describe channel flow extremely well with this element. The superiority of the mixed element is thus not a question of it being a higher order method, but simply the fact that the nature of the discretization matches the physics.

1.4.2 Example: Contraction Flow

As an example of solving partial differential equations numerically using the finite element method, we compute the flow of a viscoelastic fluid in a planar[1] contraction geometry as illustrated in figure 1.11 using the implementation described in chapter 2. We take $L_c = H_c$ as characteristic length scale, a contraction ratio of $H/H_c = 2$ and inlet/outlet lengths of $L_1 = L_2 = 5$.

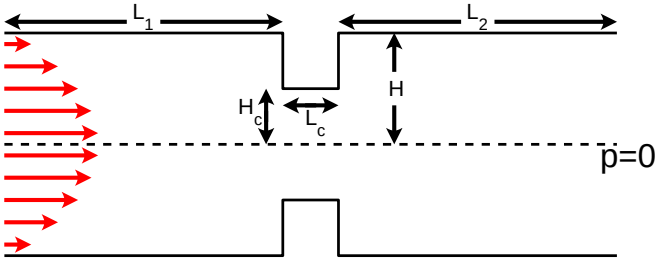

Figure 1.11: The setup for a contraction flow simulation is sketched with all the relevant length scales.

We compute the flow of a FENE-CR fluid with a solvent to total viscosity ratio of $\beta = 0.2$ and extensibility parameter $a^2_{\text{max}} = 100$. We impose a fixed inlet flow rate, $\dot{V}$, and we use this

[1] Similar results can be observed for the axisymmetric case (Personal correspondence with Manuel A. Alves from FEUP at the University of Porto).

together with H_c to calculate Weissenberg numbers. The noslip boundary condition is imposed at walls, and we use a "no normal flow" boundary condition at the symmetry line to cut the computational domain in half. The case of simple Stokes flow gives rise to a flow pattern with streamwise symmetry as shown in figure 1.12(a), while viscoelastic (b) and inertial flow (c) give rise to up- and downstream recirculations, respectively. The mixed case (d) gives rise to recirculations both up- and downstream. It is interesting to consider the effect of the mixed case on the individual recirculations, when compared to the inertial case for the downstream and viscoelastic for the upstream. If inertial and viscoelastic effects are exact opposites, one should get the Stokes flow for the mixed case, but that is clearly not the case. If the areas of the recirculations are considered, both decrease in the mixed case. If the distance between the contraction and the center point is considered, only the upstream recirculation grows, while it is the downstream recirculation that strengthens, if the actual flow rate in the recirculation is taken as the relevant characteristic.

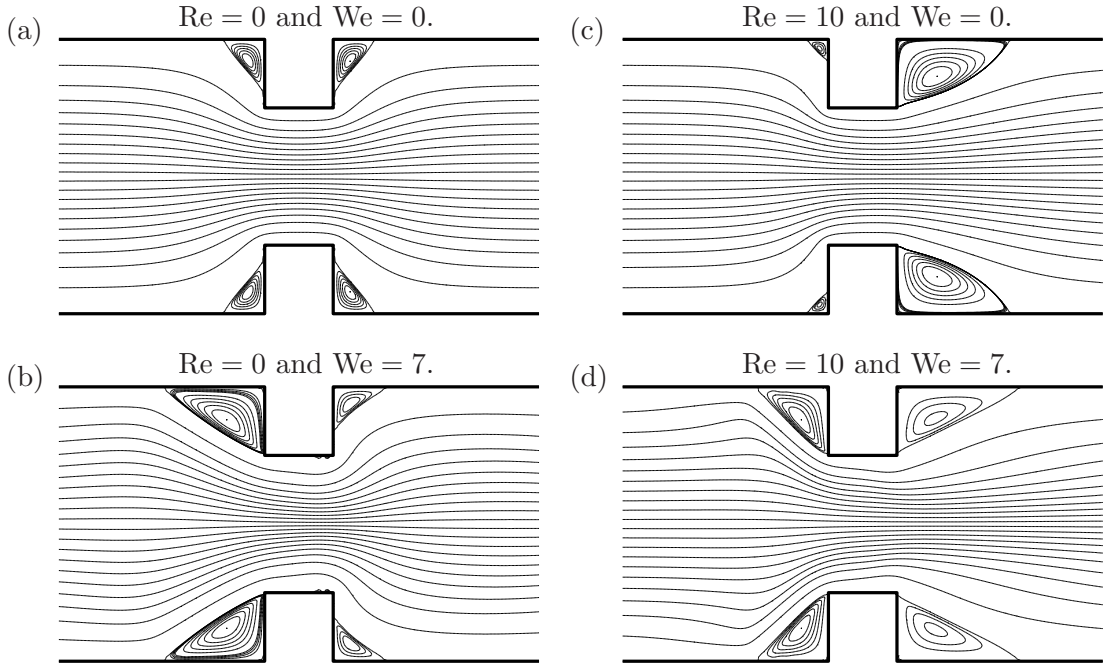

Figure 1.12: Contours are plotted for the stream function in a contraction geometry for four different flow regimes: Stokes (a), inertial (b), viscoelasic (c) and mixed (d).

The total pressure drop from inlet to outlet clearly depends on all the inlet/outlet length scales depicted in figure 1.11, but this effect can be eliminated by calculating the pressure drop corresponding to a slowly varying width, i.e.

$$\Delta p_0 \quad = \quad (\eta_s + \eta_p) \left[\frac{L_1 + L_2}{12H^2} + \frac{L_c}{12H_c^2} \right] \frac{\dot{V}}{W} \tag{1.21}$$

By subtracting Δp_0 from the total pressure drop, one can thus get an idea of the "extra pressure drop" due to the abrupt variations in width, and therefore it is this quantity that is plotted versus the Weissenberg number in figure 1.13. The figure shows different discretizations, but it only for Weissenberg numbers below 3 that the two finer ones overlap, which indicates the limit of convergence. The limit of convergence is thus close to the minimum pressure drop, which is not only below that of Stokes flow but also Δp_0. This qualitative feature of decreasing pressure drop is specific to abrupt contractions [14], and it cannot be "reproduced" in experiments [15].

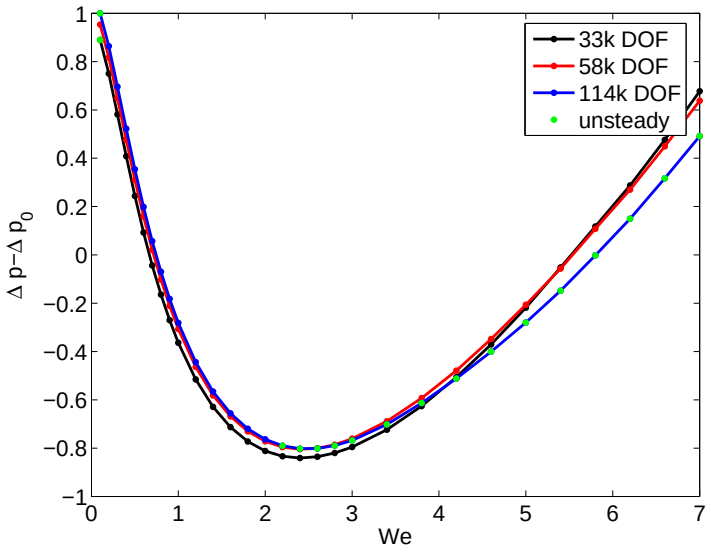

Figure 1.13: The total difference between the pressure drop and Δp_0 given by equation (1.21) is plotted as a function of the Weissenberg number for three different number of degrees of freedom (DOF).

Stream Function

Streamlines for a steady state flow can be computed by integrating the velocity field for a set of starting points, or they can be computed by solving a partial differential equation for the stream function, Ψ. In this case the latter approach was chosen as it is more convenient for plotting recirculations. The stream function can be used to compute streamlines for all steady, incompressible and two-dimensional flows. It can be related to the velocity field by

$$\mathbf{v} \cdot \hat{\mathbf{x}} = \frac{\partial \Psi}{\partial x} \quad \text{and} \quad \mathbf{v} \cdot \hat{\mathbf{y}} = -\frac{\partial \Psi}{\partial y},$$

which implies $\boldsymbol{\nabla} \cdot \mathbf{v} = 0$ in agreement with the condition of incompressibility. The stream function is governed by

$$0 \quad = \quad \nabla^2 \Psi + (\boldsymbol{\nabla} \times \mathbf{v}) \cdot \hat{\mathbf{z}}.$$

The difference between the value of the stream function in two points corresponds to the flow rate between the points, or, in other words, contours of the stream function at equispaced levels will have equal flow rates between them. One should take care in choosing boundary conditions for no-slip walls to reflect this. In example, Dirichlet boundary conditions of $\Psi = 0$ and $\Psi = 2$ were applied at the symmetry and upper wall boundary for the contraction flow in figure 1.12. The advantage of this approach is that the center of the recirculations constitute local maxima of the stream function, and this information makes it easy to specify the contours that illustrate the recirculation. In example, the stream function contours in figure 1.12 have been chosen to illustrate the recirculations, and therefore the flow rate between the streamlines in the recirculations is significantly smaller than the flow rate between the rest of the streamlines.

Chapter 2

Implementation

Popular models for viscoelastic flow are described in section 1.2, and the finite element method is described in section 1.4.1. Solution of these models with the finite element method however require a number of reformulations of the equation system, if a robust implementation is to be achieved. This work has been performed in the framework of COMSOL Multiphysics [12], which is a commercial tools featuring automatic analytic differentiation for derivation of the linearized system. It is thus able to solve custom systems of partial differential equation systems by implicit methods, even if they are very convoluted, as it is the case for reformulated viscoelastic models. The linearized equation system is also the foundation for the high-level implementation of topology optimization applied in papers [P2] and [P4].

The flow of viscoelastic fluids governed by differential constitutive equations can be predicted in commercial software, but to our knowledge these products are a bit outdated in the sense, that they do not apply the most recent model reformulation. The model implementation was thus a significant task in the beginning of the project and since we experienced an interest in our implementation from other researchers, we decided to submit paper [P1] to the International Journal for Numerical Methods in Fluids. In the paper we showcase the capabilities of our implementation outside the context of optimization with the hope of easing the implementation task for other researchers new to the modeling of viscoelastic flow. The paper includes a benchmark calculation for the flow past a confined cylinder for reference, and the ability to predict bistability is demonstrated for the cross-slot geometry. Finally the code is applied on a geometry with three inlets, which also shows bistable behavior. Another effect is however also observed as an angle in the geometry is changed beyond a certain threshold.

2.1 [P1]: Implementation of the Log-Conformation Formulation for Two-Dimensional Viscoelastic Flow

2.1.1 Abstract

We have implemented the log-conformation method for two-dimensional viscoelastic flow in COMSOL, a commercial high-level finite element package. The code is verified for an Oldroyd-B fluid flowing past a confined cylinder. We are also able to describe the well-known bistability of the viscoelastic flow in a cross-slot geometry for a FENE-CR fluid, and we describe the changes required for performing simulations with the Phan-Thien-Tanner (PTT), Giesekus and FENE-P models. Finally, we calculate the flow of a FENE-CR fluid in a geometry with three in- and outlets. The implementation is included in the supplementary material, and we hope that it can inspire new as well as experienced researchers in the field of differential constitutive equations for viscoelastic flow.

2.1.2 Introduction

The flow of viscoelastic fluids in complex geometries has many practical applications due to the fact that any dissolved elastic component, be it polymers or biological molecules, will give rise to viscoelastic effects. Such effects require the use of models that take the fluid's memory of past deformations into account. Differential constitutive equations is able to do just this, and they provide a good quantitative agreement with experiments[5]. Complex geometries call for the use of numerical methods, and therefore significant effort has been devoted towards various discretization techniques as well as model reformulations. The appearance of singularities, that caused codes to break down in smooth geometries at moderate elasticity, led to the definition of a "High Weissenberg Number Problem" (HWNP). This was effectively solved, when loss of positive definiteness for the conformation tensor was recognized as the cause of the singularity and the log-conformation method was introduced as a remedy [16].

Commercial numerical tools provide a simple workflow due to the integration of geometry description, unstructured mesh generation, discretization, solvers, and post-processing, which makes the treatment of complex geometries effortless compared to research grade code, but to our knowledge there does not exist any commercial tool that implements the log-conformation method. This is perhaps due to the fact that the method involves the calculation of eigenvectors and eigenvalues for the conformation tensor, which complicates the formulation of the constitutive equation. In two (and three) dimensions explicit expressions exists for these quantities, and it is thus possible to formulate the governing equations solely in terms of functions recognized by commercial simulation packages. We have included a COMSOL implementation of the Oldroyd-B model with log-conformation reformulation in the supplementary material, and we hope this can help other researchers working with differential constitutive equations.

The article is structured in four parts: First we discuss implementation details of the log-conformation method for the most simple constitutive equations. We then calculate the flow of an Oldroyd-B fluid past a confined cylinder using COMSOL for comparison with other works [16]. As a third point we demonstrate the ability to predict bistable behavior of a FENE-CR fluid in a cross-slot geometry [17]. Finally we consider a geometry with three in- and outlets, which has not previously been described in the context of viscoelastic flow, at least to our knowledge.

2.1.3 Log-Conformation Implementation

In the so-called dumbbell models, the elastic part of a viscoelastic fluid is approximated by two spring-connected point masses – an elastic dumbbell. The orientation and elongation of this dumbbell is described using the end-to-end vector $\mathbf{a}$ with the equilibrium length a_{eq}, see figure 2.1. The conformation tensor, $\underline{\underline{\mathbf{A}}}$, is the statistical average, $\langle ... \rangle$ of the dyadic product between

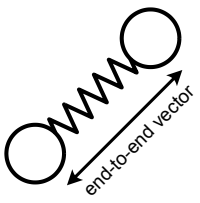

Figure 2.1: An elastic dumbbell is illustrated with its two spring-connected point masses, and the end-to-end vector describing orientation and extension.

the end-to-end vector and itself normalized with the squared equilibrium length,

$$\underline{\underline{\mathbf{A}}} = \frac{\langle \mathbf{a} \otimes \mathbf{a} \rangle}{a_{eq}^2}. \tag{2.1}$$

The equation system for the Oldroyd-B model is written below. We neglect the effect of temperature and compressibility, but keep inertia for the sake of generality.

$$\rho\frac{D\mathbf{v}}{Dt} = \boldsymbol{\nabla}\cdot\left(\overbrace{-p\underline{\underline{\mathbf{I}}}+\eta_s\left[\boldsymbol{\nabla}\mathbf{v}+(\boldsymbol{\nabla}\mathbf{v})^T\right]}^{\underline{\underline{\boldsymbol{\tau}}}_s}+\underline{\underline{\boldsymbol{\tau}}}_e\right) \tag{2.2}$$

$$\boldsymbol{\nabla}\cdot\mathbf{v} = 0 \tag{2.3}$$

$$\underline{\underline{\boldsymbol{\tau}}}_e = \frac{\eta_p}{\lambda}\left(\underline{\underline{\mathbf{A}}}-\underline{\underline{\mathbf{I}}}\right) \tag{2.4}$$

$$-\frac{1}{\lambda}(\underline{\underline{\mathbf{A}}}-\underline{\underline{\mathbf{I}}}) = \frac{D\underline{\underline{\mathbf{A}}}}{Dt}-\left[\underline{\underline{\mathbf{A}}}\cdot\boldsymbol{\nabla}\mathbf{v}+(\boldsymbol{\nabla}\mathbf{v})^T\cdot\underline{\underline{\mathbf{A}}}\right] \tag{2.5}$$

where D is the material derivative, ρ is the density, $\mathbf{v}$ is the velocity vector, t is time, p is the pressure η_s is the solvent viscosity, η_p is the elastic viscosity, λ is the relaxation time, $\underline{\underline{\boldsymbol{\tau}}}_s$ is the solvent stress tensor and $\underline{\underline{\boldsymbol{\tau}}}_e$ is the elastic stress tensor. The Navier-Stokes equation (2.2) guarantees that Newton's 2nd law is obeyed, while the continuity equation (2.3) insures mass preservation. The expression for the elastic stress tensor in equation (2.4) is best understood in light of the conformation tensor definition (2.1) with η_p/λ acting as a spring constant. The evolution of the conformation tensor is described in equation (2.5) with relaxation on the left hand side, convection by means of the total derivative and finally rotation and extension of the conformation tensor as imposed by the velocity gradient in square brackets.

When the velocity vector is approximated by C^0 continuous polynomials, the velocity gradient, $\boldsymbol{\nabla}\mathbf{v}$ becomes discontinous. This can cause numerical difficulties [18], and therefore a C^0 continuous approximation $\underline{\underline{\mathbf{G}}}$ is usually constructed for use in equation (2.5). Furthermore the zero, $\eta_p\left(\boldsymbol{\nabla}\mathbf{v}+(\boldsymbol{\nabla}\mathbf{v})^T-\underline{\underline{\mathbf{G}}}-\underline{\underline{\mathbf{G}}}^T\right)$ is added on the right-hand side of equation (2.2) to preserve the elliptic nature of the equation for small solvent viscosities in what is called the discrete elastic viscous stress splitting (DEVSS). Similarly, we use streamline upwind diffusion (SUPG) to introduce an elliptic component in the constitutive equation (2.5), see section 2.1.5.

The conformation tensor is symmetric, and the point of the log-conformation method is to exploit this property to rewrite equation (2.5) to the form

$$\frac{D\underline{\underline{\mathbf{s}}}}{Dt}-\Pi(\underline{\underline{\mathbf{s}}},\underline{\underline{\mathbf{G}}}) = 0,$$

where $\underline{\underline{\mathbf{s}}}$ is the matrix logarithm of the conformation tensor. They are related by the following expression

$$\begin{aligned}
\underline{\underline{\mathbf{A}}} &= \underline{\underline{\mathbf{R}}}\cdot e^{\underline{\underline{\mathbf{s}}}}\cdot\underline{\underline{\mathbf{R}}}^T \\
&= \begin{bmatrix} v_{1nx} & -v_{1ny} \\ v_{1ny} & v_{1nx}\end{bmatrix}\cdot\begin{bmatrix} e^{\lambda_1} & 0 \\ 0 & e^{\lambda_2}\end{bmatrix}\cdot\begin{bmatrix} v_{1nx} & v_{1ny} \\ -v_{1ny} & v_{1nx}\end{bmatrix}, \\
A_{11} &= v_{1nx}^2e^{\lambda_1}+v_{1ny}^2e^{\lambda_2} \\
A_{12} &= v_{1nx}v_{1ny}\left(e^{\lambda_1}-e^{\lambda_2}\right) \\
A_{22} &= v_{1nx}^2e^{\lambda_2}+v_{1ny}^2e^{\lambda_1}
\end{aligned}$$

where λ_1 and λ_2 are the eigenvalues of $\underline{\underline{\mathbf{s}}}$, while v_{1nx} and v_{1ny} are the normalized eigenvector components belonging to λ_1. The orthonormal rotation matrix, $\underline{\underline{\mathbf{R}}}$ holds the components of the eigenvectors, but we exploit that the second eigenvector is just the transpose of the first.

Denoting the components of $\underline{\underline{\mathbf{s}}}$ by s_{11}, s_{12} and s_{22}, the eigenvalues become[1]

$$\begin{aligned}\lambda_1 &= \frac{1}{2}\left(s_{22}+s_{11}-\sqrt{(s_{22}-s_{11})^2+4s_{12}^2}\right) \quad \text{and}\\ \lambda_2 &= \frac{1}{2}\left(s_{22}+s_{11}+\sqrt{(s_{22}-s_{11})^2+4s_{12}^2}\right),\end{aligned}$$

and the components of the first eigenvector is

$$\mathbf{v}_1 = \begin{bmatrix} \lambda_1 - s_{22} \\ s_{12} \end{bmatrix}.$$

The eigenvector is normalized

$$\mathbf{v}_{1\mathrm{n}} = \begin{bmatrix} v_{1x} \Big/ \sqrt{\mathbf{v}_{1x}^2+\mathbf{v}_{1y}^2} \\ v_{1y} \Big/ \sqrt{\mathbf{v}_{1x}^2+\mathbf{v}_{1y}^2} \end{bmatrix}.$$

The special case $s_{12}=0$ is handled by using $\underline{\underline{\mathbf{R}}} = \underline{\underline{\mathbf{I}}}$, when $|s_{12}| \leq \epsilon$ with $\epsilon = 10^{-12}$.

In the following we will express the reaction term $\underline{\underline{\mathbf{\Pi}}}$ as $\underline{\underline{\mathbf{R}}} \cdot \underline{\underline{\mathbf{\Omega}}} \cdot \underline{\underline{\mathbf{R}}}^T$ as described in [19]. The continuous velocity gradient is rewritten in the principal frame

$$\begin{aligned}\underline{\underline{\tilde{\mathbf{G}}}} &= \underline{\underline{\mathbf{R}}}^T \cdot \underline{\underline{\mathbf{G}}} \cdot \underline{\underline{\mathbf{R}}}\\ \tilde{\mathrm{G}}_{11} &= \mathbf{v}_{1nx}^2 \mathrm{G}_{11} + \mathbf{v}_{1nx}\mathbf{v}_{1yx}(\mathrm{G}_{12}+\mathrm{G}_{21}) + \mathbf{v}_{1ny}^2 \mathrm{G}_{22}\\ \tilde{\mathrm{G}}_{12} &= \mathbf{v}_{1nx}^2 \mathrm{G}_{21} + \mathbf{v}_{1nx}\mathbf{v}_{1yx}(\mathrm{G}_{22}-\mathrm{G}_{11}) - \mathbf{v}_{1ny}^2 \mathrm{G}_{12}\\ \tilde{\mathrm{G}}_{21} &= \mathbf{v}_{1nx}^2 \mathrm{G}_{12} + \mathbf{v}_{1nx}\mathbf{v}_{1yx}(\mathrm{G}_{22}-\mathrm{G}_{11}) - \mathbf{v}_{1ny}^2 \mathrm{G}_{21}\\ \tilde{\mathrm{G}}_{22} &= \mathbf{v}_{1nx}^2 \mathrm{G}_{22} - \mathbf{v}_{1nx}\mathbf{v}_{1yx}(\mathrm{G}_{12}-\mathrm{G}_{21}) + \mathbf{v}_{1ny}^2 \mathrm{G}_{11}.\end{aligned}$$

Note that this matrix is not symmetric, and that we have chosen G_{12} to refer to the derivative of the velocity vector x-component with respect to the y-coordinate. The diagonal components Ω_{11} and Ω_{22} are

$$\Omega_{11} = 2\tilde{\mathrm{G}}_{11} - \frac{e^{\lambda_1}-1}{\lambda} \quad \text{and}$$
$$\Omega_{22} = 2\tilde{\mathrm{G}}_{22} - \frac{e^{\lambda_2}-1}{\lambda}.$$

These expressions are specific to the Oldroyd-B model, but it is straight forward to write the expressions for the Giesekus, Phan-Thien-Tanner, FENE-P or FENE-CR models instead [19].

$$\begin{aligned}
\text{Giesekus} \quad &: \quad \begin{aligned}\Omega_{11} &= 2\tilde{\mathrm{G}}_{11} - \tfrac{1+\alpha_{\mathrm{Gie.}}(e^{\lambda_1}-1)}{\lambda}(e^{\lambda_1}-1)\\ \Omega_{22} &= 2\tilde{\mathrm{G}}_{22} - \tfrac{1+\alpha_{\mathrm{Gie.}}(e^{\lambda_2}-1)}{\lambda}(e^{\lambda_2}-1)\end{aligned}\\
\text{PTT(exp.)} \quad &: \quad \begin{aligned}\Omega_{11} &= 2\tilde{\mathrm{G}}_{11} - \tfrac{k_{\mathrm{PTT}}(\lambda_1,\lambda_2)}{\lambda}\\ \Omega_{22} &= 2\tilde{\mathrm{G}}_{22} - \tfrac{k_{\mathrm{PTT}}(\lambda_1,\lambda_2)}{\lambda}\end{aligned} \text{, where} \quad k_{\mathrm{PTT}}(\lambda_1,\lambda_2) = e^{\epsilon_{\mathrm{PTT}}(\lambda_1+\lambda_2-3)}\\
\mathrm{FENE-P} \quad &: \quad \begin{aligned}\Omega_{11} &= 2\tilde{\mathrm{G}}_{11} - \tfrac{k(\lambda_1,\lambda_2)e^{\lambda_1}-1}{\lambda}\\ \Omega_{22} &= 2\tilde{\mathrm{G}}_{22} - \tfrac{k(\lambda_1,\lambda_2)e^{\lambda_2}-1}{\lambda}\end{aligned} \text{, where} \quad k(\lambda_1,\lambda_2) = \frac{1}{1-(\lambda_1+\lambda_2)/L^2}\\
\mathrm{FENE-CR} \quad &: \quad \begin{aligned}\Omega_{11} &= 2\tilde{\mathrm{G}}_{11} - k(\lambda_1,\lambda_2)\tfrac{e^{\lambda_1}-1}{\lambda}\\ \Omega_{22} &= 2\tilde{\mathrm{G}}_{22} - k(\lambda_1,\lambda_2)\tfrac{e^{\lambda_2}-1}{\lambda}\end{aligned} \text{, where} \quad k(\lambda_1,\lambda_2) = \frac{1}{1-(\lambda_1+\lambda_2)/L^2}
\end{aligned}$$

[1] There also exist explicit expressions for the three-dimensional case.

The off-diagonal component, Ω_{12}, equals

$$\Omega_{12} = \begin{cases} \left(\frac{\lambda_1-\lambda_2}{e^{\lambda_1}-e^{\lambda_2}}\right)\left(e^{\lambda_1}\tilde{\mathrm{G}}_{12} + e^{\lambda_2}\tilde{\mathrm{G}}_{21}\right) & ,|\lambda_1-\lambda_2| > \epsilon \\ \tilde{\mathrm{G}}_{12} + \tilde{\mathrm{G}}_{21} & ,|\lambda_1-\lambda_2| \leq \epsilon \end{cases},$$

where we have reused the numerical parameter for the eigenvectors to handle the special case of identical eigenvalues. We are now ready to compute the reaction term

$$\begin{aligned} \Pi_{11} &= v_{1nx}^2\Omega_{11} - 2v_{1nx}v_{1ny}\Omega_{12} + v_{1ny}^2\Omega_{22} \\ \Pi_{12} &= \left(v_{1nx}^2 - v_{1ny}^2\right)\Omega_{12} + v_{1nx}v_{1ny}(\Omega_{11}-\Omega_{22}) \\ \Pi_{22} &= v_{1nx}^2\Omega_{22} + 2v_{1nx}v_{1ny}\Omega_{12} + v_{1ny}^2\Omega_{11} \end{aligned}$$

To ease modification of the implementation, we have opted to construct functions for each of the above expressions instead of writing out $\underline{\underline{\mathbf{\Pi}}}$ in terms of expressions involving $\underline{\underline{\mathbf{s}}}$ only.

2.1.4 Non-Dimensional Equations

We define the dimensionless spatial coordinates, velocity, time, pressure and stress ($\tilde{x}$, $\tilde{v}$, $\tilde{t}$, $\tilde{p}$ and $\underline{\underline{\tilde{\boldsymbol{\tau}}}}_e$),

$$\begin{aligned} \mathbf{x} = L_{\mathrm{char}}\tilde{\mathbf{x}}, \quad \mathbf{v} &= v_{\mathrm{char}}\tilde{\mathbf{v}}, \quad t = \frac{L_{\mathrm{char}}}{v_{\mathrm{char}}}\tilde{t}, \quad p = \frac{v_{\mathrm{char}}(\eta_s+\eta_p)}{L_{\mathrm{char}}}\tilde{p} \\ \text{and} \quad \underline{\underline{\boldsymbol{\tau}}}_e &= (\eta_s+\eta_p)\frac{v_{\mathrm{char}}}{L_{\mathrm{char}}}\underline{\underline{\tilde{\boldsymbol{\tau}}}}_e, \end{aligned}$$

which give rise to the following dimensionless constants

$$\mathrm{Re} = \frac{\rho v_{\mathrm{char}}L_{\mathrm{char}}}{\eta}, \quad \mathrm{We} = \lambda\frac{v_{\mathrm{char}}}{L_{\mathrm{char}}} \quad \text{and} \quad \beta = \frac{\eta_s}{\eta_p+\eta_s},$$

The Weissenberg number, We, describes the magnitude of elastic to viscous effects. When either the Weissenberg number goes to zero or the solvent to total viscosity ratio, β goes to unity, the model approaches that of a Newtonian fluid. Contrarily, the value $\beta = 0$ corresponds to the upper convected Maxwell model, which is characterized by particularly strong viscoelastic effects. Note that we favor a defining a characteristic pressure in terms of a characteristic velocity rather than the other way around due the fact that we intend to impose fixed flow rates rather than fixed driving pressures (as in [20]).

We have implemented the above approach to the log-conformation formulation for two dimensions in COMSOL Multiphysics version 4.3a, and the online version of the manuscript includes a MATLAB script for computation of the flow of an Oldroyd-B fluid past a confined cylinder using the COMSOL LiveLink interface. We use default settings for everything, except we force update of the Jacobian every time a time step is saved.

2.1.5 The Oldroyd-B model in Weak Form

Converting the strong form of the Oldroyd-B model (2.2-2.5) to weak form is trivial for the equations that relate to the elastic stress (2.4) and continuity equation (2.3) as one just multiplies with test functions for the elastic stress and pressure, respectively. The evolution equation for the conformation tensor (2.5) requires SUPG stabilization, which means that the equation is multiplied[2] with $\underline{\underline{\mathbf{A}}}_{\mathrm{test}} + (2h_{\mathrm{mesh}}/v_{\mathrm{char}})\mathbf{v}\cdot\boldsymbol{\nabla}\underline{\underline{\mathbf{A}}}_{\mathrm{test}}$ rather than $\underline{\underline{\mathbf{A}}}_{\mathrm{test}}$, where h_{mesh} is a characteristic

[2]Note that the test functions for elastic stress and conformation tensor are multiplied element wise (Hadamard product), denoted with $\circ$.

size for the mesh. In other words a small amount of stream-wise diffusion is added to allow computation, but since the amount of diffusion is scaled with the mesh, the implementation still converges towards the solution without any artificial diffusion. Finally there is the momentum part of the Navier-Stokes equation (2.2), which is multiplied with a test function for the velocity and integrated by parts:

$$\begin{aligned} 0 &= \int_\Omega \left\{ \tilde{\boldsymbol{\nabla}} \cdot \left(\underline{\underline{\tilde{\boldsymbol{\tau}}}}_s + \underline{\underline{\tilde{\boldsymbol{\tau}}}}_e \right) - \mathrm{Re} \frac{D\tilde{\mathbf{v}}}{D\tilde{t}} \right\} \cdot \tilde{\mathbf{v}}_{\mathrm{test}} d\Omega \\ 0 &= -\int_\Omega \underline{\underline{\tilde{\boldsymbol{\tau}}}}_s \circ \tilde{\boldsymbol{\nabla}}\, \tilde{\mathbf{v}}_{\mathrm{test}} d\Omega \qquad (2.6) \\ &+ \int_\Omega \left\{ \tilde{\boldsymbol{\nabla}} \underline{\underline{\tilde{\boldsymbol{\tau}}}}_e - \mathrm{Re} \frac{D\tilde{\mathbf{v}}}{D\tilde{t}} - \mathrm{Da}^{-1} \tilde{\alpha} \tilde{\mathbf{v}} \right\} \cdot \tilde{\mathbf{v}}_{\mathrm{test}} d\Omega \\ &+ \int_{\partial\Omega} \underline{\underline{\tilde{\boldsymbol{\tau}}}}_s \cdot \hat{\mathbf{n}} \cdot \tilde{\mathbf{v}}_{\mathrm{test}} dl \qquad (2.7) \end{aligned}$$

The point is that the solvent stress is integrated by parts (Divergence theorem), but the elastic stress is not. This approach has been followed by other researchers so we have adopted it as well. The advantage is that the specification of $\underline{\underline{\tilde{\boldsymbol{\tau}}}}_s$ on open boundaries is slightly more simple than $\underline{\underline{\tilde{\boldsymbol{\tau}}}}_s + \underline{\underline{\tilde{\boldsymbol{\tau}}}}_e$, but in fact we have tested both without finding any difference. At outlets we thus usually impose normal velocity, zero pressure and

$$\underline{\underline{\tilde{\boldsymbol{\tau}}}}_s = -\underline{\underline{\mathbf{I}}} \tilde{p}.$$

This can also be used for pressure driven inlets, but in that case one should supplement the constraint on the velocity with one on the conformation tensor. We impose the no-slip($\tilde{\mathbf{v}} = \mathbf{0}$) at walls, which causes COMSOL to automatically enforce $\tilde{\mathbf{v}}_{\mathrm{test}} = 0$, such that the boundary integral in equation (2.7) vanishes.

2.1.6 Confined Cylinder

The confined cylinder geometry is shown in figure 2.2, and it is a popular benchmark geometry due to the absence of geometric singularities. It can be used to verify an implementation by comparing the drag over the cylinder with a reference. We exploit the symmetry of the problem by modeling only half of the domain.

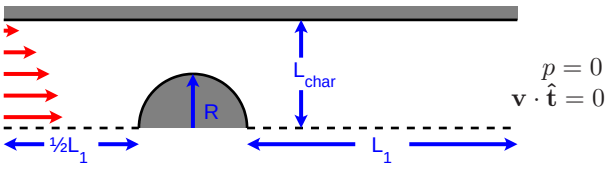

Figure 2.2: The confined cylinder geometry with a (dashed) symmetry axis. The fluid comes in from the left, flows past the obstacle and exits through the boundary on the right ($\hat{\mathbf{t}}$ is the unit tangent vector).

The cylinder radius R, and average inlet velocity are used as characteristic length and velocity, respectively. The blocking ratio is set at 2 ($H = 2R$), and the outlet length, L_1, is fixed at $10R$. In agreement with references [16] the solvent to total viscosity ratio is taken as 0.59, and inertia is neglected ($\mathrm{Re} = 0$). The dimensionless drag is computed as

$$\begin{aligned} \mathrm{Drag} &= -2 \int_{\mathrm{cylinder}} \tilde{\boldsymbol{\tau}} \cdot \hat{\mathbf{n}} \cdot \hat{\mathbf{x}}^T dl, \quad \text{with} \\ \underline{\underline{\tilde{\boldsymbol{\tau}}}} &= -\tilde{p} \underline{\underline{\mathbf{I}}} + \eta_s \left[\tilde{\boldsymbol{\nabla}} \tilde{\mathbf{v}} + (\tilde{\boldsymbol{\nabla}} \tilde{\mathbf{v}})^T \right] + \underline{\underline{\tilde{\boldsymbol{\tau}}}}_e \end{aligned}$$

where $\hat{\mathbf{n}}$ is the outward pointing normal vector.

We impose the no-slip boundary condition $\tilde{\mathbf{v}} = \mathbf{0}$ at the walls, and fully developed boundary conditions at the inlet

$$\begin{aligned}
\tilde{\mathbf{v}}_{\text{inlet}} &= \tfrac{3}{2}\left(1-(\tilde{y}/2)^2\right)\hat{\mathbf{x}} \\
A_{11,\text{inlet}} &= 1+2\left(\frac{\partial\left(\tilde{\mathbf{v}}\cdot\hat{\mathbf{x}}\right)}{\partial\tilde{y}}\text{We}\right)^2 = 1+\tfrac{9}{8}\tilde{y}^2\text{We}^2 \\
A_{12,\text{inlet}} &= \text{We}\frac{\partial\left(\tilde{\mathbf{v}}\cdot\hat{\mathbf{x}}\right)}{\partial\tilde{y}} = -\tfrac{3}{4}\tilde{y}\text{We} \quad \text{and} \quad A_{22,\text{inlet}} = 1
\end{aligned}$$

Note that the intermediate expressions can be used in the case of a pressure driven setup. At the outlet we impose zero pressure together with zero normal viscous stress.

$$p_{\text{outlet}} = 0 \quad \text{and} \quad \underline{\underline{\tilde{\boldsymbol{\tau}}}}_{s,\text{outlet}}\cdot\hat{\mathbf{n}} = \left(-\underline{\underline{\mathbf{I}}}p\right)\cdot\hat{\mathbf{n}} = 0 \tag{2.8}$$

At the symmetry line we impose zero normal velocity.

$$\tilde{\mathbf{v}}_{\text{sym}}\cdot\hat{\mathbf{n}} = 0 \tag{2.9}$$

2.1.7 Solution Details

In order to find a steady solution one can go through the following steps.

#1 Solve for the case of a Newtonian fluid.

#2 Use #1 as initial condition for a transient simulation running for 10 relaxation times.

#3 Use #2 as initial guess for a non-linear solver to find a steady solution.

We however choose to vary the Weissenberg number slowly using a regularized step function, st, such that a quasi steady state is achieved.

$$\begin{aligned}
\text{We} &= \text{We}_{\text{start}} + (\text{We}_{\text{end}} - \text{We}_{\text{start}})\,\text{st}(\tilde{t}), \quad \text{where} \\
\text{st}(\tilde{t}) &= \begin{cases} 0 & , \quad \tilde{t} < \tilde{t}_{\text{start}} \\ 0.5 + 1.5\bar{t} - 2\bar{t}^3 & , \tilde{t}_{\text{start}} \le \tilde{t} < \tilde{t}_{\text{end}} \\ 1 & , \tilde{t}_{\text{end}} \le \tilde{t} \end{cases}, \quad \text{and} \\
\bar{t} &= \frac{\tilde{t} - (\tilde{t}_{\text{start}} + \tilde{t}_{\text{end}})/2}{\tilde{t}_{\text{end}} - \tilde{t}_{\text{start}}}
\end{aligned} \tag{2.10}$$

This way we compute a quasi-steady solution to a range of Weissenberg numbers using a single transient simulation. COMSOL uses a fully implicit transient scheme with adaptive stepsize, so slow variation of the Weissenberg number does not increase the total computation time [21].

2.1.8 Results

Since the time over which the Weissenberg number is varied is a numerical parameter, we choose to scale it with the mesh size, so convergence towards the steady case is achieved, i.e.

$$T_{\text{step}} = \tilde{t}_{\text{end}} - \tilde{t}_{\text{start}} = 8000(0.07/h_{\text{mesh}})$$

Figure 2.3 shows the drag as a function of the Weissenberg number for three different discretizations indicating convergence up to We = 0.6. We observe good agreement with the reference drag although the simplicity of the chosen mesh gives rise to a high computational cost. It

is well known, that convergence at We = 0.7 is difficult, even with anisotropic mesh adaption [22]. In fact experimental [23] as well as theoretical evidence [24] exist to suggest, that a transition to a three dimensional flow pattern occurs, in other words the two dimensional symmetric flow becomes unstable. The three-dimensional solution has the flow alternating between going above and below the cylinder, and one can think of this solution as having a weaker extensional character in the wake of the cylinder.

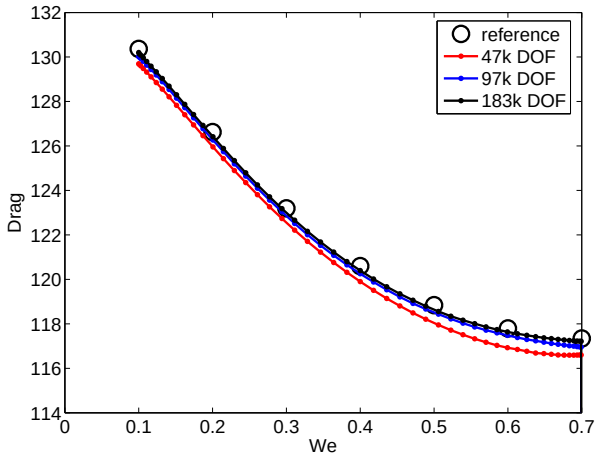

Figure 2.3: The drag on a confined cylinder is plotted as a function of the Weissenberg number for three discretizations together with the data of another study [16].

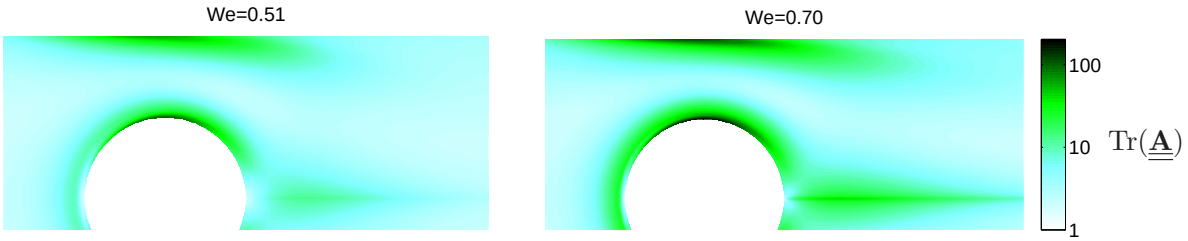

Figure 2.4: The trace of the conformation tensor is plotted on a logarithmic scale for the confined cylinder in the case of We = 0.51 and We = 0.7 (183k DOF). The acceleration of the flow in the wake of the cylinder generates a strand of highly elongated dumbbells.

When a viscoelastic fluid enters a region, where the extension rate times the relaxation time reaches a critical value, the dumbbell extension starts to grow exponentially in time. This kind of non-linearity explains the significant difference between the wake of extension at We = 0.51 and We = 0.7 illustrated in figure 2.4.

2.1.9 Bistable Cross-Slot

The FENE-CR model differs from the Oldroyd-B model in the sense, that λ is replaced by $\lambda\left[1 - \text{Trace}(\underline{\underline{\mathbf{A}}})/a^2_{\max}\right]$. In other words the relaxation time decreases as the dumbbell extension increases. This puts an upper bound $a^2_{\max}$, on the trace of the conformation tensor corresponding to a maximum extension. The modification prevents an unbounded extension in free stagnation points such as the center of the cross-slot geometry shown in figure 2.5. This geometry is known to exhibit bistability experimentally [25] as well as numerically [13].

In this case we keep the average inlet velocity as characteristic velocity and the channel width H as characteristic length scale. We impose the no-slip boundary condition at walls,

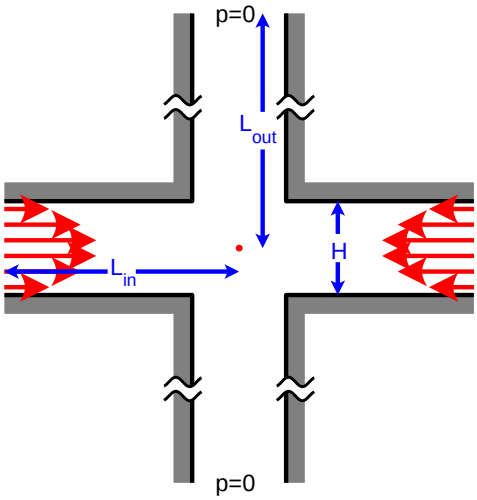

Figure 2.5: The cross-slot geometry is shown with the fluid coming in from the left and right, diverging at the center, before exiting through to the upper and lower outlets leaving a free stagnation point (red) in the center of the geometry.

but we have been unable to initialize the transient simulation with the correct expressions for the conformation tensor at the inlets. Therefore we have used $\underline{\underline{\mathbf{s}}} = \epsilon\underline{\underline{\mathbf{I}}}$ at the inlets rather than values based on the expressions listed in Appendix I. Furthermore we had to change the damping strategy of the nonlinear method from the default (constant) to automatic.

At the outlet we impose the same boundary conditions (2.8) as for the cylinder. We compute the dissipation as an integral over the entire computation domain,

$$\tilde{\phi} = \int_{\Omega} \underline{\underline{\tilde{\boldsymbol{\tau}}}} : \left[\tilde{\boldsymbol{\nabla}}\tilde{\mathbf{v}} + (\tilde{\boldsymbol{\nabla}}\tilde{\mathbf{v}})^T \right] d\Omega. \tag{2.11}$$

where : is the Frobenius product. We choose $\mathrm{Re} = 0$, $\mathrm{a}^2_{\max} = 100$ and $\beta = 0.2$ and the same transient solution procedure as described in section 2.1.7. We define the center of the domain,

$$\Omega_c \quad = \quad \tilde{\mathbf{x}} \in |\tilde{\mathbf{x}}|_\infty < 0.5,$$

as we find that the vorticity integrated over this is a good asymmetry parameter. We thus plot the square of this versus the Weissenberg number in figure 2.6(a). The system becomes bistable at $\mathrm{We} = 0.5$[3], which gives rise to a kink in the dissipation as shown in figure 2.6(b). The solution before the kink [figure 2.7(a) and (d)] has vertical, horizontal as well as 180-degree rotational symmetry, while the solutions after the kink [2.7(b), (c), (e) and (f)] only have 180-degree rotational symmetry, and we will refer to these solutions with reduced symmetry as "asymmetric solutions". The phenomenon can be understood by considering the velocity magnitude and conformation tensor trace as plotted in figures 2.7(a-c) and (d-e) respectively. The dumbbells are extended along the vertical axis, which causes a damping that delays the merging of the flows, and this gives rise to extra shear and thus also dissipation. When the solution becomes asymmetric, the damping is moved to the side of the channel, which lowers the dissipation. One can also think of the asymmetry as a flow pattern with less extension in the stagnation point, similar to the three-dimensional flow for the confined cylinder.

[3]Based on personal correspondence we have concluded that the results of [17] are based on the FENE-MCR model, so no reference exists for the FENE-CR model.

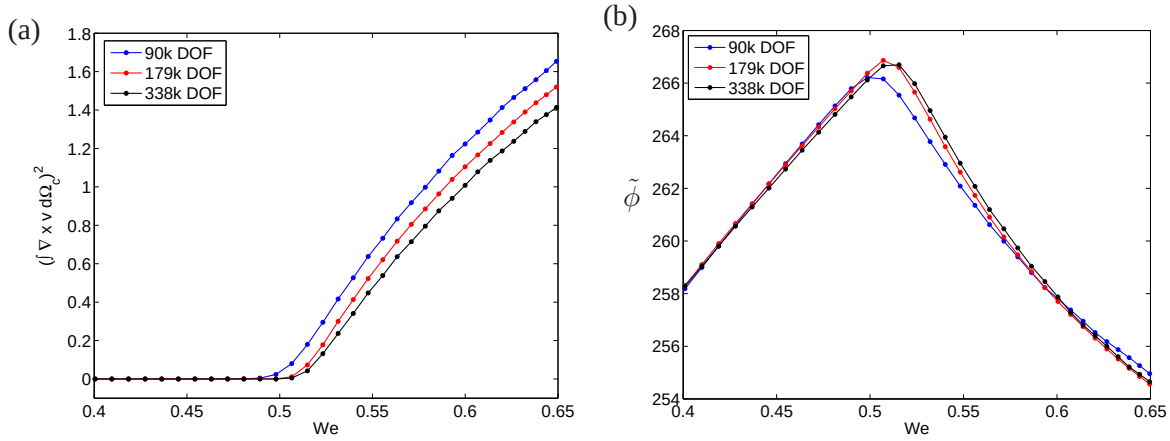

Figure 2.6: The square of the vorticity integrated over the center of the domain Ω_c is plotted as function of the Weissenberg number in (a), and so is the dissipation in (b). The point of bistability occurs at We = 0.5, which is also the point of maximum dissipation (and hydraulic resistance).

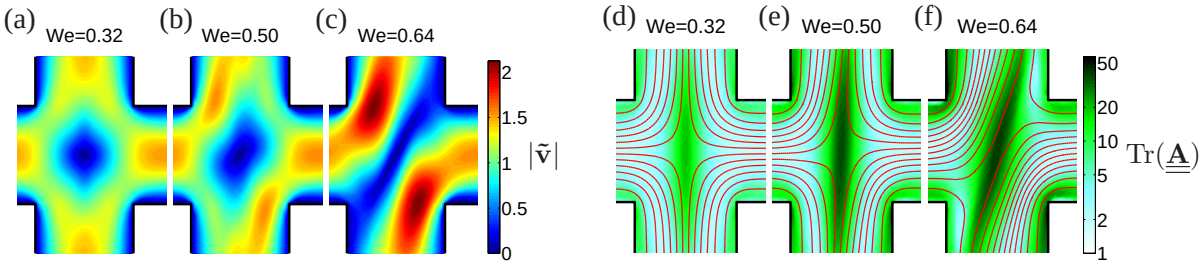

Figure 2.7: The magnitude of the velocity vector is plotted for three Weissenberg numbers in the cross geometry in (a-c), while red stream lines are plotted on top of the trace of the conformation tensor on a logarithmic scale in (d-f). Note that we plot streamlines as contours of the stream function instead of integrating the velocity field.

2.1.10 Three Inlets

In this section we introduce the geometry shown in figure 2.8. It consists of a hexagon with in- and outlets attached in an alternating fashion. The geometry always has a vertical symmetry axis, but depending on whether a certain angle is equal to $\pi/3$ or not, it can also have 120-degree rotational symmetry. We define the distance to the center as in- and outlet lengths, and set equal inlet flow rates as well as outlet pressures. We set $L_{\text{in}} = 6H$ and $L_{\text{out}} = 8L$, $\beta = 0.1$ and $\underline{\underline{\mathbf{s}}} = \epsilon \underline{\underline{\mathbf{I}}}$ at the inlets, but keep all other parameters identical to those used for the cross-slot. That is, the channel width and average inlet velocity are still used as characteristic length and velocity, respectively.

If the angle is equal to $\pi/3$ radians, a single stagnation point exists in the center of the geometry regardless of whether we consider Stokes flow or just the regime of low elasticity. Two stagnation points however appear, if the angle is different from $\pi/3$ radians. Figure 2.9 shows the solution for angles of $\pi/3$, $\pi/3.5$ and $\pi/4$ radians at We = 0.37 (low) and We = 0.66 (moderate). For an angle of $\pi/3$ radians, the regime of low elasticity (a) gives a solution with 120-degree rotational- and vertical symmetry, while for moderate elasticity a solution with only 120-degree rotation symmetry appears (b). This latter solution involves the clockwise flow, but by symmetry we can argue that there must be an identical solution with counter-clockwise flow. The symmetry reduction also occurs for an angle of $\pi/3.5$ (c-d), in the sense that we go from only vertical symmetry to no symmetry. Regardless of the Weissenberg number, there are two

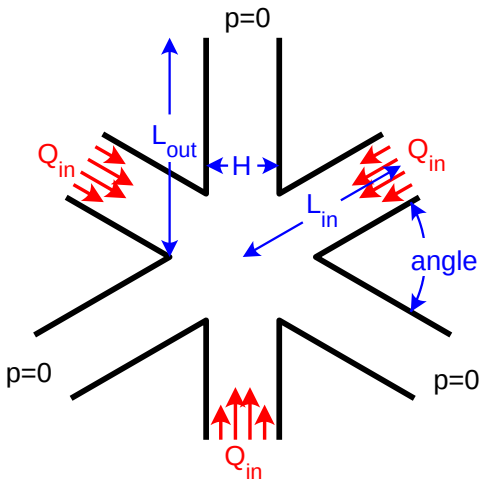

Figure 2.8: The geometry with three in- and outlets is illustrated with the different length scales and angles involved. For an angle of $\pi/3$ the geometry has a symmetry axis through every channel as well as 120-degree rotational symmetry, while an angle different from $\pi/3$ breaks all symmetries except the one around the vertical axis.

stagnations points even though the flow rate between them is small at moderate elasticity (d). In other words turning up the elasticity causes the flow rate between the stagnation points to decrease significantly. As shown in (e-f) this is different for an angle of $\pi/4$ radians, as the elasticity tends to move the stagnation points apart and increase the flow rate between them in what we call the "straight flow solution", that is the solution has identical symmetry properties at low and moderate elasticity.

Using artificial initial conditions as listed in Appendix II, one can show that the clockwise, counter-clockwise and the straight flow all exist as stable solutions at moderate elasticity for angles between $\pi/4$ and $\pi/3.5$. This means, that it is the connectivity with the solution at low elasticity that changes. Furthermore there is an unstable solution with a vertical symmetry axis for the angles $\pi/3$ and $\pi/3.5$. We calculate the integral of the vorticity around the center

$$\Omega_o \quad = \quad \mathbf{x} \in ||x||_2 < 0.5,$$

as a measure of asymmetry and plot this as a function of the Weissenberg number for five angles in figure 2.10 (a), while the dissipation is plotted in figure 2.10 (b). It is clear that the point of maximum dissipation coincides with the point of bistability for the three largest angles ($\pi/3$, $\pi/3.5$, $\pi/3.75$), as it was also the case for the cross-slot in section 2.1.9. The dissipation for the two smaller angles also have maxima, but we do not believe they play the same role as the maxima for the smaller angles. This is due to the fact that the Weissenberg number at which the maximum occurs seems to decreases for both the rotation and straight flow solutions. This means that there does not exists an angle for which the two kind of maxima in figure 2.10 (b) meet, although there must exist an angle where all three solutions are connected to the solution at low elasticity.

2.1.11 Conclusion

We have described the viscoelastic Oldroyd-B model with log-conformation reformulation in detail, and included a COMSOL implementation in the supplementary material. We have showed, that the code agrees with a reference in a benchmark geometry. Furthermore we have demonstrated that the code can be modified to describe the flow of a FENE-CR fluid, and that it can

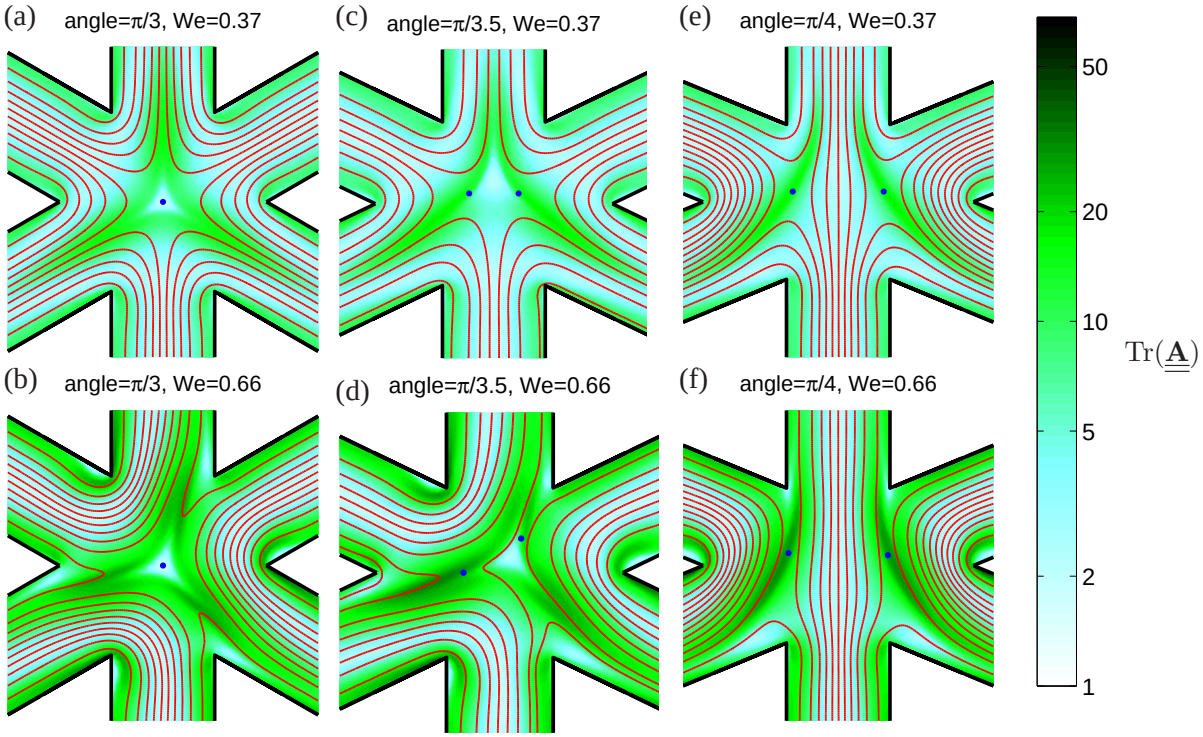

Figure 2.9: The trace of the conformation tensor is plotted on a logarithmic scale together with streamlines (red) for two Weissenberg numbers in a geometry with three inlets. The case of an angle equal to $\pi/3$ (a-b), $\pi/3.5$ (c-d) and $\pi/4$ (d-e) radians is illustrated (see figure 2.8). Although not apparent from the streamlines, the upper outlet receives fluid from all three inlets in (d), and the flow between the stagnation points is reduced with a factor of 4.5 in (d) compared to (c).

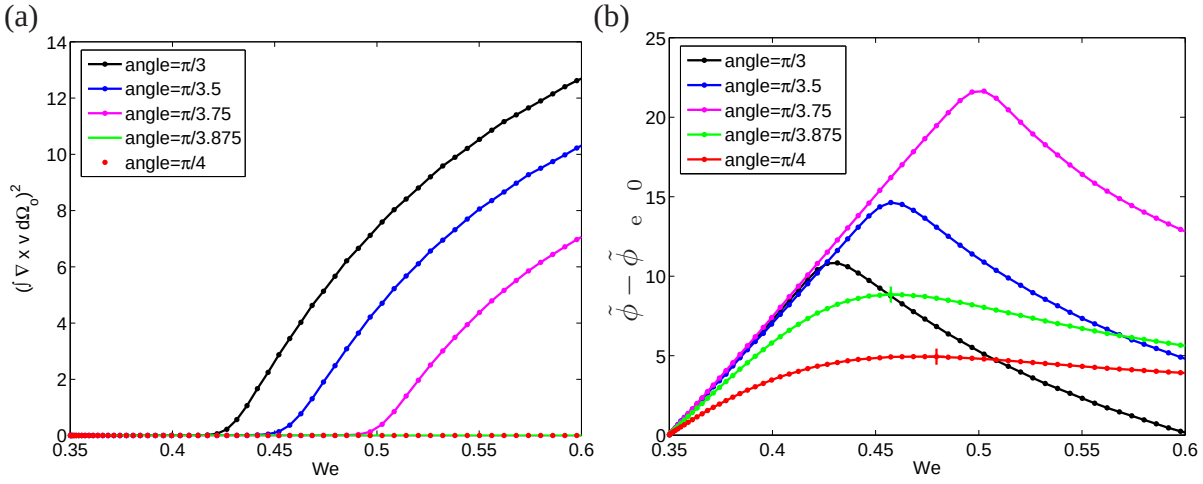

Figure 2.10: The square of the vorticity integrated over the center of the domain Ω_o is plotted as functions of the Weissenberg number for five different angles in (a), while the dissipation is shown (b). The point of bistability coincides with the point of maximum dissipation for the three larger angles, as it was also the case for the cross-slot in figure 2.6. The maximum dissipation of the two smaller angles is indicated with crosses.

reproduce bistability in the cross-slot geometry. Finally we computed the flow in a geometry with three in- and outlets, which appears to feature three stable solutions. The connectivity of

the solutions with the solution at low elasticity seems to depend on an angle in the geometry.

Appendix I: FENE-CR Inlet Conditions

The developed flow conditions for a FENE-CR fluid [4] is listed in the following equations

$$\begin{aligned}
\tilde{\mathbf{v}}_{\text{inlet}} &= -\tfrac{3}{2}\left(1-(\tilde{y}/2)^2\right)\hat{\mathbf{n}} \\
A_{11,\text{inlet}} &= a_{\max}^2 - 1 \\
&+ \frac{a_{\max}^2\left(a_{\max}^2 - \sqrt{a_{\max}^4 + 8\chi^2(a_{\max}^2-2)}\right)}{4\chi^2} \\
A_{12,\text{inlet}} &= \chi\left(1 - \frac{A_{11,\text{inlet}}+1}{a_{\max}^2}\right) \\
A_{22,\text{inlet}} &= 1, \quad \text{where} \quad \chi = \text{We}\frac{\partial\left(\tilde{\mathbf{v}}\cdot\hat{\mathbf{x}}\right)}{\partial\tilde{y}} = 3\text{We}(\tilde{y}/4)(\hat{\mathbf{n}}\cdot\hat{\mathbf{x}})
\end{aligned}$$

Appendix II: Artificial Initial Conditions for the Geometry with Three In- and Outlets

One can find stable solutions not connected to the solution at low elasticity using artificial initial conditions. A rotating solution for an angle of $\pi/4$ (see figure 2.8) can in example be found by imposing a rotating force in the center of the geometry,

$$\mathbf{F}^{\circlearrowleft} = \begin{cases} (\hat{\mathbf{x}}\tilde{y} - \hat{\mathbf{y}}\tilde{x})/2 & , \quad ||\tilde{\mathbf{r}}|| \leq 0.5/\sin(\pi/6) \\ 0 & , \quad ||\tilde{\mathbf{r}}|| > 0.5/\sin(\pi/6) \end{cases},$$

where $\tilde{\mathbf{r}}$ is the position vector and $||\cdots||$ is the euclidean norm. This is then multiplied with a step function as given by equation (2.10), such that the force vanishes beyond some critical time. Alternatively one might find a solution going straight through a geometry with an angle of $\pi/3.5$ using an upward force,

$$\mathbf{F}^{\uparrow} = \begin{cases} \hat{\mathbf{y}}(0.25 - \tilde{x}^2) & , \quad ||\tilde{\mathbf{r}}|| \leq 0.5/\sin(\pi/6) \\ 0 & , \quad ||\tilde{\mathbf{r}}|| > 0.5/\sin(\pi/6) \end{cases}.$$

[4] Note that one has to set $A_{11,\text{inlet}} = 1$ when $\chi^2 < \epsilon$.

Chapter 3

Topology Optimization of Anisotropic Flow Resistance

3.1 Topology Optimization

The formulation of an optimization problem involves definition of design variables, $\boldsymbol{\theta}$ and an objective function, ϕ, which by convention should be minimized. This is often supplemented with equality and/or inequality constraints. As the name suggests topology optimization is capable of introducing and removing holes in a design such that the topology changes. This property is related to the definition of the design variables as a field, i.e. the number of design variables scales with the number of degrees of freedom used to represent the physical variables. We will denote these with $\mathbf{c}$, and they could be velocity and pressure for a flow problem. A rather general optimization problem could thus be formulated as [the next section on filters contains a concrete example (3.4)]

$$\min_{\boldsymbol{\theta}}(\phi[\mathbf{c}(\boldsymbol{\theta}), \boldsymbol{\theta}]), \quad \text{subject to} \tag{3.1a}$$

$$\mathbf{G}(\mathbf{c}(\boldsymbol{\theta})) = \mathbf{0}, \tag{3.1b}$$

$$\mathbf{H}(\mathbf{c}(\boldsymbol{\theta}), \boldsymbol{\theta}) \leq \mathbf{0} \quad \text{and} \tag{3.1c}$$

$$\boldsymbol{\theta}_{\min} \leq \boldsymbol{\theta} \leq \boldsymbol{\theta}_{\max}. \tag{3.1d}$$

In the context of topology optimization $\mathbf{G}$ would often be the (linearized) governing equation, while $\mathbf{H}$ could be a constraint on the amount of allowable material, i.e. drag reduction calls for a minimum of material, while structural compliance minimization calls for an upper bound. It is conventional to restrict the design variables to values between 0 and 1 using $\boldsymbol{\theta}_{\min}$ and $\boldsymbol{\theta}_{\max}$. In the context of structural problems, $\theta = 0$ corresponds to void, while $\theta = 1$ corresponds to solid, but the convention is opposite for fluid problems [26]. It is often straight forward to reproduce the governing equation in one of the extreme values of θ, but the other extreme is often an approximation, i.e. structural problems often approximate void with an extremely flexible material, while the solid regions are approximated with a very low permeability sponge in fluid problems. The interpolation between these two extremes is tricky, and it is has a strong influence on the convergence of the optimization.

Level-set methods can be used for topology optimization in different ways, one of which involves the introduction of a fictitious time such that the optimization can be performed as a time evolution which makes the approach well suited for high-level implementations [27], at least in comparison with methods that use mathematical optimizers. One can use these optimizers to solve the optimization problem together with the governing equation (3.1) in what is called

simultaneous analysis and design (SAND). This treats design and physical variables similarly, but it is more popular to separate them such that the optimizer is only allowed to change the design variables in what is called a *nested formulation*, which requires the formulation of an adjoint problem for the equality constrained optimization problem as well as one for each of the inequalities. The point of the adjoint problem is to find the gradient of the objective function which is orthogonal to the gradient of the constraint that is the governing equation.

The starting point is to consider a perturbation to the physical variables and the design variables, $\delta\mathbf{c}$ and $\delta\boldsymbol{\theta}$. We then require orthogonality which corresponds to having the perturbation satisfy the governing equation ($0 = \mathbf{G} = \underline{\underline{\mathbf{A}}}\mathbf{c} - \mathbf{b}$), i.e.

$$\begin{aligned} \mathbf{0} &= \left(\underline{\underline{\mathbf{A}}} + \frac{\partial \underline{\underline{\mathbf{A}}}}{\partial \boldsymbol{\theta}}\delta\boldsymbol{\theta}\right)(\mathbf{c} + \delta\mathbf{c}) - \left(\mathbf{b} + \frac{\partial \mathbf{b}}{\partial \boldsymbol{\theta}}\delta\boldsymbol{\theta}\right) \\ &\approx \left(\frac{\partial \underline{\underline{\mathbf{A}}}}{\partial \boldsymbol{\theta}}\mathbf{c} - \frac{\partial \mathbf{b}}{\partial \boldsymbol{\theta}}\right)\delta\boldsymbol{\theta} + \mathbf{A}\delta\mathbf{c} \\ \Leftrightarrow \underline{\mathbf{0}} &= \frac{\partial \underline{\underline{\mathbf{A}}}}{\partial \boldsymbol{\theta}}\mathbf{c} - \frac{\partial \mathbf{b}}{\partial \boldsymbol{\theta}} + \mathbf{A}\frac{\partial \mathbf{c}}{\partial \boldsymbol{\theta}}, \end{aligned} \tag{3.2}$$

where we have neglected the second order term and exploited that the zeroth order term vanishes to write the second right-hand side. The last manipulation is just division by the design variable perturbation. The chain rule is then applied on the objective function and a special zero is added in the form of equation (3.2) multiplied with a set of *Lagrange multipliers* $\boldsymbol{\Lambda}$ to form what is called a Lagrange function derivative.

$$\begin{aligned} \frac{d\phi}{d\boldsymbol{\theta}} &= \frac{\partial \phi}{\partial \mathbf{c}}\frac{\partial \mathbf{c}}{\partial \boldsymbol{\theta}} + \frac{\partial \phi}{\partial \boldsymbol{\theta}} + \boldsymbol{\Lambda} \cdot \left(\frac{\partial \underline{\underline{\mathbf{A}}}}{\partial \boldsymbol{\theta}}\mathbf{c} - \frac{\partial \mathbf{b}}{\partial \boldsymbol{\theta}} + \underline{\underline{\mathbf{A}}}\frac{\partial \mathbf{c}}{\partial \boldsymbol{\theta}}\right) \\ &= \left[\frac{\partial \phi}{\partial \mathbf{c}} + \boldsymbol{\Lambda} \cdot \underline{\underline{\mathbf{A}}}\right]\frac{\partial c}{\partial \boldsymbol{\theta}} + \boldsymbol{\Lambda} \cdot \left(\frac{\partial \underline{\underline{\mathbf{A}}}}{\partial \boldsymbol{\theta}}\mathbf{c} - \frac{\partial \mathbf{b}}{\partial \boldsymbol{\theta}}\right) + \frac{\partial \phi}{\partial \boldsymbol{\theta}} \end{aligned} \tag{3.3}$$

The idea is to solve the linear equation system in square parentheses such that it disappears and the computation of the derivative of the physical variables with respect to the design variables can be avoided, but still taken into account. The problem in square parentheses is called the *dual* or *adjoint* problem, while the governing equation is sometimes referred to as the *primal problem*. The adjoint problem is linear and thus much cheaper to solve, if the governing equation is nonlinear. The special case of $\partial_{\mathbf{c}}\phi = -\mathbf{b}$ is called a self-adjoint problem, since this makes the adjoint problem identical to the governing equation and allows for the physical variables to be used as Lagrange multipliers. The analysis in the above is called a discrete adjoint, but it is also possible to derive a governing equation for the adjoint variables starting from the governing equations in what is called a continuous adjoint technique. This can be advantageous for a high-level formulation with the main disadvantage being, that the accuracy of the sensitivity is limited by the overall numerical convergence. In any case this gradient together with that of any relevant constraints can then be used as input for an optimizer (see figure 3.1)such as the method of moving asymptotes [28], SNOPT [29] or IPOPT [30]. We have chosen to use MMA with the nested formulation, which is probably the most popular combination. The SAND formulation can have superior convergence properties due to fact that higher order derivatives can be utilized [31], but this is of little consequence since MMA optimizations often stall very close to the optimum.

All users of topology optimization are faced with a kind of multi objective optimization problem in the sense, that one has to choose a set of parameters that gives a good balance between computational cost, how discrete the design is, how smooth the objective function is and how accurately the physics is described, see figure 3.2. In many cases this balance relates

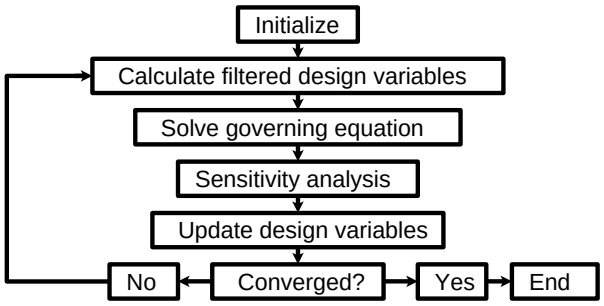

Figure 3.1: The flow chart of a typical optimization is shown with the optimizer responsible for updating the design variables based on the sensitivity analysis. This is based on the solution to the governing equation, which again is based on the design variables, completing the loop.

to length scales of different magnitude for the physics, the design and the discretization – with the easier problems characterized by similar length scales.

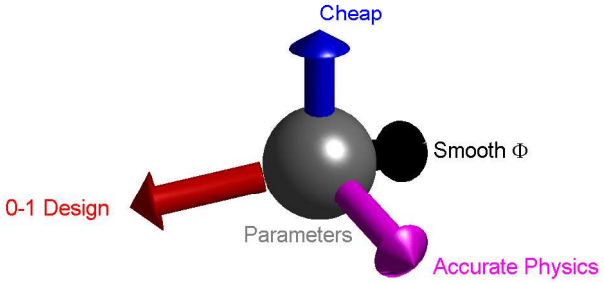

Figure 3.2: The choice of parameters in topology optimization is a balance between several conflicting objectives.

This work, and papers [P2] and [P4] in particular, is based on a high level implementation of the topology optimization method [32]. This implementation is specific to steady problems although topology optimization can be extended to transient problems. Note however that topology optimization of unsteady flows requires the definition of an observation domain in time, and that this domain has to be very large in order for the design not to depend on it – often so large that it becomes impractical for optimization.

3.1.1 Example: Structural Optimization with the PDE Filter

Within topology optimization for structural problems the use of a filter is almost always required. This is because the problem is ill-posed in the sense that the minimum length scale of the optimal structure does not have a lower bound. Many remedies have been successfully tested, but one of the most popular solutions is to compute a filtered design variable field, $\tilde{\theta}$, which has a minimum length scale, $L_{\min}$. Some filters define the filtered design variables explicitly using the discretized design variables, but it currently seems like the PDE filter [33] is gaining popularity. This filter is implicit, which allows it to be added as part of the governing equations, before they are discretized, making implementation in commercial tools much easier in a high-level formulation.

A typical problem of minimum compliance (without volume forces) can thus be stated as

$$\min_{\theta} \left(\int_{\partial\Omega_{\text{load}}} \underline{\underline{\boldsymbol{\tau}}}_{\text{load}} \cdot \hat{\mathbf{n}} \cdot \mathbf{v} d\Omega \right) \quad \text{subject to} \tag{3.4a}$$

$$\mathbf{0} = \boldsymbol{\nabla} \cdot \underline{\underline{\boldsymbol{\tau}}} = \boldsymbol{\nabla} \cdot \left[\frac{E\nu}{2(1+\nu)(1-2\nu)} \text{Tr}(\underline{\underline{\boldsymbol{\gamma}}}) \underline{\underline{\mathbf{I}}} + \frac{E}{2(1+\nu)} \underline{\underline{\boldsymbol{\gamma}}} \right] \quad \text{and} \tag{3.4b}$$

$$\mathbf{0} = L_{\min}^2 \boldsymbol{\nabla}^2 \tilde{\theta} + \theta - \tilde{\theta} \quad \text{in } \Omega \quad \text{where} \tag{3.4c}$$

$\underline{\underline{\boldsymbol{\gamma}}} = \boldsymbol{\nabla}\mathbf{v} + (\boldsymbol{\nabla}\mathbf{v})^T$ and $E = E_{\min} + (E_{\max} - E_{\min})\tilde{\theta}^P$. With the BCs

$$\underline{\underline{\boldsymbol{\tau}}} = \underline{\underline{\boldsymbol{\tau}}}_{\text{load}} \quad \text{at } \partial\Omega_{\text{load}} \quad \text{and} \quad \mathbf{v} = \mathbf{0} \quad \text{at } \partial\Omega_{\text{support}}, \quad \text{and the constraints} \tag{3.4d}$$

$$\int \theta d\Omega \leq V_{\text{frac}} \int d\Omega \quad \text{and} \tag{3.4e}$$

$$0 \leq \theta \leq 1. \tag{3.4f}$$

Here $\mathbf{v}$ is the displacement, $\underline{\underline{\boldsymbol{\gamma}}}$ is the deformation tensor, $\underline{\underline{\boldsymbol{\tau}}}$ is the stress, E is the Young's modulus, ν is the Poisson ratio and V_{frac} is the allowed volume fraction. Note that the absence of volume forces makes it possible to rescale the displacement field, such that the Youngs modulus disappears, i.e. the ratio $E_{\max}/E_{\min}$ matters, but the absolute values do not. We choose an infinite ratio. We solve the cantilever problem illustrated in figure 3.3 with L_y as characteristic length scale, $L_x = 2L_y$, $L_1 = L_y/5$, $V_{\text{frac}} = 0.5$ and $\underline{\underline{\boldsymbol{\tau}}}_{\text{load}} = -\hat{\mathbf{x}} \otimes \hat{\mathbf{y}}$. The exponent P affects the stiffness of intermediate material, and it plays a central role for convergence of the optimization, because a value of 1 gives a convex problem with a smeared out optimal design, while $P = 3$ gives a highly non-convex problem with a black and white optimal design. The optimization is thus started with $P = 1$, and this optimized design is used as initial condition for an optimization with $P = 2$, before finally optimizing for $P = 3$. Such a continuation approach is a typical strategy for finding a good global optimum to a problem with many local optima. Due to the fact that structural problems with compliance minimization (such as this) have been shown to be convex for $P = 1$, they are considered to be "solved" – for this reason some journals have in fact gone as far as to ban papers on compliance minimization.

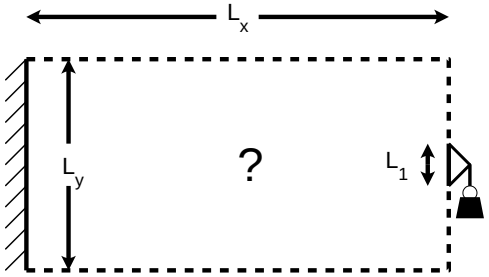

Figure 3.3: The setup for structural topology optimization of a cantilever is illustrated with support to the left and load on the right, see equation (3.4)

As shown in figure 3.4 we vary the characteristic size of the element, h_{mesh} and consider the case of $L_{\min} = h_{\text{mesh}}/2$ (a) as well as $L_{\min} = 0.025$ (b). Convergence with respect to the mesh size is only achieved in the latter case, while increasingly finer details are resolved for the first.

3.2 Anisotropic Flow Resistance

One of the fundamental advantages of models with differential constitutive equations compared to generalized Newtonian models is the ability of the fluid to have a memory of past deformations.

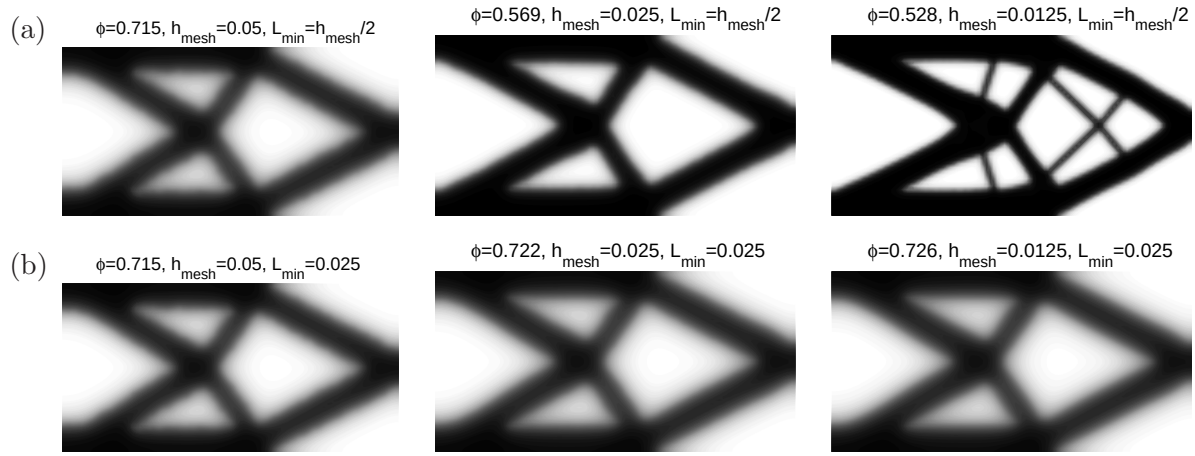

Figure 3.4: The filtered design variable $\tilde{\theta}$ is plotted for different solutions to the cantilever problem stated in equation (3.4) and illustrated in figure 3.3. The characteristic mesh size h_{mesh} is varied, while considering $L_{\min} = h_{\text{mesh}}/2$ (a) as well as $L_{\min} = 0.025$ (b). The objective and design only converges in the latter case.

This enables prediction of anisotropic flow resistance – among many other flow phenomena observed in experiments. This topic has been studied extensively for inertial effects, but little work had been done from a theoretical point of view for viscoelastic effects. It is one of the less difficult problems, because an arbitrary design ought to give rise to some kind of anisotropic flow resistance, even if the Weissenberg number is close to zero. This is in contrast to the problem of bistability, which cannot be studied below a certain minimum Weissenberg number.

This topic of no-moving-parts (NMP) valves is often mentioned in relation to micro pumps, and particularly so for the viscoelastic case, because viscoelastic effects dominate at small length scales (see equation (1.14)). Little is however said about how one should design a micropump using these valves. Therefore we will now use the concept of equivalent circuit theory introduced in section 1.2.3 to determine the optimal design of such a micro pump.

Although a real pump might give rise to a sinusoidal input, we will assume an input that shifts abruptly between two flow directions and neglect all transient effects, just for the sake of simplicity. This means that we can calculate the steady state flow in both configurations and add them together to arrive at a net flow. If back flow is not acceptable, one will have to use a bridge configuration as illustrated in figure 3.5 (a). If the load cannot be placed in the center, one flow has to cross over another, which can complicate fabrication, and therefore we have also analyzed the case of a simple series configuration as shown in figure 3.5 (b).

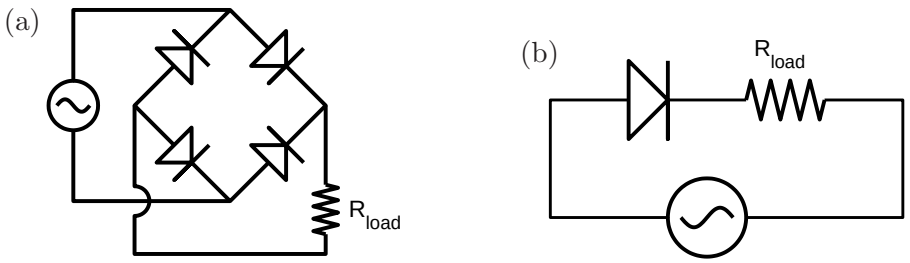

Figure 3.5: The bridge (a) and series (b) equivalent circuits for achieving a net flow using a fluidic rectifier and an oscillating input.

In both cases we assume that the rectifier has a hydraulic resistance which depends on the

flow direction. We will refer to the ratio between these resistances as the rectifier efficiency,

$$\epsilon = \frac{R_b}{R_f},$$

where R_b is the backward flow resistance, which is larger than the forward flow resistance, R_f. Furthermore the optimal design of the pump depends on R_{load}, the hydraulic resistance of the device that it is intended to be used with, and therefore the R_f/R_{load} ratio often appears.

3.2.1 Series Configuration

The series configuration shown in figure 3.5 (b) is simple to analyze in the sense that it is straight forward to write up the flow rate for both configurations, $\dot{V}_f$ and $\dot{V}_b$, such that the average flow rate can be computed

$$\begin{aligned} \dot{V}_{\text{avg}} &= \frac{\dot{V}_f - \dot{V}_b}{2} = \frac{\Delta p_{\text{drv}}}{2}\left(\frac{1}{R_{\text{load}}+R_f} - \frac{1}{R_{\text{load}}+R_b}\right) \\ \Leftrightarrow \frac{2\dot{V}_{\text{avg}}R_{\text{load}}}{\Delta p_{\text{drv}}} &= \frac{1}{1+\frac{R_f}{R_{\text{load}}}} - \frac{1}{1+\epsilon\frac{R_f}{R_{\text{load}}}}. \end{aligned} \tag{3.5}$$

This expression can be interpreted as the average pressure over the load normalized with the total driving pressure. It has a maximum at $R_{\text{load}}/R_f = \sqrt{\epsilon}$. This analysis assumes, that it is the driving pressure that is independent of the flow direction. Alternatively one can consider the case of a constant power, P, and get

$$\frac{\dot{V}_{\text{avg}}^2 R_{\text{load}}}{P_{\text{drv}}} = \frac{1}{4}\left(\frac{1}{\sqrt{1+\frac{R_f}{R_{\text{load}}}}} - \frac{1}{\sqrt{1+\epsilon\frac{R_f}{R_{\text{load}}}}}\right). \tag{3.6}$$

This can be interpreted as an average power consumption in the load normalized with the total power consumption. This also has a maximum in R_{load}/R_f, but it does not lend itself to be expressed in terms of simple analytical functions. We have however plotted the optimum value as a function of the rectifier efficiency in figure 3.6 (a) together with the expression for the bridge configuration given by equation (3.8).

3.2.2 Bridge Configuration

The bridge configuration is symmetric in terms of the flow configuration, so we only have to analyze one flow direction. We denote the flow rate through the resistors to the right in figure 3.5 (a) by $\dot{V}_1$ (upper) and $\dot{V}_2$ (lower) with the downward flow positive in the case, where the pump is moving the fluid up. This allows us to arrive at a set of equations using Kirchhoff's circuit laws

$$\left.\begin{aligned} R_f\dot{V}_1 + R_b(\dot{V}_1 - \dot{V}_{\text{drv}}) + R_{\text{load}}(\dot{V}_1 - \dot{V}_2) &= 0 \\ R_b\dot{V}_2 + R_f(\dot{V}_2 - \dot{V}_{\text{drv}}) + R_{\text{load}}(\dot{V}_2 - \dot{V}_1) &= 0 \\ R_b(\dot{V}_1 - \dot{V}_{\text{drv}}) + R_f(\dot{V}_2 - \dot{V}_{\text{drv}}) &= -\Delta p_{\text{drv}} \end{aligned}\right\}$$

$$\Rightarrow \quad \begin{aligned} \dot{V}_1 &= \Delta p_{\text{drv}}\frac{R_b+R_{\text{load}}}{2R_bR_f+R_bR_{\text{load}}+R_fR_{\text{load}}} \\ \dot{V}_2 &= \Delta p_{\text{drv}}\frac{R_f+R_{\text{load}}}{2R_bR_f+R_bR_{\text{load}}+R_fR_{\text{load}}} \\ \dot{V}_{\text{drv}} &= \Delta p_{\text{drv}}\frac{R_f+R_b+2R_{\text{load}}}{2R_bR_f+R_bR_{\text{load}}+R_fR_{\text{load}}} \end{aligned},$$

where $\dot{V}_{\text{drv}}$ is the flow rate through the pump and Δp_{drv} is the driving pressure. The flow rate through the load is equal to $\dot{V}_1 - \dot{V}_2$, and it is thus straight forward to write up the total resistance R_{drv}, load pressure Δp_{load} and load flow rate

$$\begin{aligned} R_{\text{drv}} &= \frac{\Delta p_{\text{drv}}}{\dot{V}_{\text{drv}}} = \frac{2R_bR_f + R_bR_{\text{load}} + R_fR_{\text{load}}}{R_f + R_b + 2R_{\text{load}}} \\ \frac{\dot{V}_{\text{load}}}{\dot{V}_{\text{drv}}} &= \frac{\dot{V}_1 - \dot{V}_2}{\Delta p_{\text{drv}}/R_{\text{drv}}} = \frac{\epsilon - 1}{\epsilon + 1 + 2R_{\text{load}}/R_f} \\ \frac{\Delta p_{\text{load}}}{\Delta p_{\text{drv}}} &= \frac{(\dot{V}_1 - \dot{V}_2)R_{\text{load}}}{\Delta p_{\text{drv}}} = \frac{\epsilon - 1}{2\epsilon R_f/R_{\text{load}} + \epsilon + 1} \end{aligned} \tag{3.7}$$

The dissipated power in the load, $I_{\text{load}}\Delta p_{\text{load}}$ has a maximum for

$$\boxed{R_{\text{load}}/R_f = \sqrt{\epsilon}}, \tag{3.8}$$

which corresponds to an energy efficiency of

$$\left.\frac{\dot{V}_{\text{load}}\Delta p_{\text{load}}}{\dot{V}_{\text{drv}}\Delta p_{\text{drv}}}\right|_{\frac{R_{\text{load}}}{R_f}=\sqrt{\epsilon}} = \frac{(\sqrt{\epsilon}-1)^2}{(\sqrt{\epsilon}+1)^2} \tag{3.9}$$

The consequence of this is, that going from a diodicity of 1.2 to 3 (typical of inertial and viscoelastic valves, respectively) represents an improvement of a factor of 35 in terms of energy efficiency, even though we only reach 7%. A diodicity of $\epsilon \approx 34$ is required to achieve an energy efficiency of 50 %.

Finally, in figure 3.6 (b), we have compared the optimal power efficiencies of the two configurations as given by equations (3.9) and (3.6). The comparison indicates that the series configuration is favored for rectifier efficiencies below 2.2. One should however keep in mind that the efficiency of practical rectifiers is highly dependent on the flow rate, which makes the quantitative results of this analysis nothing more than a rule of thumb.

3.2.3 Conclusion

If one cannot accept back flow, a pumping setup based on a bridge configuration should be adopted and the same is the case, if the applied rectifiers have good efficiencies. The rectifiers should be scaled or repeated such that the hydraulic resistance of the load relative to the total hydraulic resistance of a rectifying element in the forward configuration follows the curves of figure 3.6 (a).

3.3 [P2]: Topology Optimization of Viscoelastic Rectifiers

The following work was accepted for publication in the journal of Applied Physics Letters.

3.3.1 Abstract

An approach for the design of microfluidic viscoelastic rectifiers is presented based on a combination of a viscoelastic model and the method of topology optimization. This presumption free approach yields a material layout topologically different from experimentally realized rectifiers, and simulations indicate superior performance for the optimized design in the regime of moderate elasticity.

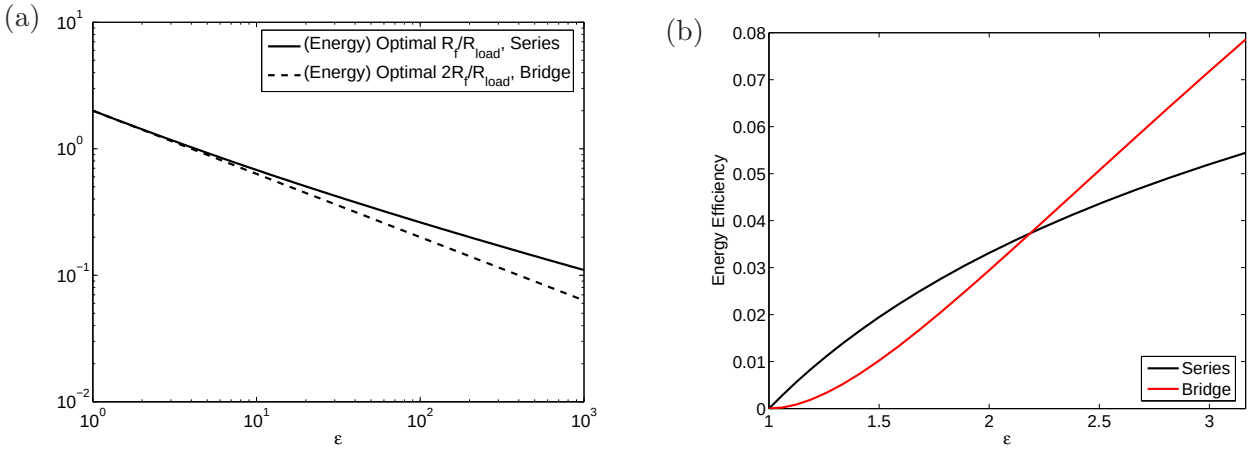

Figure 3.6: The most energy efficient R_{load}/R_f ratio is plotted as a function of the rectifier efficiency for the series configuration (a). The analytical result for the bridge configuration is included for comparison, but it is multiplied by two to illustrate the fact, that the curves coincide for small rectifier efficiencies. The actual value at the maximum is given by the right-hand side of equation (3.6), and this is plotted in (b) together with the equivalent result for the bridge configuration given by equation (3.9). The curves insect for $\epsilon \approx 2.2$, which indicates that the bridge configuration is more efficient beyond this point.

3.3.2 Article Text

Micropumps are needed for medical delivery as well as lab-on-a-chip systems, and they can be constructed using a variety of actuation principles[34]. Interest has gathered around the possibility of combining an oscillating diaphragm with no-moving-parts valves/rectifiers, which rely on the inertial properties of the fluid for their working mechanism[35]. In example the method of topology optimization has been applied to reproduce the Tesla valve as the optimal design for these devices[36]. Inertial effects, and thus also the performance of inertial rectifiers, however decreases as devices are scaled down. Viscoelastic effects on the other hand do not vanish at the micro scale, and therefore rectifiers have been suggested[37, 38] on this basis.

Topology optimization with a memory free non-Newtonian fluid has been demonstrated[39], but the working mechanism of viscoelastic rectifiers is related solely to the memory of the fluid due to past deformations. Topology optimization considering fluid memory has not previously been demonstrated, and this is probably due to the fact that merely modeling such a fluid in complex geometries has been a long standing challenge for the scientific community. We find that it is possible to combine recent model developments[16] with a high level implementation of topology optimization[32] to determine the optimal material layout, that maximizes the flow rate ratio in a rectifier device. The optimization allows for porous material, so to confirm that the design does not rely on this, we perform simulations without it, and such a quantitative investigation of viscoelastic rectifiers outside an experimental setting has not previously been demonstrated.

The fluid memory is described with a differential constitutive model, where the spatial configuration of e.g. the molecules, or whatever gives rise to the viscoelastic properties, is taken into account. A popular approach is to study a solution of spring connected point mass pairs (dumbbells) in a Newtonian solvent considering only orientation and elongation of fluid elements. In such models the conformation tensor $\underline{\underline{\mathbf{A}}}$, is used to describe configurations, and it is related to the dumbbell end-to-end vector $\mathbf{a}$, such that $\text{Trace}(\underline{\underline{\mathbf{A}}}) = \langle \mathbf{a}^2 \rangle / a_{\text{eq}}^2$, where $\langle \cdots \rangle$ is a statistical average, and a_{eq} is the equilibrium length of the end-to-end vector. The finite extensibility model by Chilcott and Rallison[9] features both a finite maximum dumbbell extensibility a_{max}

as well as a constant shear viscosity, like Boger fluids[40].

$$-\frac{k(\underline{\underline{\mathbf{A}}})}{\lambda}\left(\underline{\underline{\mathbf{A}}}-\underline{\underline{\mathbf{I}}}\right) = \frac{D\underline{\underline{\mathbf{A}}}}{Dt}-\left[\underline{\underline{\mathbf{A}}}\cdot\boldsymbol{\nabla}\,\mathbf{v}+(\boldsymbol{\nabla}\,\mathbf{v})^T\cdot\underline{\underline{\mathbf{A}}}\right] \tag{3.10}$$

$$k(\underline{\underline{\mathbf{A}}}) = \frac{1}{1-\mathrm{Trace}(\underline{\underline{\mathbf{A}}})/\mathrm{a}_{\max}^2} \tag{3.11}$$

$$\underline{\underline{\boldsymbol{\tau}}}_e = \frac{\eta_p}{\lambda}k(\underline{\underline{\mathbf{A}}})\left(\underline{\underline{\mathbf{A}}}-\underline{\underline{\mathbf{I}}}\right), \tag{3.12}$$

where $\underline{\underline{\mathbf{I}}}$ is the identity matrix, $\mathbf{v}$ is the velocity, λ is the dumbbell relaxation time, D/Dt is the material derivative, η_p is a dumbbell viscosity and $k(\underline{\underline{\mathbf{A}}})$ can be thought of as a nonlinear spring constant modification. $\underline{\underline{\boldsymbol{\tau}}}_e$ is the dumbbell stress tensor, which is put into the Stokes equation, when assuming a creeping isothermal and incompressible viscoelastic fluid. Adding the usual continuity equation for mass conservation yields

$$\mathbf{0} = \boldsymbol{\nabla}\cdot\left(-p\underline{\underline{\mathbf{I}}}+\eta_s\underline{\underline{\dot{\boldsymbol{\gamma}}}}+\underline{\underline{\boldsymbol{\tau}}}_e\right) \tag{3.13}$$

$$0 = \boldsymbol{\nabla}\cdot\mathbf{v}, \tag{3.14}$$

where p is the pressure, η_s is the solvent viscosity and $\underline{\underline{\dot{\boldsymbol{\gamma}}}} = \boldsymbol{\nabla}\,\mathbf{v}+(\boldsymbol{\nabla}\,\mathbf{v})^T$ is the rate of deformation tensor. It has been shown that the solution of Eqs. (3.10)-(3.14) with the finite element method is troubled by the existence of discontinuous velocity gradients $\boldsymbol{\nabla}\,\mathbf{v}$, at element borders[18]. The remedy is to construct a continuous approximation $\underline{\underline{\mathbf{G}}}$, for use on the right hand side of equation (3.10) and to add $\eta_p(\underline{\underline{\dot{\boldsymbol{\gamma}}}}-\underline{\underline{\mathbf{G}}}-\underline{\underline{\mathbf{G}}}^T)$ as a zero on the right hand side of the Stokes equation (1.2). A significant development occurred with the introduction of the log-conformation method[16] involving a substitution $\underline{\underline{\mathbf{A}}} = e^{\underline{\underline{\mathbf{s}}}}$, such that equation (3.10) is transformed to take the form

$$\frac{D\underline{\underline{\mathbf{s}}}}{Dt} = \underline{\underline{\mathbf{R}}}(\underline{\underline{\mathbf{s}}},\underline{\underline{\mathbf{G}}}),$$

where the computation of the reaction term $\underline{\underline{\mathbf{R}}}$ as well as the conformation tensor $e^{\underline{\underline{\mathbf{s}}}}$, involves calculation of eigenvectors and eigenvalues of $\underline{\underline{\mathbf{s}}}$[16, 41]. This change of variables guarantees the positive definiteness of the conformation tensor, making it a much more robust formulation. It however also complicates the equations and associated linearizations significantly, and therefore the optimization in this work relies heavily on a commercial high level finite element package[1] and related implementation of topology optimization[32].

We implement topology optimization by adding the usual Darcy damping term[26] $-\alpha(\theta)\mathbf{v}$, to the right hand side of the Stokes equation (3.13) . The idea is that wherever the design variable θ, is equal to unity, the damping term vanishes such that the governing equation for a fluid domain is recovered; conversely where the design variable is equal to zero, it results in very large damping terms $\alpha_{\max}$, such that the velocity becomes marginal, and the no slip boundary condition is enforced in an approximative way. A continuous optimization problem can then be formulated by interpolating the damping term in the design variable, but the convergence properties of the optimization is sensitive to the choice of interpolation. In this work a PDE filter[33] is applied to the design variable producing a filtered design variable $\tilde{\theta}$, with a minimum length scale $L_{\min}$, Eq. (3.15). Then a projection function[42], Eq. (3.16), defines the projected

[1] COMSOL 3.5a Multiphysics Reference Guide (2008).

design variable $\bar{\theta}$, which is used in the usual convex relation[26], Eq. (3.17).

$$\tilde{\theta} = \theta + L_{\min}^2 \boldsymbol{\nabla}^2 \tilde{\theta} \tag{3.15}$$

$$\bar{\theta} = \tfrac{1}{2} + \frac{\tanh(\xi(\tilde{\theta} - \tfrac{1}{2}))}{2\tanh(\xi/2)} \tag{3.16}$$

$$\alpha = \alpha_{\max} \frac{q(1-\bar{\theta})}{\bar{\theta} + q} \tag{3.17}$$

Here ξ defines the steepness of the projection function, while the convexity of the damping term in the projected design variable is determined by q.

Introducing a characteristic length scale L, pressure Δp^* and damping $\alpha_{\max}$ allows for the governing equations to be written in dimensionless form[2] such that the following dimensionless parameters arise

$$\mathrm{Da} = \frac{\eta_s + \eta_p}{L^2 \alpha_{\max}}, \quad \beta = \frac{\eta_s}{\eta_s + \eta_p}, \quad \text{and} \quad \mathrm{We} = \lambda \frac{\Delta p^*}{\eta_s + \eta_p}.$$

The Darcy number Da, describes the magnitude of the viscous term relative to the damping term in solid regions. Hence, excessively large Da will give a bad approximation of the no slip boundary condition, while convergence problems will arise for the optimization with too small Da. β expresses the proportion of viscous effects due to the solvent, while the Weissenberg number We, indicates the relative strength of elastic to viscous effects. Experimental rectifiers work most efficiently in the regime of high elasticity/We, where a transition to unsteady flow occurs, whereas we focus on optimization of steady solutions in the regime of moderate elasticity and correspondingly smaller driving pressures and/or relaxation times. Note that the Weissenberg number and thus also the device performance is independent of the characteristic length scale, provided the driving pressure is fixed, and inertia can be neglected.

We use a standard approach[41] for both the stabilization of the convective equation and for the representation of the various physical variables. The filtered design variable is represented by second order Lagrange elements, while the design variable itself is considered constant in all elements. Furthermore an isotropic triangular mesh is used to avoid favored design directions.

We use a fully implicit scheme to evolve in time for 20 dumbbell relaxation times starting from a viscoelastic fluid at rest, and then proceed by initializing a non-linear solver with the final transient solution[3]. Optimization iterations without steady solutions can occur, in which case the last transient solution is used for the sensitivity analysis. Although this approach is inconsistent, it does not become an issue for the optimization, since unsteady flows is a rare occurrence at the Weissenberg numbers considered. Our optimization setup is periodic and pressure driven as sketched in Fig. 3.7. The objective function ϕ, to be minimized is the flow rate ratio

$$\phi = \frac{\dot{V}_{\leftarrow}}{\dot{V}_{\rightarrow}} = \frac{\int -\mathbf{v}_{\leftarrow} \cdot \hat{\mathbf{x}} d\mathbf{r}}{\int \mathbf{v}_{\rightarrow} \cdot \hat{\mathbf{x}} d\mathbf{r}},$$

where the arrows indicate the flow configuration. We compute the objective function gradient $\partial\phi/\partial\theta$, with an adjoint method and combine it with the method of moving asymptotes[28] for updating the design variables.

In terms of model parameters we choose $\beta = 0.59$, as it is representative of Boger fluids and used widely in benchmarks of numerical algorithms for this reason. To avoid early transition to

[2] Additional information in supplementary material.

[3] The implementation uses default parameters[13], and it has been verified against a reference[16] in a benchmark geometry[17].

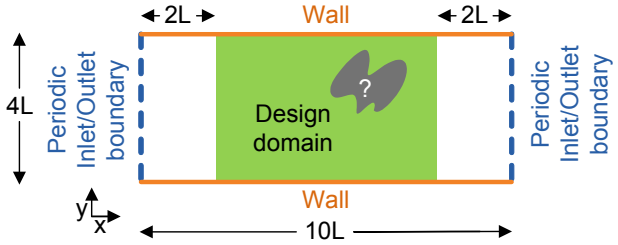

Figure 3.7: Optimization setup with periodic velocity vector and conformation tensor at the inlet/outlet boundaries, where the pressure is fixed at either 0 or Δp depending on the flow configuration($\rightarrow$ or $\leftarrow$). There is no tangential stress at the inlet/outlet boundaries and only pressure contributes to the normal stress. The no slip boundary condition is imposed on the top and bottom boundaries, and the design variable is defined in the central rectangle only.

unsteady flows, $a^2_{\max} = 100$ can be used, and with this we are able to perform optimizations at $\mathrm{We} = 5$ without serious issues with unsteady solutions. The driving pressure is set at $7.17\Delta p^*$ to give a unity average velocity for the initial empty design and thus also an effective We number closer to the imposed. Finally we find that the optimization performs well with a characteristic mesh size $h = L/10$, $L_{\min} = h$, $\mathrm{Da} = 10^{-5}$, $q = 4 \cdot 10^{-6}$ and $\xi = 10$.

Optimizations with and without imposed symmetry both result in a contraction followed by an obstacle as shown[17] in Fig. 3.8(a-b). The working mechanism is best understood by considering Fig. 3.8(c-g) specific to the symmetric case, while adopting the dumbbell fluid picture and focusing on the strongly accelerating nature of the flow in the obstacle wake close to the rear stagnation point: The acceleration will cause the forward dumbbell mass to move faster than the rear mass, and in this way a wake of elongated dumbbells appears, Fig. 3.8(c-d). The dumbbells are particularly elongated in the reverse flow configuration due to the high flow velocity in the contraction, and the wake causes a damping that gives rise to a local velocity minimum in the contraction center, Fig. 3.8(e-g).

As indicated in Fig. 3.8, the effective size of the obstacle is smaller than a plot of the filtered design variable on a linear scale suggests. This is due to the relation between the filtered design variable and the damping term (Eq. (3.17)), and it means that the projected design variable should be thresholded around $6 \cdot 10^{-4}$ to produce a performing design without porous material. It however seems that it is the curvature in the left region of the obstacle that is essential, which allows for the use of a significantly larger airfoil like obstacle.

The results of symmetric simulations with a state-of-the-art hyperbolic design[38] and a design derived from topology optimization are shown[17] in Fig. 3.9 in the case of boundary conditions and model parameters identical to that of the topology optimization. Although unsteady flows are often encountered, the objective function shows clear convergence up to $\mathrm{We} = 5$ with respect to spatial discretization and simulation time (not shown). The simulations indicate that the contraction-obstacle-design not only has superior performance in the considered regimem but also that the rectification effect sets in strongly at small Weissenberg numbers.

In conclusion we have presented results for topology optimization of a viscoelastic rectifier and found a design that promises superior performance in the regime of moderate elasticity.

3.3.3 Supplementary Material

Besides FENE-CR model in dimensionless form corresponding to equations (1.12a) and (1.13), the article includes additional figures in the supplementary material. These relate to verification of the numerical implementation using the confined cylinder geometry described in section 2.1.6. Lastly, there are additional figures for the verification simulations [figure 3.9] as shown in figure

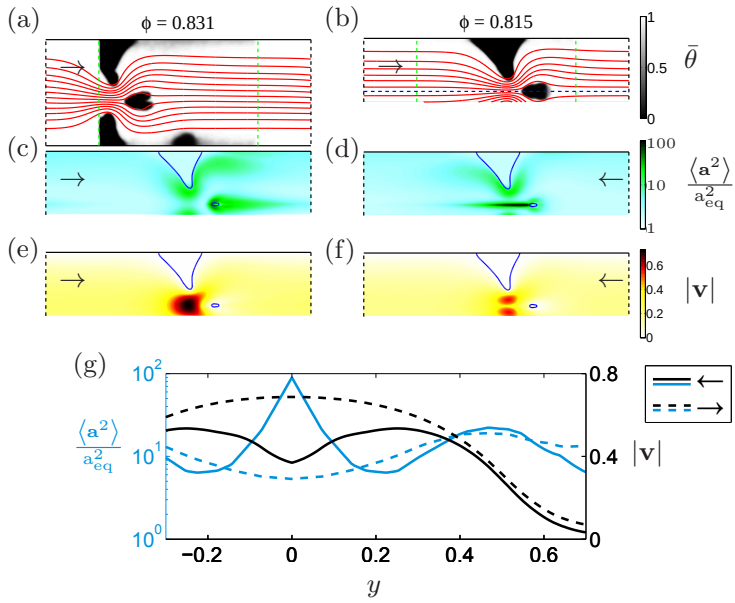

Figure 3.8: The filtered design variable is plotted together with streamlines for optimizations without (a) and with (b) symmetry. Both the dumbbell extension (c-d) and the velocity magnitude (e-f) are shown in the symmetric case for the two flow directions together with a $6 \cdot 10^{-4}$ contour of the projected design variable in blue. The working mechanism is illustrated by plotting the dumbbell extension and velocity magnitude through a cross section connecting the contractions (g).

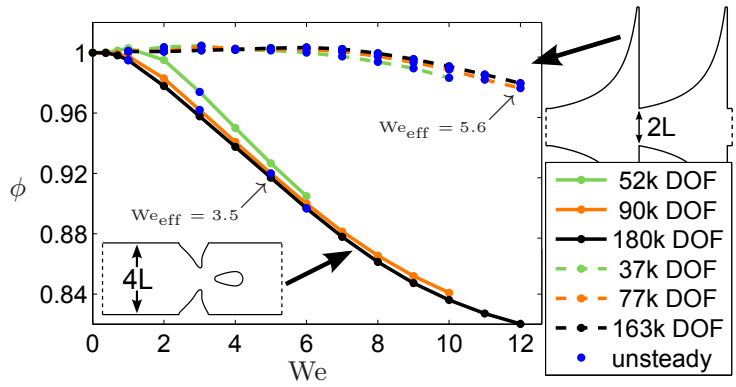

Figure 3.9: Two designs are characterized in terms of their flow rate ratio as a function of the Weissenberg number for different number of degrees of freedom (DOF). Effective Weissenberg numbers $\mathrm{We_{eff}}$, are calculated as $2\mathrm{We}\dot{V}_{\rightarrow}/L_{\mathrm{cont}}^2$, where L_{cont} is the width of the contractions.

3.10.

3.3.4 Aknowledgement

This work was presented at the 9th World Congress on Structural and Multidisciplinary Optimization (WCSMO9, Shizuoka, Japan) with support from the Otto Mønsted foundation.

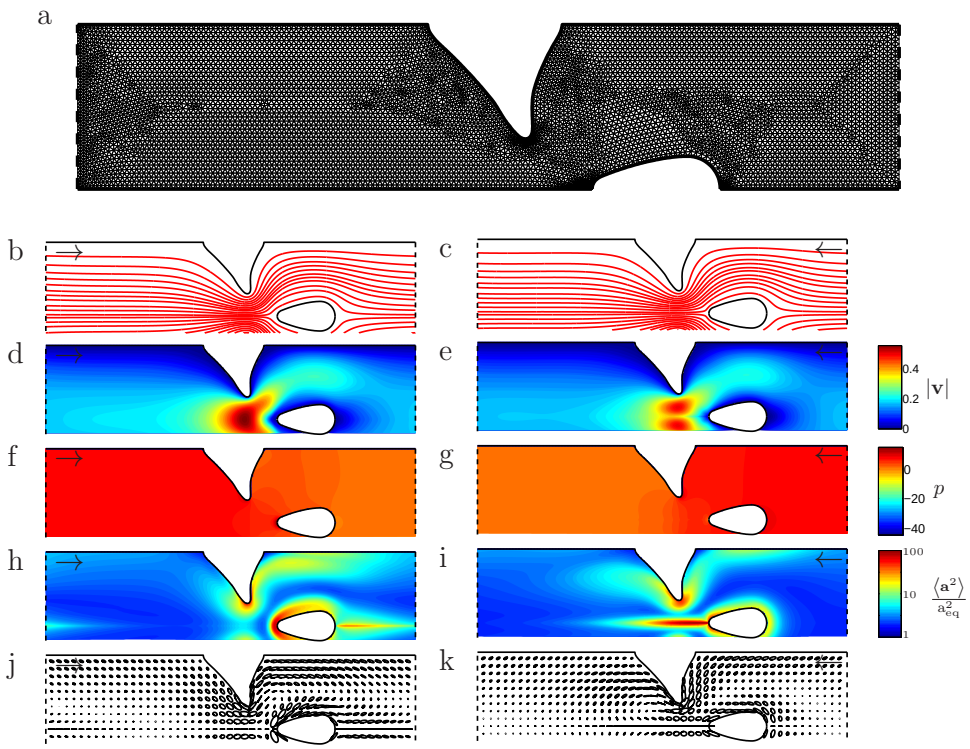

Figure 3.10: This figure shows the computational grid with 180k degress of freedom (a) used for the verification simulations (We=5) together with streamlines (b-c), velocity magnitude (d-e), pressure (f-g), conformation tensor trace (h-i) and finally the product of eigenvalues and eigenvectors for the log-conformation tensor as ellipses (j-k). Elements are concentrated around the obstacle forward and rear stagnation point in order to resolve the low pressure and high extensibility in this highly extensional region.

Chapter 4

Experimental Verification of Contraction-Obstacle Rectifier

Having found a radically new design for a viscoelastic rectifier, it seemed natural to perform an experimental investigation. It was thus fortunate that Professor Manuel Alves welcomed the idea and provided the equipment as well as guidance required for this experimental investigation. The experimental stay was thus carried out in the CEFT group at the Department of Chemical Engineering, Faculty of Engineering, University of Porto. The postdocs Francisco J. Galindo Rosales and Laura Campo Deaño helped with many of the practicalities, and as such they were crucial for this investigation. The stay itself was supported by the Otto Mønsted foundation.

The experiments where plagued with blocking, but we were able to find the point of maximum diodicity for the new design. The actual maximum diodicity was smaller than what had been reported for pure contraction designs, but the actual Weissenberg number where it occurred was slightly smaller. The following section is a copy of a paper accepted in the journal of Biomicrofluidics.

4.1 [P3]: Experimental Characterisation of a Novel Viscoelastic Rectifier Design

4.1.1 Abstract

A planar microfluidic system with contractions and obstacles is characterized in terms of anisotropic flow resistance due to viscoelastic effects. The working mechanism is illustrated using streak photography, while the diodicity performance is quantified by pressure drop measurements. The point of maximum performance is found to occur at relatively low elasticity levels, with diodicity around 3.5. Based on a previously published numerical work [Ejlebjerg et al. (2012) Appl. Phys. Lett. **100**, 234102], 2D simulations of the FENE-CR differential constitutive model are also presented, but limited reproducibility and uncertainties of the experimental data prevents a direct comparison at low elasticity, where the flow is essentially two-dimensional.

4.1.2 Introduction

Lab-on-a-chip systems can be applied for analysis and separation purposes[43, 44] with reduction in cost, analysis time and sample volumes as major advantages compared to conventional laboratory methods[45]. Micropumps can be used in lab-on-a-chip systems, but the lack of robust valves on the microscale is a critical limitation. In fact, the smallest experimentally realized pumps rely on passive valves, which are quite leaky in the sense that the resistance only

differs slightly between the two flow directions. This anisotropic flow resistance is due to inertial effects[35], but it is well-known that inertial effects decrease when devices are scaled down, making this mechanism a questionable candidate for a pump on the microscale. Many working fluids, however, contain large flexible molecules, e.g. biological fluids or polymers, and these can give rise to viscoelastic properties. Therefore, leaky valves/rectifiers relying on viscoelastic effects have been suggested[37, 38, 46], as this working mechanism not only survives, when the valve is scaled down, but also gives rise to significantly higher diodicity[47], and thus potentially larger flow rates. The working mechanism is related to elastic instabilities, which can also be used in the context of micromixing[48].

The effect of combining a contraction with an obstacle has been investigated for rectifiers of the inertial type[47], but experimental characterization of viscoelastic rectifiers have been limited to variations of the contraction shape only[37, 38, 46, 49]. Recent theoretical optimization and modelling suggests that a contraction-obstacle design could be advantageous for viscoelastic rectifiers in the regime of moderate elasticity[20], and this constitutes the motivation for the present work. In this work, we aim to compare simulations with experiments using only a differential pressure sensor[50] and a syringe pump, as opposed to determining the full stress field using a more complex birefringence set-up[5].

4.1.3 Experimental Setup

An overview of the main experimental equipment used is presented in Table 4.1, including the syringe pump for imposing flow rates and details on the set-up used for streak photography.

We employ standard soft lithography techniques for fabrication[51] of the polydimethylsiloxane (PDMS) microchannels illustrated in figure 4.1. The contraction and obstacle widths[1] are 39 μm, while the element length is 450 μm and the out-of-plane channel depth is 200 μm. To minimize inlet/outlet effects, the microchannels consist of 25 repeated elements with inlet/outlet as well as pressure ports at each side[50]. We also fabricated smaller microchannels, by a factor of two, but significant blockage problems made characterization of these channels impossible.

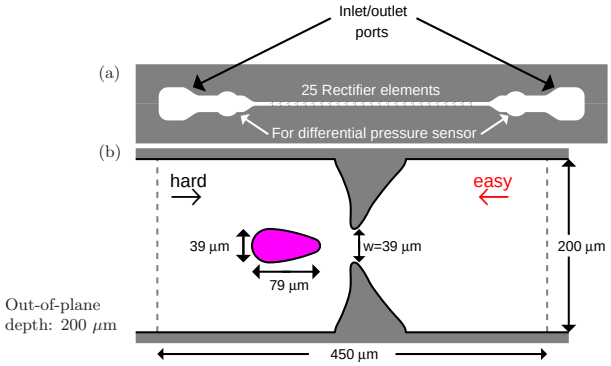

Figure 4.1: Microchannel overall view, including connections for the pressure sensor as well inlet/outlet ports (a). The dimensions of the contraction-obstacle geometry are shown in (b). The out-of-plane channel depth is 200 μm.

Robustness and resistance towards blocking are often highlighted features of passive over active valves, but channel blocking has actually been a significant difficulty for data reproducibility in the present work. If viscoelastic rectifiers are to be applied in an experimental micro pumping setup, it is therefore worth emphasizing the importance of clean and well mixed fluids as well as the use of fabrication techniques which do not introduce PDMS residue.

[1] An exact description of the geometry was included in the supplementary material for the article.

For the pressure drop measurements we use a 1 psi differential pressure sensor from Honeywell. The limited sensitivity of this pressure transducer requires a fluid with a minute polymer concentration to allow for characterization in the regime of low elasticity. Consequently we use an aqueous solution of 50 ppm polyacrylamide (PAA) with a molecular weight of 18×10^6 g/mol. To prevent shear thinning and blocking, we add 1 wt.% NaCl and 0.1 wt.% sodium dodecyl sulfate (SDS), respectively. Neglecting the effect of SDS, this fluid has a relaxation time of 4 ± 1 ms, and the shear viscosity varies by less than 2 % for 10^3-10^4 s^{-1}, shear rates as measured with a capillary break-up extensional rheometer (CaBER) and parallel plate shear rheometer, respectively[52].

The data of typical experiments are shown in figure 4.2. Based on observations through an optical microscope, we attribute the difference between experiments at identical flow conditions to partial channel blocking. The amplitude of the pressure drop oscillations increase with the flow rate, and the frequency is proportional to the flow rate. The proportionality factor corresponds to 16.6 μL per oscillation, which is in good agreement with 16.7 μL computed from a 4.61 mm inner syringe diameter and a 1 mm screw pitch, as used in the experimental set-up. We thus conclude that the syringe pump has an imperfection, such that each flow rate oscillation period corresponds to the time elapsed during one full revolution of the pump screw. The variation of oscillation amplitude for identical flow conditions probably arises because the imperfection is a non-linear function of the pump position (the syringe fluid volume). Alternatively the syringe pressure can play a role, as this does not reflect the differential pressure, if the outlet tube is partially blocked.

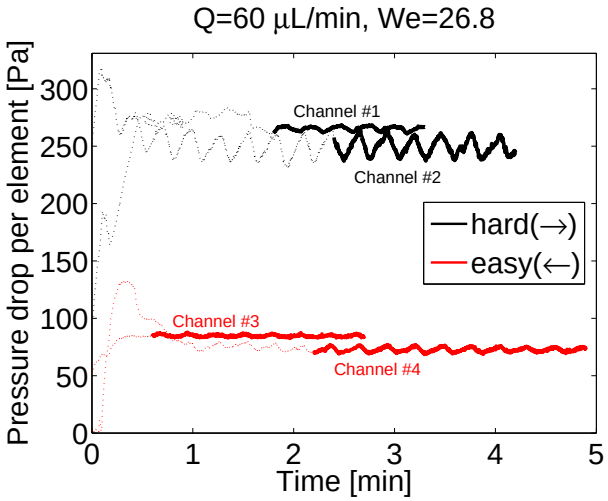

Figure 4.2: Measured pressure drop as a function of time for four experiments, two in each flow direction. The thick curves correspond to the data used to calculate averaged values. Oscillations in the sensor signal with a period much longer than fluid relaxation time occur, but the effect of blocking exceeds the error related to the averaging of these oscillations.

4.1.4 Numerical Simulations

We perform 2D simulations with the FENE-CR model given by

Table 4.1: List of equipment used excluding tubing and most equipment used for fabrication.

Manufactor	Product	Description
Cetoni	neMESYS	Syringe pump
Hamilton	1 mL	Syringe
National Instruments	6218-USB	Data Acquisition board
Honeywell	1 psi, 26PC series	Differential pressure sensor
Leica Microsystems	DMI 5000M	Inverted Microscope
Leica Microsystems	HCX APO L	Objective (10X/NA=0.25)
Leica Microsystems	DFC350 FX	Monochrome digital camera
Leica Microsystems	Excitation BP 530-545 nm	Filter cube
Molecular probes	Nile red, Invitrogen, Ex/Em: 520/580 nm	Fluorescent micro-particles
Sigma-Aldrich	Sodium dodecyl sulfate	Surfactant
	Precision tips	ID-OD: 0.41-0.71 mm (blue, for connection) ID-OD: 0.51-0.81 mm (purple, for punching holes)
Lascar Electronics	PSU 206 5-15V	DC power supply
Leica Microsystems	HBO 100	100 W Mercury lamp for streak photography

$$0 = \boldsymbol{\nabla}\cdot\left(-p\underline{\underline{\mathbf{I}}}+\eta_s\left[\boldsymbol{\nabla}\mathbf{v}+(\boldsymbol{\nabla}\mathbf{v})^T\right]+\underline{\underline{\boldsymbol{\tau_e}}}\right) \tag{4.1}$$

$$\overbrace{-12\frac{\eta_s+\eta_p}{h^2}\mathbf{v}}^{\mathbf{F}_{3D}} \tag{4.2}$$

$$\boldsymbol{\nabla}\cdot\mathbf{v} = 0$$

$$\underline{\underline{\boldsymbol{\tau_e}}} = \frac{\eta_p}{\lambda\left(1-\mathrm{Trace}(\underline{\underline{\mathbf{A}}})/a^2_{\max}\right)}\left(\underline{\underline{\mathbf{A}}}-\underline{\underline{\mathbf{I}}}\right) \tag{4.3}$$

$$-(\underline{\underline{\mathbf{A}}}-\underline{\underline{\mathbf{I}}}) = \lambda\left(\frac{D\underline{\underline{\mathbf{A}}}}{Dt}-\left[\underline{\underline{\mathbf{A}}}\cdot\boldsymbol{\nabla}\mathbf{v}+(\boldsymbol{\nabla}\mathbf{v})^T\cdot\underline{\underline{\mathbf{A}}}\right]\right), \tag{4.4}$$

where $\mathbf{v}$ is the velocity vector, p is the pressure, $\underline{\underline{\boldsymbol{\tau_e}}}$ is the polymer extra-stress tensor, $\underline{\underline{\mathbf{A}}}$ is the conformation tensor, h is the channel depth (200 μm), λ is relaxation time, $a_{\max}$ is the maximum to equilibrium polymer extensibility, while η_s and η_p are the solvent and polymer viscosities, respectively. The elastic component of the fluid is modelled as an ensemble of point mass pairs connected by a non-linear spring, "dumbbells". The dumbbell end-to-end vector, $\mathbf{a}$, is related to the conformation tensor, $\underline{\underline{\mathbf{A}}}$, such that

$$\underline{\underline{\mathbf{A}}} = \frac{\langle\mathbf{a}\otimes\mathbf{a}\rangle}{\mathrm{a}^2_{\mathrm{eq}}},$$

where $\langle ...\rangle$ is the statistical average and a_{eq} is the squared equilibrium dumbbell extension. Consequently the conformation tensor trace, $\mathrm{Tr}(\underline{\underline{\mathbf{A}}})$, equals the statistical average of the squared dumbbell extension, a^2, normalized with the squared equilibrium extension.

The numerical solution of equations (4.1)-(4.4) was described in a previous work[20], where a slightly different geometry was studied in the absence of the force $\mathbf{F}_{3D}$. The FENE-CR model has a constant shear viscosity, and this means that it is possible to use an extra damping term to account for the effect of the third dimension, also called the shallow channel approximation. The channel depth and width are equal, so it is a rather crude approximation, but it is an efficient way of introducing extra shear effects without performing a full three dimensional calculation.

The simulations were performed with 439k degrees of freedom, and they indicates a particular working mechanism in the regime of low to moderate elasticity as illustrated in figure 4.3: In the obstacle wake a birefringent strand of elongated polymer dumbbells appears [figure 4.3(b)], which is particularly elongated in the reverse flow configuration due both to the small curvature of the obstacle trailing edge and the accelerating nature of the flow due to the contraction. Figure 4.3(a) shows that the normal stresses generated this way give rise to a damping, which creates a local minimum in the flow velocity along the line connecting the contractions. This does not happen for the opposite flow direction [see figure 4.3(c-d)].

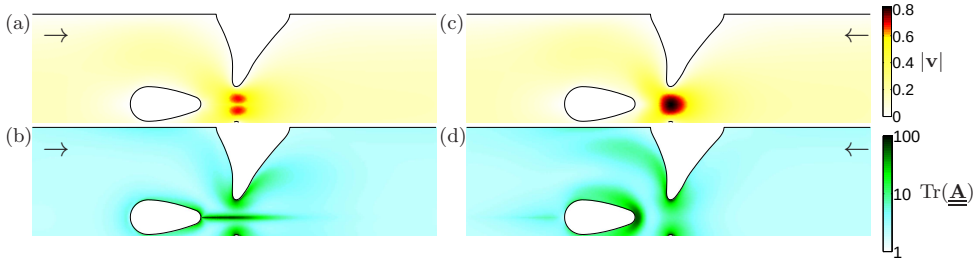

Figure 4.3: The working mechanism of the contraction-obstacle design as simulated by a 2D periodic and pressure driven FENE-CR model using $\eta_s/(\eta_p + \eta_s) = 0.59$, $a^2_{\max} = 100$, and We = 21.3 (based on the easy flow direction, see section 4.1.5). The damping from the microchannel floor and ceiling is described with a shallow channel approximation. The velocity (a) and (c) as well as the polymer extension (c) and (d) are plotted for both flow directions. The predicted flow rate ratio is $\mathrm{Di}_{\Delta p} = 1.10$. The simulations were performed with 439k degrees of freedom with enhanced resolution at the obstacle separation points.

4.1.5 Results

The Weissenberg number describes the ratio of elastic and viscous effects, with the Newtonian regime characterized by numbers much smaller than unity. For our geometry,

$$\mathrm{We} = \lambda \frac{v_{\mathrm{avg}}}{L_{\mathrm{char}}} = \lambda \frac{Q/(hw)}{w/2}, \tag{4.5}$$

where λ is the relaxation time of the fluid ($\approx$ 4 ms), while the average flow velocity, v_{avg}, divided by a characteristic length scale, L_{char}, defines a characteristic shear rate. In accordance with related experiments[38] we use the flow rate Q, to calculate the average velocity at the contraction and select the half contraction width, $w/2 = 19$ μm, as a characteristic length scale. This definition is applied for experimental and simulated data, but the simulations are pressure driven, so interpolation is used to estimate driving pressures at equal flow rates. Non-Newtonian fluids are usually better characterized using a spectrum of relaxation times, and the CaBER tends to detect the longer relaxation times in this spectrum, but these do not necessarily dominate in our geometry, and therefore the estimation of the Weissenberg number is not straightforward in practice.

The relevance of flow inertia can be quantified by the Reynolds number,

$$\mathrm{Re} \quad = \quad v_{\mathrm{avg}} \frac{\rho L_{\mathrm{char}}}{\eta} = \frac{Q}{hw} \frac{\rho w/2}{\eta}, \tag{4.6}$$

where ρ is the solution density (998 kg/m^3), and $\eta = \eta_p + \eta_s$ is the total viscosity (10^{-3} Pa s).

SDS was added in order to minimize progressive blocking due to small pieces of PDMS residue [see figure 4.4(a)] at the cost of more frequent blocking with large pieces of PDMS, as shown in figure 4.4(b). The severity of the first blocking issue is possibly due to the separation point of the obstacle, but blocking issues with *larger* pieces of PDMS have also been observed in contraction geometries. These *large* pieces are created as a consequence of hole punching with a hollow needle in the microchannel preparation, and it is thus possible that the blocking issue can be reduced by means of an alternative hole production technique.

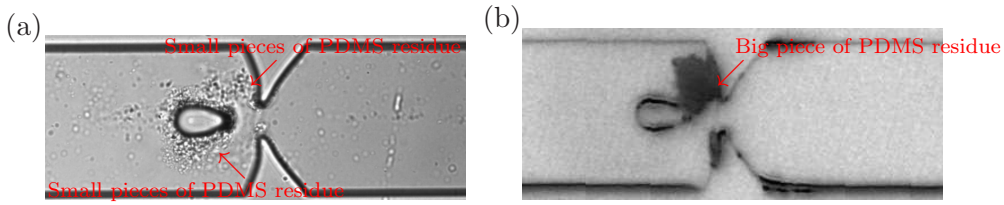

Figure 4.4: Small pieces of PDMS would give rise to progressive blocking around the obstacle (a). This problem could be eliminated by adding the surfactant SDS to the solution, but this procedure amplified the blocking of large PDMS pieces (b). The images were acquired in different microscopes, hence the overall qualitative difference.

Blocking seems to occur faster for large flow rates and therefore experiments were usually performed starting from small flow rates as to avoid early channel blocking of the severe kind that makes further characterization impossible. We show repeated pressure drop measurements for the same flow rate in figure 4.5 to illustrate the problem of more moderate blocking. The pressure drop is similar for the two flow directions up to a flow rate of about 30 μL/min. Above this point the hard flow direction breaks of, while the easy flow direction continues to exhibit a quasi linear increase of pressure drop up to 50 μL/min and even then the increase of the slope is more modest.

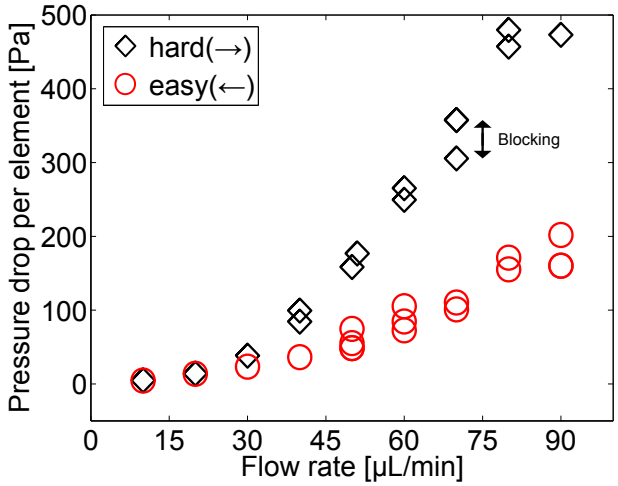

Figure 4.5: Pressure drop per element as function of the flow rate for the two flow directions. The effect of blocking is illustrated by repeated measurements at the same flow rate indicating that the effect of the flow direction dominates. Altogether the figure represents data from seven microchannels, but around 70 channel were fabricated and tested in total.

The diodicity is defined in terms of the driving pressure ratio at a given flow rate,

$$\mathrm{Di}_Q = \frac{\Delta p_{\mathrm{hard}(\rightarrow)}}{\Delta p_{\mathrm{easy}(\leftarrow)}}. \tag{4.7}$$

We use the minimum pressure drops Δp (corresponding to the least blocked experiment) to calculate the experimental diodicity for each flow rate. We plot the diodicity for both experiments and simulations[2] versus the Weissenberg number as well as the Reynolds number in figure 4.6. In order to quantify the degree of experimental reproducibility, we calculate diodicities based on the second lowest measured pressures, $\Delta p_{\min\#2}$, for the flow rates in the 60-80 μL/min regime. The experimental diodicity increases significantly at We $\approx$ 10, while the curve for the simulations increases much slower. The experimental reproducibility is around ± 0.5 for the diodicities in the 60-80 μL/min flow rate regime.

The discrepancy between simulations and experiments is not surprising in the sense that experiments show a significant pressure drop enhancement in contraction geometries[15], but closed-form differential viscoelastic models are currently unable to predict this basic phenomenon. Furthermore it is not until recently that the 3D viscoelastic flow at We = 2 has been computed in a simple benchmark geometry[24]. The presented simulations assume 2D flow, but early transition to 3D for flow around obstacles is known experimentally[23] as well as theoretically[24]. We thus hypothesize that the lack of agreement between theory and experiment can be partially attributed to the onset of a 3D flow structure above We $\approx$ 10 and/or the inability of the viscoelastic model to adequately predict the pressure drop in contraction flows.

The maximum diodicity of 3.5 is a factor of two smaller than what has been reported for hyperbolic contractions with large aspect ratios[46], but one should remember that this geometry is optimized for the regime of moderate elasticity, and it is thus worth emphasizing that the maximum occurs for a Weissenberg number of just 27, instead of around 70. Small aspect ratio hyperbolic rectifiers have similar peak diodicities, and these reach their maximum for We $\approx$ 45, but in this context the uncertainty of the relaxation time should be kept in mind.

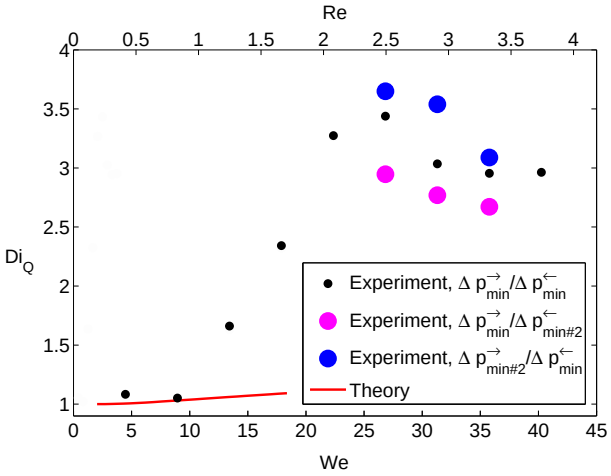

Figure 4.6: The driving pressure ratio is plotted versus the Weissenberg number indicating a maximum of 3.5 at We $\approx$ 27. The simulations reach a diodicity of 1.09 at a Weissenberg number of 18.4. The diodicities calculated using the second lowest measured pressures, $\Delta p_{\min\#2}$, indicate an experimental reproducibility of ± 0.5 for the diodicity.

We investigate the working mechanism using streak photography, as shown in figure 4.7. As typical for viscoelastic fluid flow, recirculation zones form on the upstream side of the contraction and these squeeze the flow to the sides of the obstacle in the case of the hard flow direction. The fact that the recirculation occurs on the upstream side indicates that elastic effects indeed are dominant, in agreement with the fact that the elasticity number, El = We/Re, is around 11 indicating a relatively high ratio of elastic over inertial stresses[53]. In the theo-

[2] $a^2_{\max} = 100$ and $\eta_s/(\eta_s + \eta_p) = 0.59$ were selected as parameter values.

retical optimizations[20] the diodicity was attributed to the strand of elongated polymers in the obstacle wake, but we are unable to see this effect experimentally, as it would require the use of birefringence techniques.

A break down of the rectifier diodicity for larger Weissenberg numbers is not captured in the experimental data. Instead, the diodicity seems to reach a plateau around 3, which could be due to the fact that the breakdown mechanism involves obstacle to obstacle and/or contraction to contraction interaction similar to what happens at higher Weissenberg numbers for the hyperbolic rectifiers. At least this kind of mechanism could require very large Weissenberg numbers, because of the relatively large length of periodicity. Asymmetric flow patterns are clearly documented by the streak photography in figure 4.7, so strong asymmetric flow patterns for both directions is another likely candidate for the break down mechanism, but further experiments at higher flow rates are required in order to investigate this important performance aspect.

One might expect that the flow of a Newtonian fluid at large Reynolds numbers could look similar to what is observed here, and for this reason the investigated geometry might perform well for Newtonian fluids as well. The working mechanism would however be different from previous contraction-obstacle rectifiers[47], in the sense that it relies on contraction recirculations rather than obstacle vortices due to the streamlined obstacle employed in this work. This means that the hard and easy directions would be switched around compared to the viscoelastic case, as also observed in triangular rectifiers[37].

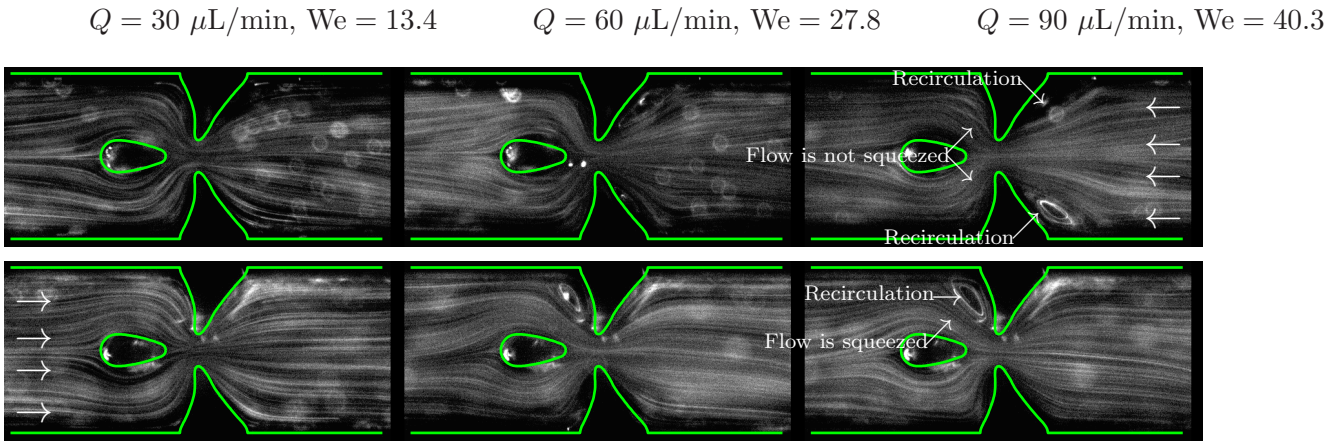

Figure 4.7: Flow patterns for the easy (top) and hard (bottom) flow directions at different flow rates. Upstream recirculation zones form for flow rates $Q = 60$ and 90 μL/min.

4.1.6 Conclusions

We successfully characterized a viscoelastic rectifier with a contraction-obstacle design and found a maximum diodicity of 3.5 at a Weissenberg number of 27, which is a verification of previous simulations[20] in the sense that these predicted the design to be optimal at moderate elasticity. Streak photography illustrated that the working mechanism can be attributed to elastic recirculations upstream of the contraction. Finally, the geometry has a potentially broad operating regime as the experimental data indicates a broad flow rate range of high diodicity.

4.1.7 Acknowledgments

The authors would like to acknowledge the Otto Mønsted foundation and FCT, COMPETE and FEDER through project PTDC/EME-MFE/114322/2009 for financial support to this work.

Chapter 5

Topology Optimization of Bistability

This chapter contains an article submitted to the journal of Structural and Multidisciplinary Optimization. The FENE-CR model was used for this work, and discovered some discrepancies between this, and other published works[17]. Based on correspondence with Manuel A. Alves from the University of Porto, we switched to a stress based formulation with the FENE-MCR model, which removed the discrepancies as illustrated in figure 5.1. We thus believe that the published works in fact used the FENE-MCR model and that we indeed are able to accurately describe bistability.

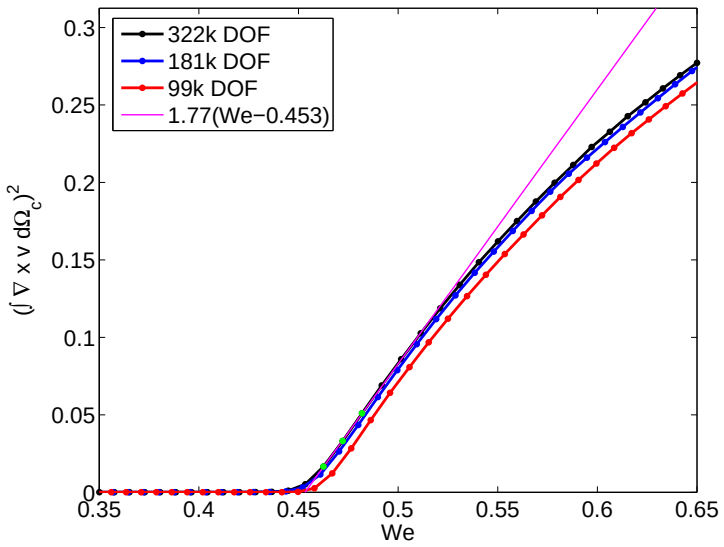

Figure 5.1: The rotation of a FENE-MCR fluid in the center of a cross-slot geometry is plotted as a function of the Weissenberg number for a solvent to total viscosity ratio of 0.1 and a maximum extensibility parameter of $a^2_{max} = 100$. The data has been generated using a transient simulation with Weissenberg numbers varying slowly in time, "quasi-static simulation". We show three different discretizations to illustrate the degree of convergence. Furthermore we perform a linear fit on the green points to estimate the Weissenberg number critical for bistability. This quantity is reported at 0.46 in [17] with slight asymmetry at 0.455.

5.1 [P4]: Optimization of Bistable Viscoelastic Systems

5.1.1 Abstract

We consider the flow of a viscoelastic fluid in a symmetric cross geometry. For small driving pressures the flow is symmetric, but beyond a certain critical pressure the symmetric flow becomes unstable; two stable asymmetric solutions appear, and forcing of the unstable symmetric flow beyond the critical pressure gives rise to increased hydraulic resistance. We have combined a state-of-the-art implementation for viscoelastic flow modeling with topology optimization in a high level finite element package (COMSOL). We use this framework on the cross geometry with the aim to reduce the critical driving pressure corresponding to the point of bistability, such that the effect is enhanced. The point of bistability is, however, not explicitly contained in the solution, so we opt for a heuristic approach based on the dissipation ratio between the asymmetric and unstable symmetric flow solutions. We find a design that significantly reduces the driving pressure required for bistability, and furthermore is in agreement with the approach followed by experimental researchers. Furthermore, by comparing the the two asymmetric solutions, we succesfully apply the same approach to a problem with two fluids meeting in the cross.

5.1.2 Introduction

Viscoelastic fluids appear in many industrial applications due to the presence of biological components and synthetic polymers, e.g. food and plastic processing respectively. The elastic character of these small constituents can cause large normal stresses which in turn can give rise to exceptional flow phenomena such as rod climbing, upstream recirculation and bistability. Differential constitutive equations are not only able to reproduce such phenomena, but also provide a good quantitative agreement with experiments [5]. We have showed that recent reformulations [54] have improved the robustness of these models to the extent that they can be combined with the method of topology optimization [32]. Note that the reformulations complicate linearization to the extent that tools capable of automatic differentiation are called for, a rarity in current research grade codes, and therefore we rely on a high-level implementation of topology optimization based on the density method [32] in COMSOL Multiphysics, a commercial finite element package [12]. Previously, we have used our implementation to find a novel material layout for a viscoelastic rectifier [20] and verified the performance experimentally [55]. Lately we have applied this optimization implementation to the cross-slot geometry, and this paper is dedicated to those results.

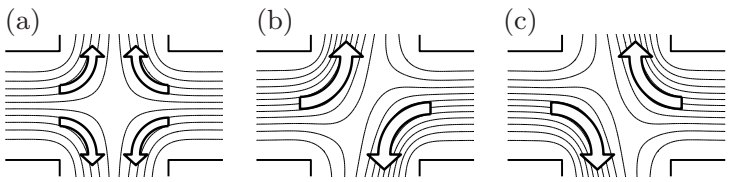

Figure 5.2: The viscoelastic flow in a cross is symmetric in the regime of low elasticity (a), but the symmetric flow becomes unstable in the regime of moderate elasticity. Instead two asymmetric solutions appear, (b) and (c).

When a viscoelastic fluid flows in a slot-cross geometry, large normal stresses arise as the fluid flows out the two side channels. The system lends itself to be described by a pitchfork bifurcation in the sense that the symmetric flow is stable in the low elasticity regime, while it becomes unstable and two asymmetric stable solutions appear in the regime of moderate

elasticity, see figure 5.2. This phenomenon of flow bistability has been observed experimentally [25] and reproduced numerically [13]. The unstable symmetric solution has been investigated in simulations, which revealed that the asymmetric flow corresponds to a lower hydraulic resistance. We use this observation to formulate a heuristic objective function that allows for minimization of the driving pressure at which bistability occurs. The heuristic approach is successful in the sense that the ideas of experimental researchers are reproduced [56], so we attempt to use the same approach for breaking the symmetry of the design. This is successful for a simple case, but a more advanced problem seems to call for optimization at the point of bistability.

5.1.3 Modeling

A simple way to describe orientation and extension of elastic fluid elements is by so called dumbbell models: Two point masses are connected with a spring, and the end-to-end vector, $\mathbf{a}$ describes orientation as well as extension through the conformation tensor

$$\underline{\underline{\mathbf{A}}} = \frac{\langle \mathbf{a} \otimes \mathbf{a} \rangle}{\mathrm{a}_{\mathrm{eq}}^2},$$

where a_{eq} is the equilibrium extension and $\langle \cdots \rangle$ is a statistical average. The trace of the conformation tensor thus expresses the dumbbell extension,

$$\mathrm{Tr}(\underline{\underline{\mathbf{A}}}) = \frac{\langle \mathbf{a}^2 \rangle}{\mathrm{a}_{\mathrm{eq}}^2}.$$

The conformation tensor is convected by the flow velocity, $\mathbf{v}$, while being stretched and rotated by the velocity gradient, $\boldsymbol{\nabla}\mathbf{v}$.

$$\frac{D\underline{\underline{\mathbf{A}}}}{Dt} = \left[\underline{\underline{\mathbf{A}}} \cdot \boldsymbol{\nabla}\mathbf{v} + (\boldsymbol{\nabla}\mathbf{v})^T \cdot \underline{\underline{\mathbf{A}}}\right] - \frac{k(\underline{\underline{\mathbf{A}}})}{\lambda}\left(\underline{\underline{\mathbf{A}}} - \underline{\underline{\mathbf{I}}}\right), \tag{5.1}$$

where $\underline{\underline{\mathbf{I}}}$ is the identity matrix, λ is the dumbbell relaxation time and D/Dt is the material derivative. The first and second terms on the right hand side of equation (5.1) correspond to stretching/rotation and relaxation respectively. The FENE-CR model employs a diverging spring constant modification for the relaxation, $k(\underline{\underline{\mathbf{A}}})$, and this puts an upper bound, $\mathrm{a}_{\mathrm{max}}$ on the dumbbell extension.

$$k(\underline{\underline{\mathbf{A}}}) = \frac{1}{1 - \mathrm{Trace}(\underline{\underline{\mathbf{A}}})/\mathrm{a}_{\mathrm{max}}^2} \tag{5.2}$$

The fact that $k(\underline{\underline{\mathbf{A}}})$ blows up as $\mathrm{Trace}(\underline{\underline{\mathbf{A}}}) \to a_{\mathrm{max}}^2$ reduces the effective relaxation time in this limit [see equation (5.1)]. The singular behavior of the spring constant can give rise to high spring tensions expressed by the dumbbell stress tensor,

$$\underline{\underline{\boldsymbol{\tau}}}_e = \frac{\eta_p}{\lambda} k(\underline{\underline{\mathbf{A}}})\left(\underline{\underline{\mathbf{A}}} - \underline{\underline{\mathbf{I}}}\right), \tag{5.3}$$

where η_p is the dumbbell viscosity. We assume that the dumbbells are in a Newtonian solvent, and that the flow is not only creeping, but also isothermal and incompressible. This means that requiring momentum conservation leads to the Stokes equation.

$$\mathbf{0} = \boldsymbol{\nabla} \cdot \left(-p\underline{\underline{\mathbf{I}}} + \eta_s \underline{\underline{\dot{\boldsymbol{\gamma}}}} + \underline{\underline{\boldsymbol{\tau}}}_e\right) - \alpha\mathbf{v}, \tag{5.4}$$

where p is the pressure, η_s is the solvent viscosity, $\underline{\underline{\dot{\boldsymbol{\gamma}}}} = \boldsymbol{\nabla}\mathbf{v} + (\boldsymbol{\nabla}\mathbf{v})^T$ is the strain rate tensor and $-\alpha\mathbf{v}$ is a damping term for use with topology optimization. To ensure mass conservation we add the usual continuity equation to the set of equations,

$$0 = \boldsymbol{\nabla} \cdot \mathbf{v}. \tag{5.5}$$

The FENE-CR model (5.1-5.5) is inspired by the FENE-P model [8], which exhibits shear thinning behavior. The FENE-CR model on the other hand has a constant shear viscosity, which better reflects the properties of the dilute polymer solutions often used to study viscoelastic effects in experiments[40].

5.1.4 Dimensionless Modeling

The FENE-CR model (5.1-5.5) can be written in terms of the dimensionless variables $\tilde{x}$, $\tilde{v}$, $\tilde{t}$, $\tilde{p}$, $\underline{\underline{\tilde{\tau}}}_e$ and $\tilde{\alpha}$

$$\begin{aligned} \mathbf{x} &= L_{\text{char}}\tilde{\mathbf{x}}, \quad \mathbf{v} = \frac{p_{\text{char}}L_{\text{char}}}{\eta_s+\eta_p}\tilde{\mathbf{v}}, \quad t = \frac{\eta_s+\eta_p}{p_{\text{char}}}\tilde{t}, \\ p &= p_{\text{char}}\tilde{p}, \quad \underline{\underline{\boldsymbol{\tau}}}_e = p_{\text{char}}\underline{\underline{\tilde{\boldsymbol{\tau}}}}_e \quad \text{and} \quad \alpha = \alpha_{\max}\tilde{\alpha}. \end{aligned}$$

We wish to perform pressure driven calculations, and therefore we define a characteristic velocity in terms of characteristic pressure, p_{char} rather than the other way around. The dimensionless variables yield

$$\begin{aligned} 0 &= \tilde{\boldsymbol{\nabla}}\cdot\left(-\underline{\underline{\mathbf{I}}}\tilde{p}+\beta\left[\tilde{\boldsymbol{\nabla}}\,\tilde{\mathbf{v}}+\left(\tilde{\boldsymbol{\nabla}}\,\tilde{\mathbf{v}}\right)^T\right]+\underline{\underline{\boldsymbol{\tau}}}_e\right)-\text{Da}^{-1}\tilde{\alpha}\tilde{\mathbf{v}}, \\ \frac{D\underline{\underline{\mathbf{A}}}}{D\tilde{t}} &= -\frac{k(\underline{\underline{\mathbf{A}}})}{\text{We}}\left(\underline{\underline{\mathbf{A}}}-\underline{\underline{\mathbf{I}}}\right)+\left[\underline{\underline{\mathbf{A}}}\cdot\tilde{\boldsymbol{\nabla}}\,\tilde{\mathbf{v}}+\left(\tilde{\boldsymbol{\nabla}}\,\tilde{\mathbf{v}}\right)^T\cdot\underline{\underline{\mathbf{A}}}\right], \\ \underline{\underline{\boldsymbol{\tau}}}_e &= \frac{1-\beta}{\text{We}}k(\underline{\underline{\mathbf{A}}})\left(\underline{\underline{\mathbf{A}}}-\underline{\underline{\mathbf{I}}}\right) \quad \text{and} \\ k(\underline{\underline{\mathbf{A}}}) &= \frac{1}{1+\text{Trace}(\underline{\underline{\mathbf{A}}})/L^2}, \end{aligned}$$

where the following characteristic physical parameters have been introduced

$$\begin{aligned} \text{We} &= \frac{\{\text{elastic effects}\}}{\{\text{viscous effects}\}} = \frac{\lambda\Delta p}{\eta_s+\eta_p} = 0.75, \\ \beta &= \frac{\{\text{viscous effects due to solvent}\}}{\{\text{total viscous effects}\}} = \frac{\eta_s}{\eta_s+\eta_p} = 0.2, \\ a^2_{\max} &= 100 \quad \text{and} \quad \Delta p = 67.2p_{\text{char}}. \end{aligned} \tag{5.6}$$

These physical non-dimensional parameters represent the relative magnitude of the quantities between curly brackets. Note that a Newtonian fluid is recovered in the limit of the Weissenberg number, We going to zero or the solvent to total viscosity ratio, β going to 1. Typical values of the physical parameters are listed in equation (5.6), while numerical parameters such as the Darcy number, Da are treated in section 5.1.6 on topology optimization.

5.1.5 Numerical Implementation

When the FENE-CR model is analyzed with the finite element method, the velocity components are usually taken as 2nd order Lagrange polynomials with C^0 continuity, but this causes discontinuity of the velocity gradients, $\boldsymbol{\nabla}\,\mathbf{v}$. This can be solved by introducing a continuous approximation, $\underline{\underline{\mathbf{G}}}$, for use in equation (5.1). Furthermore small solvent viscosities can cause the Stokes equation (5.4) to lose its elliptic character[18] and therefore $0 = \eta_p(\underline{\underline{\mathbf{G}}}+\underline{\underline{\mathbf{G}}}^T-\boldsymbol{\nabla}\,\mathbf{v}-(\boldsymbol{\nabla}\,\mathbf{v})^T)$ is added on the right-hand side of equation (5.4). Finally equation (5.1) can be reformulated [54] such that it is the logarithm of the conformation tensor, $\underline{\underline{\mathbf{s}}}$, that is convected. This ensures that the conformation tensor $\underline{\underline{\mathbf{A}}} = e^{\underline{\underline{\mathbf{s}}}}$ remains positive definite, which improves robustness.

We use SUPG stabilization to handle the convection-reaction equations (5.1) in the sense that we multiply with $\underline{\underline{\mathbf{s}}}_{\text{test}} + 2h_{\text{mesh}}(\boldsymbol{\nabla}\underline{\underline{\mathbf{s}}}_{\text{test}} \cdot \mathbf{v})$ rather than just $\underline{\underline{\mathbf{s}}}_{\text{test}}$, when we convert to the weak formulation.

We find a steady solutions by

#1 finding the solution corresponding to Stokes flow and setting $\underline{\underline{\mathbf{s}}} \approx \underline{\underline{\mathbf{0}}}$.

#2 initializing a transient solver with #1 and evolving for many relaxation times.

#3 initializing a static solver with #2.

We use 2^{nd} order polynomials for $\mathbf{v}$ and 1^{st} order for p, $\underline{\underline{\mathbf{G}}}$, $\underline{\underline{\mathbf{s}}}$ and $\underline{\underline{\boldsymbol{\tau}}}_e$, which is a standard choice within modeling of viscoelastic fluids [41]. Finally there are two variables, θ and $\tilde{\theta}$, which are related to the topology optimization as explained in section 5.1.6. θ is discontinuous as it takes a constant value in every element, while $\tilde{\theta}$ is approximated with 2^{nd} order polynomials.

Although we would like to applaud the general progress within modeling of viscoelastic fluids in complex geometries, we also have to stress that the models remain computationally intensive due to the presence of two tensor variables. This means that state-of-the-art 3D simulations are carried out on supercomputers and even then only in simple benchmark geometries [41, 24]. Furthermore, computations in the regime of high viscoelasticity is limited by the presence of small time and length scales in what is collectively referred to as viscoelastic turbulence. Presently no viscoelastic turbulence models exists. The results presented in the following are thus limited to steady 2D flow in the regime of low to moderate viscoelasticity.

5.1.6 Topology Optimization

We are interested in optimizing devices relying on viscoelastic effects, but it is well known that the magnitude of viscoelastic effects increases at small length scales and the very nature of our optimization problems thus has the potential to result in designs with length scales identical to that of the numerical discretization. This entails not only poor, if not unphysical, numerical approximation of the governing equation, but also the risk of unsteady flow, the presence of which cannot be handled by the applied optimization implementation. Consequently we wish to impose a lower bound $L_{\min}$ on the length scale of the design variable, θ, and this can be achieved by using the PDE filter [33] to compute the filtered design variable, $\tilde{\theta}$. The filter unfortunately also gives rise to larger areas of intermediate material, and therefore we use a projection function [42], before applying the usual convex relation [26].

$$\tilde{\theta} = \theta + L_{\min}^2 \boldsymbol{\nabla}^2 \tilde{\theta} \tag{5.7}$$

$$\bar{\theta} = \tfrac{1}{2} + \frac{\tanh(\xi(\tilde{\theta} - \tfrac{1}{2}))}{2\tanh(\xi/2)} \tag{5.8}$$

$$\alpha = \alpha_{\max} \frac{q(1-\bar{\theta})}{\bar{\theta} + q} \tag{5.9}$$

where ξ and q determines the steepness of the projection and convexity of the inverse permeability in the projected design variable, $\bar{\theta}$. Ideally ξ, $\alpha_{\max}$ and q should be as large as possible, while the filter length $L_{\min}$ should be small. The convexity of the optimization problem however decreases in these limits. We have found a set of parameters that facilitates a good compromise between acceptable approximation of the physics in solid and fluid areas as well as an objective

found that is sufficiently smooth with respect to variations of the design variables

$$\begin{aligned} L_{\min} = h_{\text{mesh}}, \quad \xi &= 10, \quad q = 4 \cdot 10^{-6} \quad \text{and} \\ \text{Da} = \frac{\{\text{viscous effects in solid}\}}{\{\text{damping effects in solid}\}} &= \frac{\eta_s + \eta_p}{L^2 \alpha_{\max}} = 10^{-5}, \end{aligned} \tag{5.10}$$

where the Darcy number Da has been introduced in terms of the characteristic length scale L. It describes the magnitude of viscous forces relative to damping forces in solid regions, and it thus belongs among the other numerical parameters. Should a design without a steady solution appear, we use the final transient solution to calculate the derivative of the objective function, ϕ. This gradient is used to improve the design in an iterative way using the method of moving asymptotes [28].

We find it convenient to introduce symmetry by defining

$$\theta_{\text{sym}} = (\theta + \theta(x, -y))/2, \tag{5.11}$$

and using θ_{sym} in place of θ in the PDE filter (5.7). Equation (5.11) is specific to a horizontal symmetry axis as used in the following section, but it is straight forward to generalize it to vertical or 180 degree rotational symmetry. It is usual for topology optimization of fluid problems to involve some degree of approximation for the solid regions, but we find that the relation between the design variables and the damping term (5.7-5.9) gives rise to rather large areas of intermediate damping, and therefore we have performed verification simulations in geometries inspired by the optimization results.

5.1.7 Cross with Horizontal Symmetry

The cross geometry is illustrated in figure 5.3 with a forced horizontal symmetry axis for the design, inlets to the sides and outlets in the upper and lower channels. The channel width, L, is chosen as characteristic length scale and the size of the design domain is taken as $L_d = 2L$. The system is pressure driven, and at a critical driving pressure the system goes through a pitchfork bifurcation as sketched in figure 5.4.

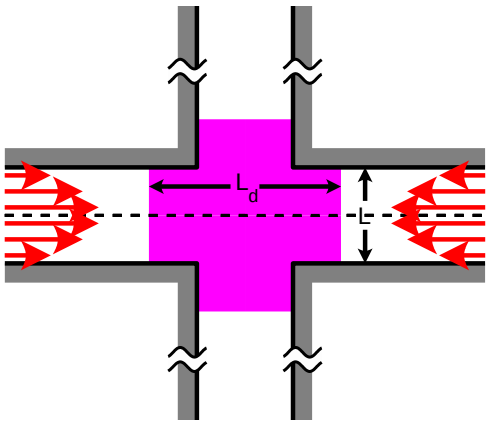

Figure 5.3: The setup for optimization of the symmetric cross is shown with inlets to the sides and a central design domain (pink). Note that the design is mirrored around the dashed symmetry line. The distance from the center to the inlets is $2L$, while it is $4L$ for the outlets. The flow is pressure driven with $\underline{\underline{\mathbf{A}}} = \underline{\underline{\mathbf{I}}}$ at the inlets.

The system can be forced in the unstable symmetric solution by enforcing zero normal flow along the symmetry line, which gives rise to an increased hydraulic resistance and thus smaller

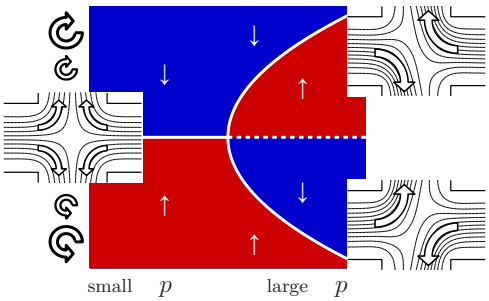

Figure 5.4: A pitchfork bifurcation is sketched with rotation as solution variable on the y-axis. Red and blue areas represent areas with increasing clock- and counterclockwise rotation, respectively. The insets show the symmetric and two asymmetric solutions at their respective positions in the diagram.

dissipation as outlined in figure 5.5. Note that the dissipation would have a maximum rather than a minimum in the case of a flow rate driven setup. The point of bistability appears implicitly in the solution, so it is not straightforward to optimize for it. We opt for a heuristic approach based on the dissipation ratio between the unstable and one of the stable solutions, i.e.

$$\begin{aligned} \phi &= P_{\text{asym}}/P_{\text{sym}} \quad \text{where} \\ P &= \int_\Omega \left(\dot{\underline{\underline{\tilde{\gamma}}}} : (\underline{\underline{\tilde{\tau}}}_s + \underline{\underline{\tilde{\tau}}}_e) + \text{Da}^{-1} \tilde{v}^2 \right) d\Omega, \end{aligned}$$

where : is the Frobenius product and ϕ is the objective function, which by convention should be minimized. That is we hope to decrease the critical driving pressure by pulling apart the two curves in figure 5.5. We use the physical parameters of equation (5.6), and it now makes sense to remark that the relation between the driving pressure and the characteristic pressure serves to put the average inlet velocity close to unity for the empty design, while $\beta = 0.2$ is an upper limit for the existence of bistability in the first place.

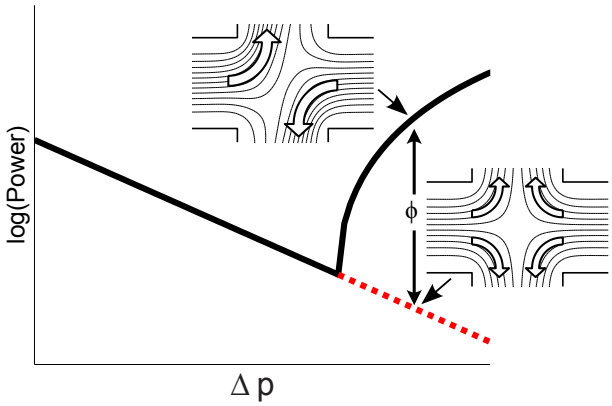

Figure 5.5: The logarithm of the power dissipation is outlined as a function of the driving pressure for the stable (black) and unstable flow solutions (red). The distance between the two curves, ϕ, is the ratio between the power dissipation in the two states. The idea is to choose ϕ as objective function, such that the curves are pulled apart, and the point of bistability is moved to the left – assuming that the slope of the curves is unaffected.

Figure 5.6 shows the result of an optimization with these physical parameters and the numerical parameters of equation (5.10). It is not surprising that the optimization produces contractions, since this approach has been used to increase the effective Weissenberg number in

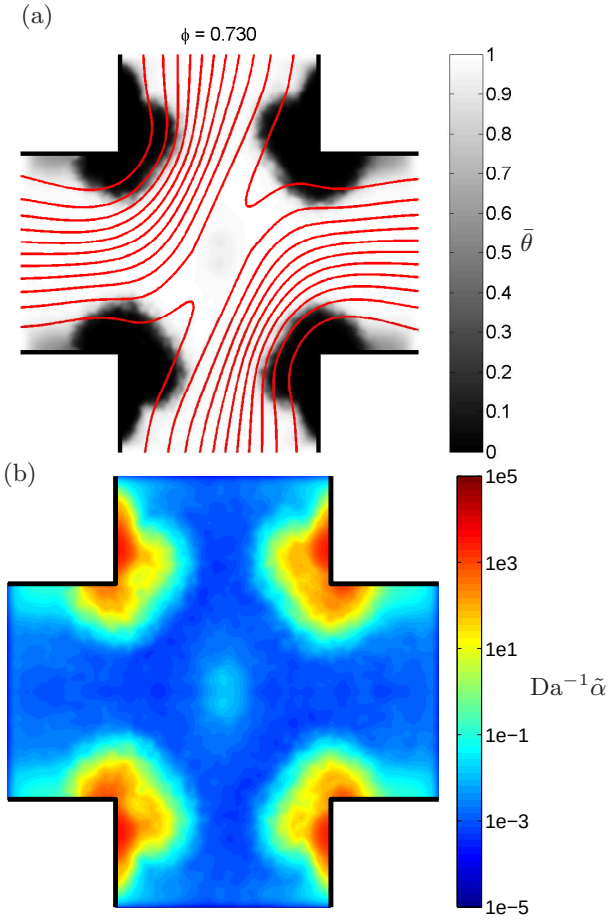

Figure 5.6: Topology optimization of the cross for maximum dissipation ratio gives rise to contractions in the corners as shown with the projected design variable in (a). The damping field pictured in (b) is however rather smeared out due to the convex interpolation in equation (5.9).

experiments[56]. The contractions keep growing as long as the shear rate (and thus the effective We number) increases, but at some point the pressure driven nature of the system causes the flow rate to drop. It thus seems that the optimal contraction width goes to zero for increasing length of the outlet channels. Although the filtered design variable in figure 5.6(a) is reasonably discrete, the damping field in figure 5.6(b) is not. Increasing the projection steepness ξ leads to unsteady solutions, so the fuzzy boundaries seem to avoid large local Weissenberg numbers by hiding the small length scale of the elements. It is possible that the problem can be solved using a shape optimization technique, but we have just performed simulations in a geometry inspired from the result of the optimization. The purpose of this is to verify that the working mechanism does not depend on the damping term in a way that is not physical. Note that these simulations are performed by slowly ramping down We:

$$\mathrm{We} = \mathrm{We}_{\max} + \mathrm{st}(t)\,(\mathrm{We}_{\min} - \mathrm{We}_{\max}) \tag{5.12}$$

where $\mathrm{st}(t)$ is a regularized step function[1] with a width of $T_{\mathrm{step}} = 4000\mathrm{We}_{\max}(0.035L/h_{\mathrm{mesh}})$. The idea is to make the variation so slow, that a quasi-steady solution is obtained. We integrate the vorticity over the center of the domain,

$$\Omega_c = \tilde{\mathbf{x}} \in |\tilde{\mathbf{x}}|_\infty < 0.5,$$

[1] We use a third order polynomial to construct the step function.

for each We number, as we find that the square of this is a good measure of asymmetry. In figure 5.7 we thus plot this quantity versus We numbers based on the flow rates,

$$\mathrm{We}_{\dot{V}} = \lambda \frac{\mathrm{v}_{avg,inlet}}{L} = \mathrm{We}\tilde{\mathrm{v}}_{avg,inlet},$$

for easier comparison with literature, but in fact no reference exists for the FENE-CR model[2]. The figure indicates a significant decrease in the driving pressure critical for bistability, and as such it shows that the heuristic approach is viable. In the next section we will investigate, whether it can also be applied in the context of asymmetric bistability.

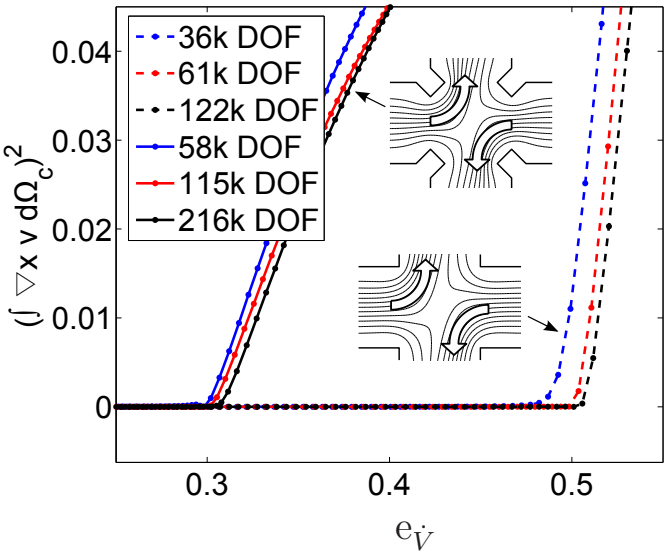

Figure 5.7: The integral of the vorticity is squared and plotted as a function of $\mathrm{We}_{\dot{V}}$ for two designs using different number of degrees of freedom (DOF). The simulations for the empty design (dashed lines) converge to indicate a point of bistability at $\mathrm{We}_{\dot{V}} = 0.5$, while the simulations of the contraction design indicate a much smaller value, although these results are not fully converged. The contraction design is produced by subtracting the small squares from the empty design. The squares are centered on the corners, rotated 45 degrees and have a side length of $L/4$.

5.1.8 Cross with Vertical Symmetry, Two Fluids Simultaneously

In this section we consider the flow of two fluids with slightly different relaxations times meeting in a cross as illustrated in figure 5.8. Apart from a vertical symmetry axis and a design domain confined to the corners, the setup is identical to the previous problem. One could apply the system as a rheometer relying on a reference fluid. In other words it could answer the question "is the new fluid or more or less viscoelastic than the old one?". We model the different relaxation times by convecting a marker field c,

$$\begin{aligned}
\mathbf{v}\cdot\boldsymbol{\nabla} c &= 0, \ \text{in}\,\Omega, \quad \text{with} \quad c = 0 \ \text{at left inlet}, \quad \text{and} \\
c &= 1 \ \text{at right inlet}, \\
\bar{c} &= \tfrac{1}{2} + \frac{\tanh(\xi_c(c-\tfrac{1}{2}))}{2\tanh(\xi_c/2)}, \quad \text{and} \\
\mathrm{We} &= \mathrm{We}_{\text{left}} + \bar{c}\,(\mathrm{We}_{\text{right}} - \mathrm{We}_{\text{left}})
\end{aligned}$$

[2]Based on personal correspondence with Manuel A. Alves, we believe [17] presents results for the FENE-MCR model.

where we choose $\xi_c = 4$, 1st order polynomials for c and SUPG stabilization for the convective equation. Our hypothesis is that an arbitrary design without a horizontal symmetry axis causes different dissipations for the two stable solutions in the manner outlined in figure 5.10, which should reflect that one of the solutions has become disconnected from the solution at low pressure as also sketched in figure 5.9. We aim to maximize asymmetry, such that the system favors the solution where the fluid with the smaller relaxation time coming from the left goes up (clockwise flow). This corresponds to maximizing the gap in figure 5.10, i.e.

$$\phi = P^{\circlearrowleft}_{\text{asym}} / P^{\circlearrowleft}_{\text{asym}}, \tag{5.13}$$

where $P^{\circlearrowleft}_{\text{asym}}$ refers to the dissipation for the solution with most of the flow coming from the left going up.

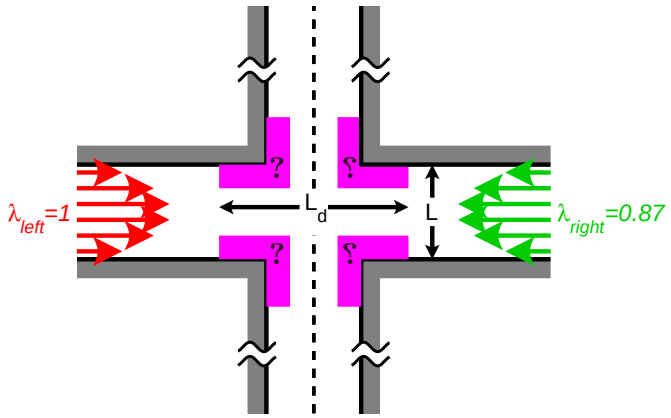

Figure 5.8: The optimization setup for two fluids with different relaxation times meeting in a cross is illustrated. Note that the design domain is confined to the corners and mirrored around the dashed symmetry line. The distance from the center to the inlets is $2L$, while it is $4L$ for the outlets. The flow is pressure driven with $\underline{\underline{\mathbf{A}}} = \underline{\underline{\mathbf{I}}}$ at the inlets.

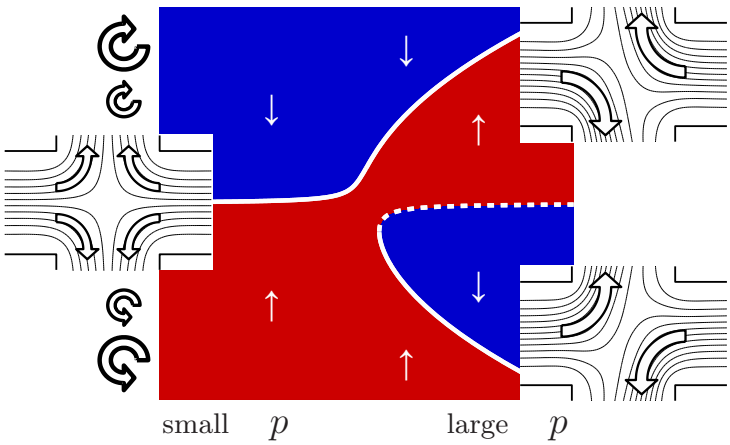

Figure 5.9: An asymmetric pitchfork bifurcation is sketched with rotation as solution variable on the y-axis. Red and blue areas give rise to increasing clock- and counterclockwise rotation, respectively. The insets do not show the asymmetry of the design, only the qualitative features of the stable solutions at their respective positions in the diagram.

In order to reliably compute both of the dissipations in the objective (5.13), we impose a time-dependent damping field listed in the appendix. The effect of this is that we start every

simulation with a diagonal wall to establish one of the states, before slowly removing this wall and enforcing the actual design.

In terms of physical parameters we keep $\beta = 0.2$, $a^2_{max} = 100$, $\Delta p = 67.2 p_{char}$, and set $We_{left} = 0.75$ and $We_{right} = 0.87 We_{left}$. This results in a contraction at the upper outlet (see figure 5.10), which indicates that the larger dissipation is related to having the fluid with the longer relaxation time flowing through the contraction.

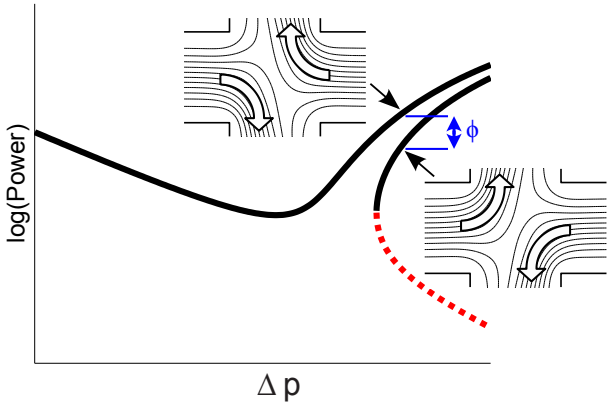

Figure 5.10: The logarithm of the power dissipation is outlined as a function of the driving pressure in the case of an asymmetric design. The unstable solutions is shown with a dashed red line, and the stable solutions are drawn in black. The distance between the two stable solutions, ϕ, is the ratio between the power dissipation in the two states.

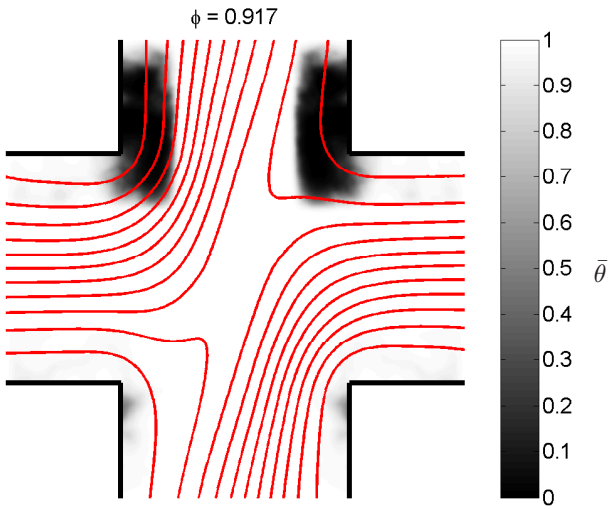

Figure 5.11: Topology optimization of the cross with two fluids for maximum dissipation ratio gives rise to a contraction at the upper outlet. Streamlines are only shown for the solution with the higher dissipation.

There is a significant amount of flow going through the solid regions in figure 5.11, so we we once again validate the result by performing simulations in a design inspired by the optimization as shown in figure 5.12. Note that these simulations are performed by starting from the state with counterclockwise flow and slowly ramping down the pressure (both We_{left} and We_{right}) similar to equation (5.12), before ramping it back up again such that the total simulation time becomes $2T_{step}$. When we plot the squared integrated vorticity and dissipation in figures 5.12a 5.12b, We see a transient discontinuity as predicted by figures 5.9 and 5.10. This is in agreement

with the expectation, and we can thus conclude that the heuristic approach based on dissipations can be used to optimize for asymmetry.

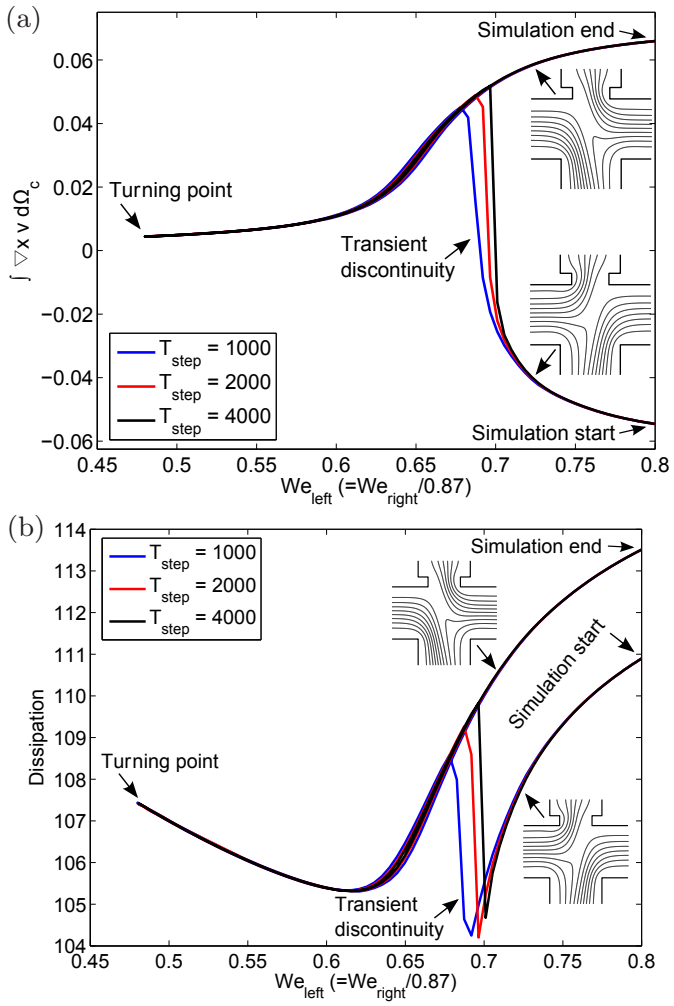

Figure 5.12: The squared integral of the vorticity (a) and the dissipation (b) are plotted as a function of $\mathrm{We}_{\mathrm{left}}$. The simulation is initialized the stable counterclockwise solution (see inset), but it jumps to the upper solution as the Weissenberg number is decreased. The jump appears steeper as the simulation is performed slower, which indicates a shift from one stable solution to another. The contraction design is produced by subtracting the small squares from the empty design. The squares have a side length of $0.2L$, and 104 thousand degrees of freedom is used for each time step.

5.1.9 Cross with Rotational Symmetry, Two Fluids, not Simultaneously

Devices for measuring the maximum extensibility parameter have been realized experimentally [57], but it is the relaxation time of the fluid that has received the most interest due to its status as the primary parameter of the fluid. In this section we explore the idea of a device capable of measuring secondary viscoelastic parameters, such as the solvent to total viscosity ratio, by making the asymmetry of the cross-slot selective to the fluid flowing, i.e. the clockwise flow is chosen for $\beta = 0.15$, while the counterclockwise is chosen for $\beta = 0.2$, see figure 5.13. In theory such a device is capable of distinguishing perfectly between fluids with solvent to total viscosity ratios smaller and larger than some critical value, approximately 0.175 in this case. In practice,

accuracy would be limited by the continuity of the fluid, thermal fluctuation and other effects not considered in the model. There is also the option of analyzing the sensitivity of the critical value with respect to the design, such that a range of design with different critical values can be generated. These designs can then be realized together in a microfluidic system capable of measuring the actual value of the solvent to total viscosity ratio with an accuracy dictated by the number of designs.

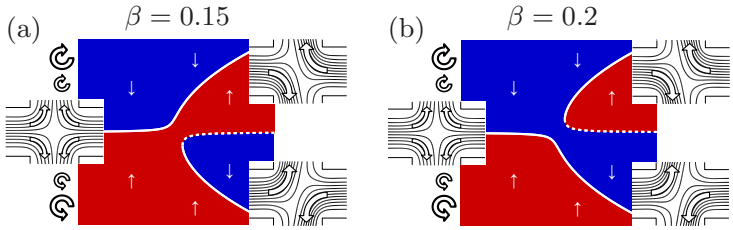

Figure 5.13: The idea of asymmetry selective to the fluid is presented. The system should select different asymmetric solutions depending on whether $\beta = 0.15$ or $\beta = 0.2$.

We aim to achieve asymmetry selective to the fluid by considering the dissipation, as this approach was successful for the previous example. This time we minimize the larger of the two objective functions (min-max problem),

$$\begin{aligned} \phi &= \max\left(\phi_{\beta=0.2}, \phi_{\beta=0.15}\right) \quad \text{where} \\ \phi_{\beta=0.2} &= P^{\circlearrowleft}_{\beta=0.2}/P^{\circlearrowright}_{\beta=0.2} \quad \text{and} \\ \phi_{\beta=0.15} &= P^{\circlearrowleft}_{\beta=0.15}/P^{\circlearrowright}_{\beta=0.15}. \end{aligned} \tag{5.14}$$

We assume that the favored flow solution has the bigger dissipation, as this is what we saw for the previous examples. It basicly means that the black curves in figure 5.10 cannot cross, and that decreasing both objective functions below unity, yields the desired effect. This approach requires that we simulate the flow of a fluid with a solvent to total viscosity ratio of $\beta = 0.2$ and then $\beta = 0.15$. We furthermore compute the dissipation for both the clockwise and counterclockwise flow using the time varying damping field listed in the appendix. Apart from a design with 180 degree rotational symmetry, the setup is identical to that illustrated in figure 5.3. For the physical parameters we keep $\mathrm{We} = 0.75$ and $\mathrm{a}^2_{\max} = 100$, but we increase the distance between the center and the outlet to $8L$ and set $\Delta p = 112 p_{\mathrm{char}}$ to compensate for the increased resistance.

The gradients of the objective functions $\phi_{\beta=0.2}$ and $\phi_{\beta=0.15}$ are highly antiparallel, and we have only been able to improve on the initial symmetric design by employing the globally convergent version of the method of moving asymptotes [58]. We use a mesh with horizontal as well as vertical symmetry. Figure 5.14(a) shows the optimization result for this problem with obstacles placed asymmetrically in inlets and outlets. The objective functions deviates less from unity compared to the previous examples as one would expect due to the difficulty of the problem. The fact that the optimization is not converged also plays a role, but further optimization is pointless, because the quasi-steady analysis shown in figure 5.14(b) reveals that the dissipation curves for the two states cross in the case of $\beta = 0.2$. That is, the optimization strategy is flawed, so better objective functions will not give the desired effect. A possible solution is to carry out the optimization at a Weissenberg much closer to the point of bistability, but this requires estimation of the point of bistability at every iteration.

5.1.10 Conclusion

We have been able to combine the method of topology optimization with models for viscoelastic flow in the cross-slot geometry, known to feature bistable solutions. We used the combination

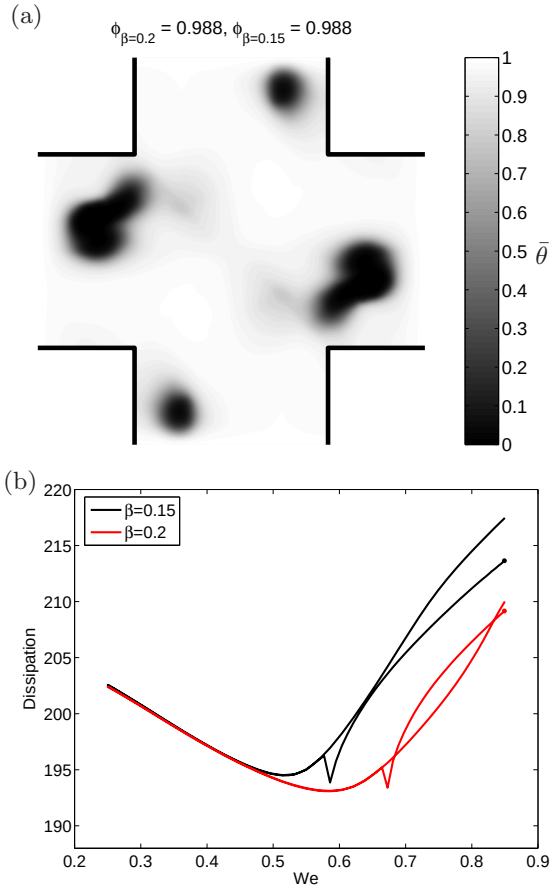

Figure 5.14: Topology optimization of the cross for asymmetry selective to the fluid is shown with obstacles at inlets and outlets as shown in (a). The optimization is not converged, but the analysis in (b) reveals that the dissipation curves for the two states cross in the case of $\beta = 0.2$, making further optimization pointless. We use the result of the optimization directly for the analysis and vary the Weissenberg number in a way similar to the previous problems with both simulations started in the counterclockwise state using the equation in the appendix. The start of the simulation is indicated by points, and the jumps after the minimum dissipation indicate the point of bistability, and that it is the counterclockwise solution that is disconnected for both fluids (the black curves do not cross).

to find a design that gives rise to early bistability using a heuristic objective function based on the ratio of dissipation between an unstable and a stable solution. We successfully used the same approach on an asymmetric version of the same bistable system. Finally, we presented our attempt at making the asymmetry selective to the fluid.

5.1.11 Aknowledgement

The presentation of preliminary results at the 17th International Workshop on Numerical Methods for Non-Newtonian Flows (IWNMNNF17, Blois, France) was supported by Reinholdt W. Jorck and Wife's foundation, while the presentation of the final results at the 10th World Congress on Structural and Multidisciplinary Optimization (WCSMO10, Orlando, USA) was supported by the Fabrikant P.A. Fisker Foundation.

Appendix

In order to reliably compute both of the dissipations in the objectives (5.13) and (5.14), we impose a time-dependent damping field,

$$\alpha = \begin{cases} \alpha_0 & , \quad \tilde{t} < 10\mathrm{We}_{\mathrm{left}} \\ \alpha_0[2 - \tilde{t}/(10\mathrm{We}_{\mathrm{left}})]^2 & , \quad 10\mathrm{We}_{\mathrm{left}} \leq \tilde{t} < 20\mathrm{We}_{\mathrm{left}} \\ \alpha_D[\tilde{t}/(10\mathrm{We}_{\mathrm{left}}) - 2]^2 & , \quad 20\mathrm{We}_{\mathrm{left}} \leq \tilde{t} < 30\mathrm{We}_{\mathrm{left}} \\ \alpha_D & , \quad 30\mathrm{We}_{\mathrm{left}} \leq \tilde{t} \end{cases}, \quad \text{where}$$

$$\alpha_0 = \begin{cases} \alpha_{\max} & , \quad |\tilde{x}| < 1 \ \& \ |\tilde{y}| < 1 \ \& \ \tilde{y} - 0.2 < \tilde{x} < 0.2 + \tilde{y} \\ 0 & , \quad \text{otherwise} \end{cases}, \quad \text{for } P^{\circlearrowleft}_{\mathrm{asym}} \text{ and}$$

$$\alpha_0 = \begin{cases} \alpha_{\max} & , \quad |\tilde{x}| < 1 \ \& \ |\tilde{y}| < 1 \ \& \ -\tilde{y} - 0.2 < \tilde{x} < 0.2 - \tilde{y} \\ 0 & , \quad \text{otherwise} \end{cases}, \quad \text{for } P^{\circlearrowleft}_{\mathrm{asym}}$$

that is we start every simulation with a diagonal wall, α_0, to establish one of the states, before slowly removing this wall and enforcing the actual design, α_D, given by the right-hand side of equation (5.9).

Chapter 6

Concluding Remarks

6.1 Conclusions

Topology optimization has been extended far beyond structural problems and many flow problems have been studied. Some of these have considered non-Newtonian effects using generalized Newtonian models, but this thesis constitutes the first attempt at using the method with differential constitutive equations. This has allowed for the study of new problems, but the robustness of the models as well as the discreteness of the design are areas worthy of further study

Nevertheless, a viscoelastic rectifier was successfully designed using the method of topology optimization, and though the optimization was carried out at moderate elasticity, experiments showed the resulting design to be competitive with previous designs in the regime of optimal performance, which occurs for unsteady flows at high elasticity.

Furthermore we applied the optimization to the bistable flow of the cross-slot geometry using a heuristic approach. This was successful for two simple cases, while a more tricky problem seemed to call for optimization exactly at the point of bistability, a prospect we did not investigate.

Finally the COMSOL 4.3a model implementation was published, and we hope this will inspire other researchers in modeling viscoelastic fluids.

6.2 Future work

- The fact that the viscoelastic flow tends to be stabilized by the smeared out boundaries of the PDE filter in topology optimization is a subject not completely understood. In example, the sharp corners of the cross-slot geometry do not pose a problem, but perhaps this is due to the fact that the no-slip boundary conditions are enforced explicitly. If that is the case, it might be advantageous to apply shape optimization with an explicit boundary representation.

- Small time and length scales limit computation in the regime of high elasticity similar to inertial flow at high Reynolds numbers. The latter has however been addressed with turbulence models, but something similar has yet to be developed for viscoelastic flow. Verification of such models will have to be performed against large-scale computations as well as experiments. Measurements without influence of inertia however require small length scales and thus the use of microfluidics, which is a subject of many issues in itself.

- On the experimental side, publication bias with respect to positive results is an issue in all areas of science, but microfluidics is something on its own in this regard. Experiments

are often performed more than 10 times, before a usefull results is produced. These issues of reproducibility and robustness are rarely mentioned in articles, which not only prevents progress, but also limits industrial interest in the field.

Chapter 7

Bibliography

[1] MA Hulsen, APG Van Heel, and BHAA Van Den Brule. Simulation of viscoelastic flows using brownian configuration fields. *Journal of Non-Newtonian Fluid Mechanics*, 70(1): 79–101, 1997.

[2] PJ Daivis, ML Matin, and BD Todd. Nonlinear shear and elongational rheology of model polymer melts by non-equilibrium molecular dynamics. *Journal of non-newtonian fluid mechanics*, 111(1):1–18, 2003.

[3] Stephen D Senturia. *Microsystem design*, volume 3. Kluwer academic publishers Boston, 2001.

[4] Robert Byron Bird, Robert C Armstrong, and Ole Hassager. *Dynamics of polymeric liquids. Vol. 1: Fluid mechanics*. John Wiley and Sons Inc., New York, NY, 1987.

[5] Frank Baaijens, Sjaak HA Selen, Hans PW Baaijens, Gerrit WM Peters, and Han EH Meijer. Viscoelastic flow past a confined cylinder of a low density polyethylene melt. *Journal of non-newtonian fluid mechanics*, 68(2):173–203, 1997.

[6] Wilco MH Verbeeten, Gerrit WM Peters, and Frank Baaijens. Numerical simulations of the planar contraction flow for a polyethylene melt using the xpp model. *Journal of non-newtonian fluid mechanics*, 117(2):73–84, 2004.

[7] Gerrit WM Peters, Jeroen FM Schoonen, Frank Baaijens, and Han EH Meijer. On the performance of enhanced constitutive models for polymer melts in a cross-slot flow. *Journal of non-newtonian fluid mechanics*, 82(2):387–427, 1999.

[8] RB Bird, PJ Dotson, and NL Johnson. Polymer solution rheology based on a finitely extensible bead–spring chain model. *Journal of Non-Newtonian Fluid Mechanics*, 7(2-3): 213–235, 1980.

[9] MD Chilcott and JM Rallison. Creeping flow of dilute polymer solutions past cylinders and spheres. *Journal of Non-Newtonian Fluid Mechanics*, 29:381–432, 1988.

[10] P.J. Oliveira and A.I.P. Miranda. A numerical study of steady and unsteady viscoelastic flow past bounded cylinders. *Journal of Non-Newtonian Fluid Mechanics*, 127(1):51–66, 2005.

[11] JL Lumley. Drag reduction in turbulent flow by polymer additives. *Journal of Polymer Science: Macromolecular Reviews*, 7(1):263–290, 1973.

[12] COMSOL 3.5a Documentation. 3.5a documentation. *Multiphysics*, 2008.

[13] RJ Poole, MA Alves, and PJ Oliveira. Purely elastic flow asymmetries. *Physical review letters*, 99(16):164503, 2007.

[14] M Nyström, HR Tamaddon Jahromi, Mats Stading, and MF Webster. Numerical simulations of boger fluids through different contraction configurations for the development of a measuring system for extensional viscosity. *Rheologica acta*, 51(8):713–727, 2012.

[15] Jonathan P Rothstein and Gareth H McKinley. Extensional flow of a polystyrene boger fluid through a 4: 1: 4 axisymmetric contraction/expansion. *Journal of non-newtonian fluid mechanics*, 86(1):61–88, 1999.

[16] M.A. Hulsen, R. Fattal, and R. Kupferman. Flow of viscoelastic fluids past a cylinder at high weissenberg number: stabilized simulations using matrix logarithms. *Journal of Non-Newtonian Fluid Mechanics*, 127(1):27–39, 2005.

[17] Gerardo N Rocha, Robert J Poole, Manuel A Alves, and Paulo J Oliveira. On extensibility effects in the cross-slot flow bifurcation. *Journal of Non-Newtonian Fluid Mechanics*, 156 (1):58–69, 2009.

[18] A. Fortin, R. Guenétte, and R. Pierre. On the discrete evss method. *Computer Methods in Applied Mechanics and Engineering*, 189(1):121–139, 2000.

[19] A. Kane, R. Guénette, and A. Fortin. A comparison of four implementations of the log-conformation formulation for viscoelastic fluid flows. *Journal of Non-Newtonian Fluid Mechanics*, 164(1-3):45–50, 2009. ISSN 0377-0257.

[20] K. Ejlebjerg Jensen, P. Szabo, and F. Okkels. Topology optimization of viscoelastic rectifiers. *Applied Physics Letters*, 100(23):234102–234102, 2012.

[21] COMSOL Multiphysics. 4.3a users guide, 2013.

[22] R. Guénette, A. Fortin, A. Kane, and J.F. Hétu. An adaptive remeshing strategy for viscoelastic fluid flow simulations. *Journal of Non-Newtonian Fluid Mechanics*, 153(1): 34–45, 2008.

[23] G.H. McKinley, R.C. Armstrong, and R.A. Brown. The wake instability in viscoelastic flow past confined circular cylinders. *Philosophical Transactions: Physical Sciences and Engineering*, 344(1671):265–304, 1993.

[24] M. Sahin. Parallel large-scale simulation of viscoelastic fluid flow instabilities. In *17th International Workshop on Numerical Methods for Non-Newtonian Flows*, 2012.

[25] P.E. Arratia, CC Thomas, J. Diorio, and JP Gollub. Elastic instabilities of polymer solutions in cross-channel flow. *Physical review letters*, 96(14):144502, 2006.

[26] T. Borrvall and J. Petersson. Topology optimization of fluids in Stokes flow. *International Journal for Numerical Methods in Fluids*, 41(1):77–107, 2003.

[27] A Kawamoto, T Matsumori, T Nomura, T Kondoh, S Yamasaki, and S Nishiwaki. Topology optimization by a time-dependent diffusion equation. *International Journal for Numerical Methods in Engineering*, 2012.

[28] K. Svanberg. The method of moving asymptotes-a new method for structural optimization. *International journal for numerical methods in engineering*, 24(2):359–373, 1987.

[29] Philip E Gill, Walter Murray, and Michael A Saunders. Snopt: An sqp algorithm for large-scale constrained optimization. *SIAM journal on optimization*, 12(4):979–1006, 2002.

[30] LT Biegler and VM Zavala. Large-scale nonlinear programming using ipopt: An integrating framework for enterprise-wide dynamic optimization. *Computers & Chemical Engineering*, 33(3):575–582, 2009.

[31] Jasbir S Arora and Qian Wang. Review of formulations for structural and mechanical system optimization. *Structural and Multidisciplinary Optimization*, 30(4):251–272, 2005.

[32] L.H. Olesen, F. Okkels, and H. Bruus. A high-level programming-language implementation of topology optimization applied to steady-state Navier-Stokes flow. *International Journal for Numerical Methods in Engineering*, 65(7):975–1001, 2006. ISSN 1097-0207.

[33] BS Lazarov and O. Sigmund. Filters in topology optimization based on helmholtz-type differential equations. *International Journal for Numerical Methods in Engineering*, 86(6): 765–781, 2011.

[34] B.D. Iverson and S.V. Garimella. Recent advances in microscale pumping technologies: a review and evaluation. *Microfluidics and Nanofluidics*, 5(2):145–174, 2008.

[35] E. Stemme and G. Stemme. A valveless diffuser/nozzle-based fluid pump. *Sensors and Actuators A*, 39(2):159–167, 1993.

[36] G. Pingen and K. Maute. Optimal design for non-newtonian flows using a topology optimization approach. *Computers & Mathematics with Applications*, 59(7):2340–2350, 2010.

[37] A. Groisman and S.R. Quake. A microfluidic rectifier: Anisotropic flow resistance at low Reynolds numbers. *Physical review letters*, 92(9):94501, 2004.

[38] PC Sousa, FT Pinho, MSN Oliveira, and MA Alves. Efficient microfluidic rectifiers for viscoelastic fluid flow. *Journal of Non-Newtonian Fluid Mechanics*, page 652671, 2010.

[39] G. Pingen, A. Evgrafov, and K. Maute. A parallel schur complement solver for the solution of the adjoint steady-state lattice boltzmann equations: application to design optimisation. *International Journal of Computational Fluid Dynamics*, 22(7):457–464, 2008.

[40] DV Boger. A highly elastic constant-viscosity fluid. *Journal of Non-Newtonian Fluid Mechanics*, 3(1):87–91, 1977.

[41] L. Carracciuolo, D. Casaburi, L. D'Amore, G. D'Avino, PL Maffettone, and A. Murli. Computational simulations of 3d large-scale time-dependent viscoelastic flows in high performance computing environment. *Journal of Non-Newtonian Fluid Mechanics*, 166:1382–1395, 2011.

[42] F. Wang, B.S. Lazarov, and O. Sigmund. On projection methods, convergence and robust formulations in topology optimization. *Structural and Multidisciplinary Optimization*, 43 (1):767–784, 2011.

[43] R.J. Yang, H.H. Hou, Y.N. Wang, C.H. Lin, and L.M. Fu. A hydrodynamic focusing microchannel based on micro-weir shear lift force. *Biomicrofluidics*, 6(3):034110–034110, 2012.

[44] H.W. Hou, H.Y. Gan, A.A.S. Bhagat, L.D. Li, C.T. Lim, and J. Han. A microfluidics approach towards high-throughput pathogen removal from blood using margination. *Biomicrofluidics*, 6(2):024115, 2012.

[45] G.M. Whitesides. The origins and the future of microfluidics. *Nature*, 442(7101):368–373, 2006.

[46] P.C. Sousa, F.T. Pinho, M.S.N. Oliveira, and M.A. Alves. High performance microfluidic rectifiers for viscoelastic fluid flow. *RSC Adv.*, 2(3):920–929, 2012.

[47] C.H. Tsai, C.H. Lin, L.M. Fu, and H.C. Chen. High-performance microfluidic rectifier based on sudden expansion channel with embedded block structure. *Biomicrofluidics*, 6(2): 024108, 2012.

[48] YC Lam, HY Gan, NT Nguyen, and H. Lie. Micromixer based on viscoelastic flow instability at low reynolds number. *Biomicrofluidics*, 3(1):014106, 2009.

[49] N.T. Nguyen, Y.C. Lam, S.S. Ho, and C.L.N. Low. Improvement of rectification effects in diffuser/nozzle structures with viscoelastic fluids. *Biomicrofluidics*, 2(3):034101, 2008.

[50] P. Cheung, K. Toda-Peters, and A.Q. Shen. In situ pressure measurement within deformable rectangular polydimethylsiloxane microfluidic devices. *Biomicrofluidics*, 6(2):026501, 2012.

[51] Y. Xia and G.M. Whitesides. Soft lithography. *Annual Review of Materials Science*, 28(1): 153–184, 1998.

[52] L. Campo-Deaño, F.J. Galindo-Rosales, F.T. Pinho, M.A. Alves, and M.S.N. Oliveira. Flow of low viscosity boger fluids through a microfluidic hyperbolic contraction. *Journal of Non-Newtonian Fluid Mechanics*, 166(21):1286–1296, 2011.

[53] PC Sousa, FT Pinho, MSN Oliveira, and MA Alves. Extensional flow of blood analog solutions in microfluidic devices. *Biomicrofluidics*, 5(1):014108, 2011.

[54] R. Fattal and R. Kupferman. Time-dependent simulation of viscoelastic flows at high weissenberg number using the log-conformation representation. *Journal of Non-Newtonian Fluid Mechanics*, 126(1):23–37, 2005.

[55] K. Ejlebjerg Jensen, P. Szabo, F. Okkels, and MA Alves. Experimental characterisation of a novel viscoelastic rectifier design. *Biomicrofluidics*, 6:044112, 2012.

[56] A. Groisman, M. Enzelberger, and S.R. Quake. Microfluidic memory and control devices. *Science*, 300(5621):955, 2003.

[57] Peter Szabo, Gareth H McKinley, and Christian Clasen. Constant force extensional rheometry of polymer solutions. *Journal of Non-Newtonian Fluid Mechanics*, 169:26–41, 2012.

[58] Krister Svanberg. A class of globally convergent optimization methods based on conservative convex separable approximations. *SIAM Journal on Optimization*, 12(2):555–573, 2002.